



저작자표시-비영리-변경금지 2.0 대한민국

이용자는 아래의 조건을 따르는 경우에 한하여 자유롭게

- 이 저작물을 복제, 배포, 전송, 전시, 공연 및 방송할 수 있습니다.

다음과 같은 조건을 따라야 합니다:



저작자표시. 귀하는 원저작자를 표시하여야 합니다.



비영리. 귀하는 이 저작물을 영리 목적으로 이용할 수 없습니다.



변경금지. 귀하는 이 저작물을 개작, 변형 또는 가공할 수 없습니다.

- 귀하는, 이 저작물의 재이용이나 배포의 경우, 이 저작물에 적용된 이용허락조건을 명확하게 나타내어야 합니다.
- 저작권자로부터 별도의 허가를 받으면 이러한 조건들은 적용되지 않습니다.

저작권법에 따른 이용자의 권리는 위의 내용에 의하여 영향을 받지 않습니다.

이것은 [이용허락규약\(Legal Code\)](#)을 이해하기 쉽게 요약한 것입니다.

[Disclaimer](#)

공학박사학위논문

**Instability of Cryogenic Swirl Flows  
under Subcritical to Supercritical Conditions**

아임계 및 초임계 조건에서  
극저온 스월 유동의 불안정성

2015년 2월

서울대학교 대학원

기계항공공학부

조성호

## ABSTRACT

Instability characteristics of cryogenic swirl flows were experimentally investigated. The cryogenic liquid nitrogen was injected into a high-pressure chamber through a simplex swirl injector under subcritical to supercritical conditions of nitrogen. High-speed photography with backlight imaging was used to obtain images of the temporally changing flow. The set of images was analyzed by the image processing method. The instability frequency was measured by flow image processing and the laser beam diagnostics.

Surface instability of the flow under subcritical to supercritical condition was investigated. Comparing the flow images of the cryogenic and conventional swirl flows, different behaviors were noted, and it was hypothesized that the instability of the cryogenic swirl flow was dominated by the precessing vortex core in the central toroidal recirculation zone. When the ambient condition of the flow was changed from subcritical to supercritical, the phase change and subsequent density change of the injectant differed and flow actions, such as the behavior of the downstream flow, the spray angle, the wavelength, and the propagation velocity, changed drastically. When measuring the frequency of the flow instability, it was found to correspond to that of the precessing vortex core instability. The frequency decreased with the ambient pressure due to the decreasing flow velocity, but it did not change drastically when the surrounding conditions changed from subcritical to supercritical. This implies that the interface of the flow is highly affected by the density of the phase-changed injectant, but that the instability of the flow is determined by the flow in a liquid state.

The dynamic characteristics of a cryogenic swirl flow under supercritical conditions were experimentally investigated using a mode decomposition method. Superposed instability structures and vortex ring structures were found in the instantaneous flow image. The spray angle was decreased under supercritical conditions because of the unusual phase change of the injectant inside the injector. Two kinds of modes were deduced by POD analysis of the flow images. The analysis showed that two types of modes exist: a symmetric/tilted-ring shaped mode and an anti-symmetric shaped mode.

The Kelvin-Helmholtz instability mechanism generated the symmetric mode. The anti-symmetric structure was created by helical instability, which was generated by the instability of the liquid film inside the injector under subcritical conditions. However, under supercritical conditions, the precessing vortex core in the central toroidal recirculation zone determined the unstable behavior of the flow. A spatial and temporal analysis of the POD modes supported this explanation for the instability. Meanwhile, the spatial characteristics of the coherent structures became similar in the downstream region or under supercritical conditions, which implicates the strong influence of the state of the injectant in flow behavior.

**Keywords:** Liquid Propellant Rocket Engine, Simplex Swirl Injector, Cryogenic Flow, Supercritical Condition, Flow Instability, Proper Orthogonal Decomposition

**Student Number:** 2009-30169

# LIST

ABSTRACT .....	i
LIST.....	iii
LIST OF FIGURES.....	vi
LIST OF TABLES.....	ix
NOMENCLATURE.....	x

## CHAPTER 1

INTRODUCTION.....	1
1.1 Background and Motivation.....	1
1.2 Survey of Relevant Literature .....	5
1.2.1 Characteristics of fluid under supercritical condition .....	5
1.2.2 Single and coaxial jet flow .....	6
1.2.3 Jet flow with external excitation .....	8
1.2.4 Simplex swirl flow .....	9
1.3 Scope of Study.....	10

## CHAPTER 2

EXPERIMENTAL METHOD .....	11
2.1 Experimental Apparatus .....	11
2.1.1 Design procedure of swirl injector .....	11
2.1.2 High-pressure chamber .....	17
2.1.3 Cryogenic fluid feeding system .....	19
2.2 Flow Measurement .....	20
2.2.1 High-speed photography .....	21
2.2.2 Flow instability frequency measurement .....	23

CHAPTER 3	
SURFACE INSTABILITY ON CRYOGENIC SWIRL FLOW	
UNDER SUB- TO SUPERCRITICAL CONDITIONS.....	24
3.1 Background and Objectives .....	24
3.2 Experimental Methods .....	27
3.2.1 Injector design.....	27
3.2.2 Experimental conditions.....	28
3.2.3 Experimental techniques .....	30
3.3 Results and Discussion .....	31
3.3.1 Characteristics of the cryogenic swirl flow .....	31
3.3.2 Effect of the ambient pressure on a cryogenic swirl flow surface.....	34
3.3.3 Instability analysis of a cryogenic swirl flow surface.....	43
CHAPTER 4	
DYNAMIC CHARACTERISTICS OF A CRYOGENIC SWIRL FLOW	
UNDER SUPERCRITICAL CONDITIONS.....	46
4.1 Background and Objectives .....	46
4.2 Experimental Methods .....	48
4.2.1 Injector design.....	48
4.2.2 Experimental conditions.....	50
4.2.3 Experimental techniques .....	51
4.2.4 Proper Orthogonal Decomposition.....	51
4.3 Results and Discussion .....	54
4.3.1 Static characteristics of a cryogenic flow .....	54
4.3.2 POD analysis of flow image .....	57
4.3.3 Analysis of POD mode.....	69
CHAPTER 5	
CONCLUSION AND FUTURE WORK.....	74
5.1 Conclusion .....	74

5.2 Recommendations for Future Work.....	76
APPENDIX	
PROPER ORTHOGONAL DECOMPOSITION.....	77
A.1 Background .....	77
A.2 POD Analysis Procedure .....	77
BIBLIOGRAPHY .....	81
ABSTRACT IN KOREAN.....	87

## LIST OF FIGURES

Fig. 1.1	Combustion process in liquid propellant rocket engine	2
Fig. 1.2	Hierarchy of injector experiments [Talley, 2002]	2
Fig. 1.3	Transcritical process of liquid propellant in combustion chamber of liquid propellant rocket engine	4
Fig. 2.1	Schematic of liquid swirl injector [Kim, 2013]	12
Fig. 2.2	High-pressure chamber	18
Fig. 2.3	Air curtain system	18
Fig. 2.4	Cryogenic fluid feeding system	19
Fig. 2.5	Flow condition measurement inside swirl injector	21
Fig. 2.6	High-speed photography	22
Fig. 2.7	Flow instability frequency measurement using Ar-Ion laser	23
Fig. 3.1	Open-type simplex swirl injector (unit: mm)	27
Fig. 3.2	Experimental conditions in Pressure-Temperature diagram of nitrogen	29
Fig. 3.3	Instantaneous swirl flow image at $\Delta P = 1$ MPa, $P_c = 1$ MPa for (a) cryogenic swirl flow and (b) water swirl flow; (left) original image and (right) flow boundary	32
Fig. 3.4	Representative swirl flow images under various ambient pressure conditions for instantaneous image (top row) and averaged image (bottom row) at $\Delta P = 0.5$ MPa	35
Fig. 3.5	Instantaneous swirl flow image at $\Delta P = 0.5$ MPa for (a) $P_c = 2$ MPa (subcritical conditions) and (b) $P_c = 4$ MPa (supercritical conditions); (left) original image and (right) flow boundary	36
Fig. 3.6	Spray angle of cryogenic swirl flow	38
Fig. 3.7	Image analysis of cryogenic swirl flow for (a) sinusoidal wave imposed on plane liquid sheet, (b) flow boundary detection and (c) sine curve fitting of flow surface	40

Fig. 3.8	Wave amplitude on surface of cryogenic swirl flow	41
Fig. 3.9	Wavelength on surface of cryogenic swirl flow	42
Fig. 3.10	Propagation velocity of surface wave in axial direction	42
Fig. 3.11	Results from spectral analysis of transmission rate at $\Delta P = 0.5$ MPa under various ambient pressure conditions: (a) $P_c = 2$ MPa, (b) $P_c = 4$ MPa	45
Fig. 3.12	Instability frequency of cryogenic swirl flow	45
Fig. 4.1	Schematic of the simplex swirl injector (unit: mm)	49
Fig. 4.2	Experimental conditions in Pressure-Temperature diagram of nitrogen	50
Fig. 4.3	Analysis area of the flow image for the upstream (yellow line) and downstream (red line) regions	53
Fig. 4.4	Representative images of the cryogenic swirl flow; instantaneous (left column) and averaged (right column) images for (a) subcritical, (b) critical, (c) supercritical ambient conditions, and (d) structures on the flow surface	55
Fig. 4.5	Spray angle of the cryogenic swirl flow	56
Fig. 4.6	POD mode eigenvalue distribution for the experimental conditions; (a) upstream modes, and (b) downstream modes	58
Fig. 4.7	Initial 10 POD modes for subcritical condition ( $P_c = 2.0$ MPa); upstream region	59
Fig. 4.8	Initial 10 POD modes for subcritical condition ( $P_c = 2.0$ MPa); downstream region	60
Fig. 4.9	Initial 10 POD modes for critical condition ( $P_c = 3.4$ MPa); upstream region	61
Fig. 4.10	Initial 10 POD modes for critical condition ( $P_c = 3.4$ MPa); downstream region	62
Fig. 4.11	Initial 10 POD modes for supercritical condition ( $P_c = 5.0$ MPa); upstream region	63

Fig. 4.12	Initial 10 POD modes for supercritical condition ( $P_c = 5.0$ MPa); downstream region	64
Fig. 4.13	Representative POD modes of the upstream cryogenic swirl flow; symmetric/tilted-ring structure (left column) and anti-symmetric structure (right column) modes for (a) subcritical, (b) critical, and (c) supercritical ambient conditions	67
Fig. 4.14	Representative POD modes of the downstream cryogenic swirl flow; symmetric/tilted-ring structure (left column) and anti-symmetric structure (right column) modes for (a) subcritical, (b) critical, and (c) supercritical ambient conditions	68
Fig. 4.15	Conjugate pair analysis of POD modes at $P_c = 2.0$ MPa (upstream region): (a) conjugate mode images, and (b) cross-power spectral density for conjugate modes	70
Fig. 4.16	Instability frequency of POD modes in the cryogenic swirl flow	71
Fig. 4.17	Wavelength of POD modes in the cryogenic swirl flow	73

## LIST OF TABLES

Table 1.1	Recently developed liquid propellant rocket engines [Talley, 2002]	3
Table 1.2	Table 1.2 Critical properties of fluids	4
Table 3.1	Injector geometry	28
Table 3.2	Experimental conditions	30
Table 4.1	Injector geometry	49
Table 4.2	Experimental conditions	51

## NOMENCLATURE

### *Alphabet*

$A_0$	cross-section area of discharge orifice
$a_{i,n}$	time coefficient of POD mode
$C$	open coefficient
$C_d$	discharge coefficient
$C_{d,eq}$	equivalent discharge coefficient
$D_s$	swirl chamber diameter
$d_L$	manufacture diameter
$d_{o,i}$	inner diameter of orifice exit
$d_{o,o}$	outer diameter of orifice exit
$d_p$	diameter of tangential inlet
$f$	frequency
$I$	laser beam intensity
$I_0$	Initial laser beam intensity
$K$	injector geometric constant, $Rr_o/ir_p^2$
$K_D$	injector geometric constant concerning deformation effect
$K_{eq}$	equivalent injector geometric constant
$k$	wave number
$L$	length of the injector
$M$	number of data points in flow field
$\dot{m}_l$	spray mass flow rate
$N$	number of snapshots/images used in POD analysis
$n$	number of tangential inlet
$P_c$	chamber pressure
$R$	swirl arm from axis of injector to center of tangential inlet
$Re_p$	Reynolds number of tangential entry
$r_o$	radius of orifice exit

$r_p$	radius of tangential inlet
$r_{p,eq}$	equivalent radius of tangential inlet
$r_r'$	radius of gas core at orifice exit
$S$	dimensionless radius of gas core in discharge orifice, $r_r'/r_0$
$T_c$	ambient chamber temperature
$t$	time
$u$	axial velocity
$V$	set of flow field snapshots
$v$	flow field snapshot
$w$	tangential velocity
$x$	distance from injector post along liquid sheet
$Z$	companion matrix of POD

### ***Greek***

$\alpha$	Spray angle
$\alpha_{ideal}$	Ideal spray angle
$\alpha_{eq}$	Equivalent spray angle
$\Delta_{in}$	Energy loss at tangential entry
$\Delta_k$	Energy loss at wall of vortex chamber
$\Delta_L$	Energy loss due to swirl chamber wall length
$\Delta_{noz}$	Energy loss at converging part
$\Delta P_{ideal}$	ideal injection differential pressure
$\Delta P_{eq}$	equivalent injection differential pressure
$\varepsilon$	Jet deformation rate
$\eta_0$	wave amplitude
$\lambda_i$	eigenvalue of POD mode
$\lambda_k$	friction coefficient
$\lambda_{laser}$	Laser wavelength

$\Phi$	set of POD modes
$\varphi$	filling efficiency
$\varphi_c$	corrected filling efficiency
$\phi_i$	$i$ th POD mode
$\Psi$	injector contraction angle
$\omega$	wave growth rate

### ***Subscripts***

$c$	chamber
$eq$	equivalent value
$l$	liquid
$o$	discharge orifice

# CHAPTER 1

## INTRODUCTION

### 1.1 Background and Motivation

A combustion occurred in a liquid propellant rocket engine is an important process which determines performance of the engine. Comprehensive study of the combustion process in the rocket engine is required to improve the understanding and acquire crucial information of combustion phenomena which can be used in the engine development.

The detailed combustion process is shown in Fig. 1.1. In the liquid propellant rocket engine, fuel and oxidizer are injected into the chamber through the injector. Propellants in liquid state are then atomized, vaporized and mixed inside the chamber. The combustion process of the propellants starts and the combusted gas is created. These products of combustion expands through the nozzle of the engine and finally generates the thrust. In this process, injector dominates the atomization process and affects the combustion of the propellants.

Because the injector has a huge influence on the performance of the liquid propellant rocket engine, the development of liquid propellant rocket engine starts from the design of the injector in consideration of engine performance requirement [Talley, 2002]. After injector design, cold flow test under atmospheric pressure is usually conducted using single injector element. Then the experiment under high pressure or supercritical condition is carried out. Hot fire test is followed after cold flow test; single element test and subscale multi-element test are conducted. Finally, full scale testing is carried out and the engine development is finished. This process is shown in Fig. 2.2.

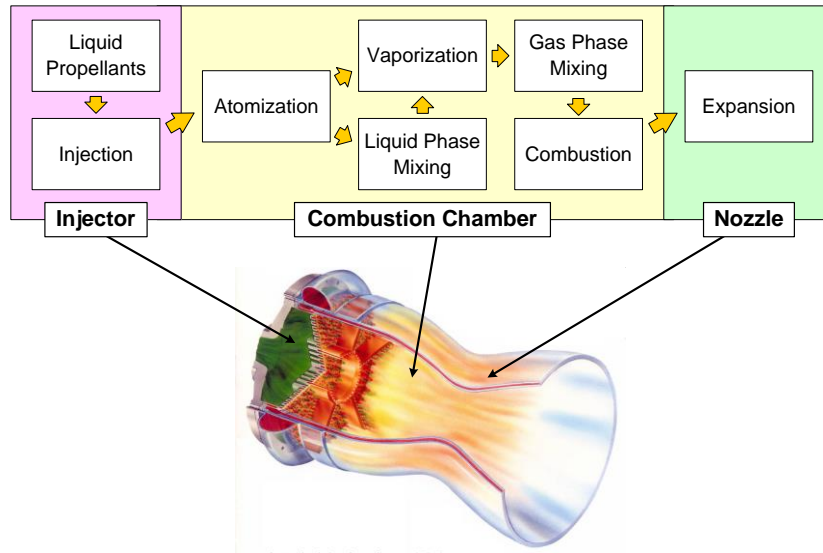


Fig. 1.1 Combustion process in liquid propellant rocket engine

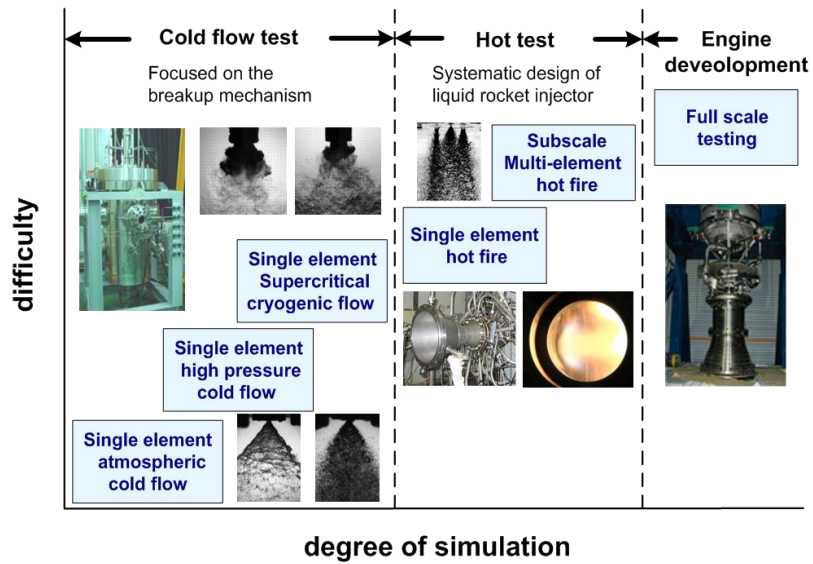


Fig. 1.2 Hierarchy of injector experiments [Talley, 2002]

It is well known that the higher chamber pressure allows the higher specific impulse for the engine [Oschwald et al., 2006]. Thus, as shown in Table 1.1, recently developed liquid propellant rocket engines operates under high pressure and temperature conditions to acquire the high performance. In this situation, the pressure and temperature inside the combustion chamber exceeds the critical conditions of the injected propellants. As a result, the state of the propellants injected into the chamber is changed from liquid to supercritical fluid. This phase change process is called “transcritical process” [Chehroudi et al., 2003; Mayer et al., 1998; Yang, 2000]. In this process, propellants are injected first. The pressure is decreased and temperature is increased, and the propellants are remained in liquid state. Because of the high temperature of the combustion chamber (~ 3000 K), propellants are then heated. The propellants are then changed from liquid to supercritical fluid, and the thermophysical properties are changed drastically.

Table 1.1 Recently developed liquid propellant rocket engines [Talley, 2002]

Vehicle	Year	Engine	Injector type	Propellants	Combustion pressure (MPa)
Ariane 5	1996	Vulcain	Shear coaxial	LOx / H <sub>2</sub>	10
Ariane 5E	Dev.	VINCI	Shear coaxial	LOx / H <sub>2</sub>	6
Atlas V	2002	RD-180	Swirl coaxial	LOx / RP-1	26.7
Delta IV	2002	RS-68	Shear coaxial	LOx / H <sub>2</sub>	10.2
H-II	1994	LE-7	Shear coaxial	LOx / H <sub>2</sub>	12.7
Space Shuttle	1981	RS-25	Shear coaxial	LOx / H <sub>2</sub>	20.6
Titan IV	1997	LR-87	Shear coaxial	N <sub>2</sub> O <sub>4</sub> / Aerozine-50	6
Falcon-9	2010	Merlin	Pintle	LOx / RP-1	9.7
Antares	2013	NK-33	Swirl coaxial	LOx / RP-1	14.5

Table 1.2 Critical properties of fluids

Fluid	Critical pressure (MPa)	Critical Temperature (K)
N <sub>2</sub>	3.39	126.2
O <sub>2</sub>	5.04	154.6
H <sub>2</sub>	1.31	33.2
He	0.23	5.2
CH <sub>4</sub>	4.59	190
RP-1	2.17	662

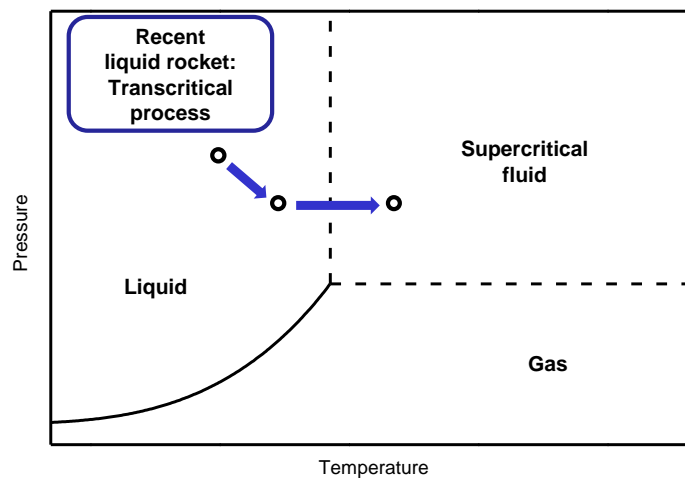


Fig. 1.3 Transcritical process of liquid propellant in combustion chamber of liquid propellant rocket engine

In case of the propellant injection under supercritical condition, conventional liquid atomization model cannot be used to explain the breakup process inside the combustion chamber. Therefore, the combustion characteristics to the new model should be suggested which can explain the behavior of the liquid propellant in transcritical process. Various studies of the fluid injection under supercritical condition have been conducted for this purpose with experimental and numerical approach.

## **1.2 Survey of Relevant Literature**

The first study about liquid atomization in near-critical region was conducted in 1970's [Newman and Brzustowski, 1971]. However, because of the difficulty of experiment and lack of interest, systematic investigations about this topic was started after 1990's. Most of the related studies were conducted by the German Aerospace Center (DLR) and the Air Force Research Laboratory in USA (AFRL).

The studies conducted using experimental approach mainly used liquid nitrogen as a simulant of LOx; the critical properties of the nitrogen and oxygen are similar, and the handling of liquid nitrogen was easier than LOx. The LOx flow was investigated by numerical analysis. Because the study of transcritical injection process was conducted to reveal the breakup mechanism and characteristics of non-reacting flow, single/coaxial jet with/without external excitation was considered and the reacting flow is not included in this section.

### **1.2.1 Characteristics of fluid under supercritical condition**

Among the various properties of the fluid, surface tension is the most important property in breakup process. With this property, liquid resists expansion of its surface area [Lefebvre, 1989]. The external force must exceed the surface tension force to achieve atomization. In supercritical fluid, however, surface tension is diminished [Mayer et al., 2001; Oswald et al., 2006]. As a result, the liquid-gas like breakup process and gas-gas

like mixing behavior can be observed in transcritical process [Chehroudi et al., 2003].

For coaxial injection of  $O_2$  and  $H_2$  in the liquid propellant rocket engine, mixing and burning phenomena of oxidizer and fuel occurs at the shear layer between two fluids. The critical properties of a mixture should be considered. Single critical point cannot be defined, but critical mixing lines define the state of the mixture. The solubility and the surface tension is determined by the pressure, temperature and mole fraction of the mixture. Previous study [Mayer et al., 2001] found that the critical temperature decreases with increasing pressure. Surface tension would exist in the mixture while the pressure is above the critical pressure of pure  $O_2$ . It implies that the solubility of liquid droplet would be decreased when the surrounding gas is the mixture [Mayer et al., 1998]. Surface tension decreased with the increase of pressure and temperature.

The properties of the fluid become very sensitive at the near-critical pressure condition. The specific heat would reach maximum peak value at certain temperature. At this temperature, the fluid would behave like a liquid at boiling point. This point is called pseudo-boiling point, and the thermal diffusivity reaches a distinct minimum. Because of the unusual characteristics of this point, further study of flow behavior should be conducted in consideration of pseudo-boiling [Banuti and Hannemann, 2014].

### **1.2.2 Single and coaxial jet flow**

Jet flow can be observed in the liquid propellant rocket engines developed in USA and Europe, which uses impinging type injector and shear coaxial type injector. To understand the mechanism of liquid breakup under supercritical conditions, the simplest and most fundamental case of the flow was investigated first. Various experimental methods have been adopted for the research of the jet flow in qualitative and quantitative manner. The investigation of coaxial jet was followed.

The qualitative analysis of jet surface was conducted first [Chehroudi et al., 2002b; Mayer and Tamura, 1996; Mayer et al., 1998]. In these studies, the different breakup mechanism of single jet was observed. Under subcritical condition, annular liquid jet was

atomized and droplet was found on the flow surface. However, the comb-like structure caused by transcritical process existed on the surface under supercritical conditions. This phenomena was caused by the existance of mixing layer around the jet surface. The injectant behaved like a dense gas in this condition. Although the density variation was very large, the buoyancy effect could be ignored [Chehroudi et al., 2002b].

The length of the single jet was measured by flow imaging [Chehroudi et al., 2003]. The measured dark core region of the jet was thought as potential core. However, the results obtained from the flow imaging was slightly differnet to the result obtained from Raman scattering method [Mayer et al., 2003].

Research of the growth rate of the single jet has been conducted intensively because it provides a mixing characteristics of the jet. In AFRL, the first quantitative analysis of the growth rate of single jet was conducted [Chehroudi et al., 2002b]. They plotted the growth rate along the density ratio of injectant and ambient gas, and compared the result to the previous works about gas jet. The obtained results showed that the co-existence of liquid-like and gas-like behavior of the jet. By adopting the concept of appropriate characteristic time such as bulge formation time and the gasification time, phenomenologiral model of the jet growth rate was developed. The results showed good agreement with the results obtained from Raman scattering method [Chehroudi et al., 2002a].

For the quantitative measurement of the flow, Raman scattering measurement method was adopted [Chehroudi et al., 2002a; Oswald and Schik, 1999]. The density and temperature distribution of the flow field were then measured by this method. As the initial injection temperature decreaased, the density decay was slower. Because of pseudo-boiling effect, the temperature of jet was maintained while the specific volume was increased with the heat transfer to the jet [Oswald and Schik, 1999]. The self-similarity of the density field was observed in jet flow [Chehroudi et al., 2002a].

The investigation of coaxial jet used measurement methods similar to the single jet. One more parameter, the velocity ratio between inner liquid jet and outer gas jet, was considered in this subject. In LN<sub>2</sub>/GN<sub>2</sub> coaxial jet, the outer coaxial gas jet played two

roles; the assistance of inner jet breakup and the heat transfer behavior [Davis and Chehroudi, 2007]. The dark core length decreased along the increase of velocity ratio, and the length was drastically decreased under supercritical conditions.

### **1.2.3 Jet flow with external excitation**

The study of jet with external excitation is required to reveal the effect of combustion instability to the behavior of the injected propellant. For example, the fluctuation of the flow can interact with the velocity fluctuation parallel to the injector face [Oefelein and Yang, 1993].

In both single and coaxial jets, the impact of the external forcing to the jet was significant under subcritical conditions [Davis and Chehroudi, 2007]; the fluctuation of dark core length was larger than that under supercritical conditions. In coaxial jet flow, higher outer jet velocity would decrease the fluctuation of jet length. From these results, it can be deduced that flow under supercritical condition with high velocity of coaxial flow is less sensitive to the external excitation. Therefore it would be announced that the probability of combustion instability can be reduced under this flow condition.

A numerical analysis about the coaxial jet with external excitation was conducted [Schmitt et al., 2012]. The results obtained from this study was similar to that from experimenatal studies. However, the analysis of dynamic characteristics of the flow showed interesting results. When the flow has natural frequency, then the response of the flow to the excitation followed its natural frequency; the flow oscillated with the sub-harmonic of excitation frequency, which is similar to the natural frequency of the flow.

#### 1.2.4 Simplex swirl flow

Although lots of research about jet flow have been conducted, the swirl flow under supercritical flow was rarely studied. In contrast with shear-coaxial injector which generates jet flow, swirl injector enhances mixing because of the impartment of radial momentum to the injectant. Therefore, his type of injector have been used in many liquid propellant rocket engines developed in Russia [Bazarov and Yang, 1998; Borodin et al., 1968; Khavkin, 2004]. However, many research about the swirl injector was not introduced to USA or Europe which mainly concerned about single and coaxial jet flow found in the rocket engines using shear-coaxial injector. Moreover, the swirl flow is more complicated than the jet flow and difficult to examine. Therefore, the swirl flow under supercritical condition was less favored from DLR and AFRL.

It is difficult to find the experimental study of swirl flow under supercritical condition. In Marshall Space Flight Center, characteristics of the swirling LO<sub>x</sub>/GH<sub>2</sub> jet coaxial flow were investigated experimentally [Hutt and Cramer, 1996]. They found the periodic occurrence of globules in LO<sub>x</sub> spray breakup process, and the vanishment of the surface tension near the critical pressure. However, this study conducted qualitative investigation only, and additory research was not carried out.

The numerical analysis of swirl flow under supercritical condition have been attempted more frequently than experimental approach. Dynamic characteristics of LO<sub>x</sub> flow under supercritical condition was investigated first [Zong and Yang, 2008]. The flow was injected from open-type swirl injector, and the instability mechanism inside and outside of the injector was revealed. While the hydrodynamic instability and the acoustic oscillation generated instability of the flow inside the injector element, Kelvin-Helmholtz instability and Precessing Vortex Core instability dominated the external flow instability. The effect of injector geometry and swirl strength also was investigated. Additional research of the injector with similar geometry was followed [Heo et al., 2012; Huo et al., 2014].

### **1.3 Scope of Study**

This study aimed to conduct experimental investigation of the characteristics of the cryogenic swirl flows under subcritical to supercritical conditions, especially LOx swirl flow. The liquid nitrogen was used as a simulant of the LOx, and the simplex swirl injector was used to create conical liquid sheet. The ambient condition of the flow was controlled by high-pressure chamber. The behavior of the flow was measured with high-speed photography and laser diagnostics method. The static and dynamic characteristics of the flow along the ambient conditions were observed.

In Chapter 2, the experimental methods used in this study was explained. The design process of the swirl injector, high-pressure chamber and cryogenic fluid feeding system were described. The high-speed photography and flow instability frequency measurement were also introduced. In Chapter 3, flow characteristics injected by open-type swirl injector were studied. Differences between cryogenic flow and conventional liquid flow were observed first, and the characteristics of flow pattern were investigated. Wavy structure on flow surface was analyzed in quantitative manner. The frequency of flow instability were measured. In Chapter 4, dynamic characteristics of flow injected by closed-type swirl injector were studied. The spatial and temporal characteristics of flow dynamics was revealed by application of mode decomposition method to the flow image set. Finally, whole results were concluded in Chapter 5.

## **CHAPTER 2**

### **EXPERIMENTAL METHOD**

#### **2.1 Experimental Apparatus**

The experiments conducted in this study aimed to simulate the liquid oxygen flow in the combustion chamber of the liquid propellant rocket engine. Therefore, liquid nitrogen was injected into a high-pressure chamber through a simplex swirl type injector. Liquid nitrogen was used as a working fluid to simulate liquid oxygen. Owing to the similar critical properties of these fluids (nitrogen: 3.39 MPa/126.2 K; oxygen: 5.04 MPa/154.6 K) as shown in Table 1.1, liquid nitrogen has been used in many studies as a simulant of liquid oxygen for safety purposes [Chehroudi et al., 2002b; Mayer and Tamura, 1996; Schmitt et al., 2012; Zong et al., 2004]. The simplex swirl type injector was mounted inside the high-pressure chamber to create the hollow-cone shape swirl flow. The cryogenic fluid feeding system was used to maintain nitrogen in liquid state and feed the fluid into the high-pressure chamber. The high-pressure chamber was used to control the ambient condition of the flow and change it from subcritical to supercritical condition of the liquid nitrogen.

##### **2.1.1 Design procedure of swirl injector**

Many type of the injectors such as jet injector, impinging injector, pintle injector and swirl injector are used in the liquid propellant rocket engines. Among these, the swirl type injector is widely used in the engine developed in Russia [Bazarov and Yang, 1998; Khavkin, 2004]. This injector type has many advantages compared to the other injectors [Bazarov and Yang, 1998; Borodin et al., 1968; Dityakin et al., 1977; Khavkin, 2004; Lefebvre, 1989]. A schematic of the liquid swirl injector is shown in Fig. 2.1.

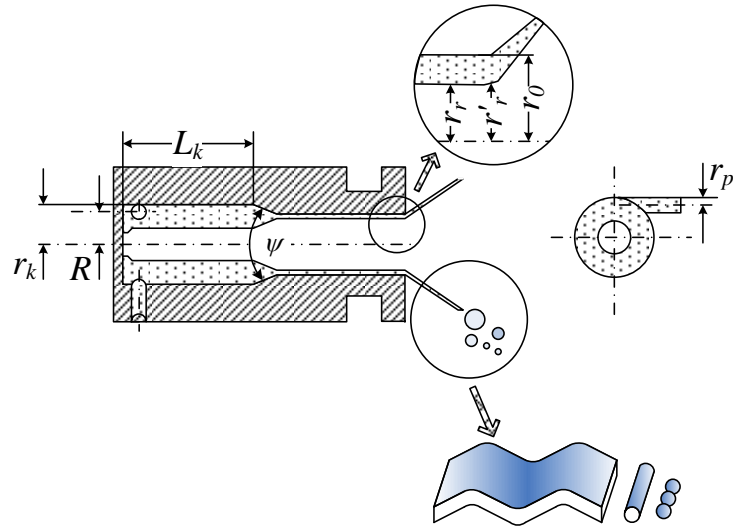


Fig. 2.1 Schematic of liquid swirl injector [Kim, 2013]

Before the design of swirl type injector, the performance and the size of the engine should be confirmed [Kim, 2013]. After this process, density of the propellant  $\rho$ , mass flow rate  $\dot{m}_l$ , injector nozzle diameter  $d_o$ , number of tangential inlet  $n$ , length of the injector  $L$  and ideal value of injection differential pressure  $\Delta P_{ideal}$  are determined. The design process of the injector starts with these variables, and the equivalent tangential inlet radius  $r_{p,eq}$  and equivalent injection differential pressure  $\Delta P_{eq}$  are finally obtained.

The design process is based on the ideal liquid theory and viscous liquid theory (reference). Approximated injector design is deduced from the ideal liquid theory, and the deformation and viscous effect on the flow is concerned in viscous liquid theory for correction of the design.

### 1. Ideal liquid theory

From the ideal liquid theory, discharge orifice area  $A_o$ , discharge coefficient  $C_d$ , and the filling efficiency  $\varphi$  should be calculated first.

$$A_o = \frac{\pi}{4} d_{o,i}^2 \quad (2.1)$$

$$C_d = \frac{\dot{m}_l}{A_o \sqrt{2\rho\Delta p_{ideal}}} \quad (2.2)$$

$$C_d = \sqrt{\frac{\varphi^3}{2-\varphi}} \rightarrow \varphi \quad (2.3)$$

$$K = \frac{(1-\varphi)\sqrt{2}}{\varphi\sqrt{\varphi}} \quad (2.4)$$

$K$  is the geometric constant. It determines the swirling strength of the injected fluid.

$$C = \frac{R}{r_o} \rightarrow R = Cr_o \quad (2.5)$$

$C$  is the open coefficient. The value of  $C$  is 0.915 for open type injector and 1.25 ~ 5.0 for closed type injector [Bayvel, 1993; Khavkin, 2004]. The swirl arm  $R$  can be determined with Eq. 2.5.

The tangential inlet radius  $r_p$  and the spray angle  $\alpha_2$  is finally deduced by Eq. 2.6 ~ 2.9.

$$K = \frac{Rr_o}{nr_p^2} \rightarrow r_p = \sqrt{\frac{Rr_o}{nK}} \quad (2.6)$$

$$C_d = \sqrt{1 - C_d^2 K^2} - S \sqrt{S^2 - C_d^2 K^2} - C_d^2 K^2 \ln \frac{1 + \sqrt{1 - C_d^2 K^2}}{S + \sqrt{S^2 - C_d^2 K^2}} \quad (2.7)$$

$$S = \frac{r_r}{r_o} \quad (2.8)$$

$$\tan \frac{\alpha_2}{2} = \frac{2C_d K}{\sqrt{(1+S)^2 - 4C_d^2 K^2}} \quad (2.9)$$

## 2. Viscous liquid theory

In the real flow inside the swirl injector, non-negligible deformation of the jet can be occurred at the tangential entries inside the vortex chamber.  $K_D$ , geometric constant concerning deformation effect, and the corrected filling efficiency  $\varphi_c$  are calculated via Eq. 2.10 using jet deformation factor  $\varepsilon$  [Borodin et al., 1968].

$$K_D = \frac{K}{\varepsilon} = \frac{(1 - \varphi_c) \sqrt{2}}{\varphi_c \sqrt{\varphi_c}} \rightarrow \varphi_c \quad (2.10)$$

From  $K_D$ , the tangential inlet radius  $r_{p,eq}$  can be deduced.

$$K_D = \frac{Rr_o}{ir_{p,eq}^2} \rightarrow r_{p,eq} = \sqrt{\frac{Rr_o}{nK_D}} \quad (2.11)$$

The swirl chamber diameter  $D_s$  can be calculated by Eq. 2.12.

$$D_s = 2R + 2r_p + 2d_L, \quad (2.12)$$

$d_L$  is manufacture diameter.

In the viscous flow, friction effect should be considered to explain the flow motion. Friction due to the rotating flow in vortex chamber can cause the decrease in the spray angle. Therefore, friction factor  $\theta$  should be calculated from  $K_D$ , Reynolds number of a tangential entry  $Re_p$  and friction coefficient  $\lambda_k$  to obtain the equivalent spray angle in viscous flow  $\alpha_{eq}$  [Sterling and Sleicher, 1975].

$$\theta = \frac{\lambda_k}{2} K_D \left( \frac{r_k}{r_o} - 1 \right), \quad Re_p = \frac{\dot{m}_l}{\frac{\pi}{4} \mu_l d_p \sqrt{n}} \quad (2.13)$$

$$\text{where } \lambda_k = \frac{1.22}{Re_p^{0.36}} \left( Re_p > 2.3 \times 10^3 \right), \quad \lambda_k = \frac{24.6}{Re_p^{0.75}} \left( Re_p < 2.3 \times 10^3 \right)$$

$$\bar{\alpha} = \frac{\alpha_{eq}}{\alpha_{ideal}} = f(\theta) \quad \rightarrow \quad \alpha_{eq} = \bar{\alpha} \times \alpha_{ideal} \quad (2.14)$$

In the swirl injector, hydraulic losses caused by friction can be found at the tangential entry, wall of the vortex chamber, and the converging part [Bayvel, 1993; Borodin et al., 1968; Dityakin et al., 1977]. These losses change the discharge coefficient and the required injection differential pressure.

First, the energy loss at tangential entry  $\Delta_{in}$  can be determined in Eq. 2.15.

$$\Delta_{in} = \xi_{in} \frac{K_D^2}{C^2}; \quad C = \frac{R}{r_0} \quad (2.15)$$

The energy loss at the wall of the vortex chamber  $\Delta_k$  can be calculated by Eq. 2.16

$$\Delta_k = \frac{\lambda_k}{\sigma^2} \left\{ \frac{1}{\sigma} \left( 1 - \frac{1}{C_k} \right) + \lambda_k \left[ \left( \frac{K_e}{2} - \frac{1}{2\sigma - \lambda_k} \right) \left( \frac{2}{\sigma} + \frac{K_e}{2} + \frac{1}{2\sigma - \lambda_k} \right) + \frac{3}{2\sigma^2} \ln \frac{(2\sigma - \lambda_k) K_e C_k}{2} \right] \right\}; \quad (2.16)$$

$$\text{where } \sigma = \frac{1}{K_e} + \frac{\lambda_K}{2} C_K, \quad K_e = \frac{K_D}{1+\theta}, \quad C_K = \frac{r_K}{r_0}$$

The energy loss due to swirl chamber wall length  $\Delta_L$  is in Eq. 2.17.

$$\Delta_L = \frac{K_D^2}{2C_K} (1 + C_{d,pr} K_D C_K) \left[ 1 - \frac{1}{\left(1 + \theta \frac{C_K}{C_K - 1} \bar{\lambda} \cdot \bar{L}_K\right)^{-2}} \right] \quad (2.17)$$

$$\text{where } \bar{\lambda} = 1.0, \quad \bar{L}_K = \frac{L_K}{D_K}, \quad K_{pr} = K_D C_K = \frac{(1 - \varphi_{pr}) \sqrt{2}}{\varphi_{pr}^{1.5}}, \quad C_{d,pr} = \sqrt{\frac{\varphi_{pr}^3}{2 - \varphi_{pr}}}$$

Finally, energy loss at converging part  $\Delta_{noz}$  is in Eq. 2.18.

$$\Delta_{noz} = \frac{\xi_{noz}}{\varphi_\theta^2} \quad (2.18)$$

In Eq.18, the hydraulic resistance  $\xi_{noz}$  is affected by contraction angle  $\psi$ :  $\xi_{noz} = 0.11$  at  $\psi = 90^\circ$  and  $\xi_{noz} = 0.16$  at  $\psi = 120^\circ$ .

Considering the energy losses mentioned above, the equivalent discharge coefficient  $C_{d,eq}$ , geometric constant  $K_{eq}$ , and injection differential pressure  $\Delta P_{eq}$ .

$$C_{d,eq} = \frac{1}{\sqrt{\left(\frac{1}{\varphi_\theta^2} + \frac{K_{eq}^2}{1 + \varphi_\theta} + \Delta_{sum}\right)}} \quad ; \quad \Delta_{sum} = \Delta_K + \Delta_{in} + \Delta_{noz} + \Delta_L \quad (2.19)$$

$$K_{eq} = \frac{K_D}{1 + \theta \left(1 + \frac{C_K}{C_K - 1} \bar{\lambda} \bar{L}_k\right)} \quad (2.20)$$

$$\Delta P_{eq} = \frac{\Delta P_{ideal}}{\left(\frac{C_{d,eq}}{C_d}\right)^2} \quad (2.21)$$

### 2.1.2 High-pressure chamber

The combustion chamber of the liquid propellant rocket engine operates under high pressure and temperature. In this conditions, behavior of the liquid flow is much different from those at atmospheric conditions [Lefebvre, 1989; Strakey et al., 2001]. Therefore, the high-pressure chamber was used in the experiments to control the conditions surrounding the flow.

The schematic and the photograph of the chamber is shown in Fig. 2.2. The chamber was pressurized by gas nitrogen. Although the endurance pressure of the chamber was designed to 12 MPa, the maximum available working pressure was 6 MPa for safety. Because the maximum working pressure exceeds the critical pressure of the nitrogen (3.39 MPa), the experiment under supercritical condition for the injected flow was available. Since the chamber pressure was increased when the flow was injected and vaporized, the controller automatically reduced and maintained the chamber pressure by sensing the chamber pressure and then opening and closing the exhaust valve. The inner diameter of the chamber was 500 mm and the length was 1,000 mm; total inner volume of the chamber was 200 L. The injector was mounted on the transporting device inside the chamber. This device was able to vertically transverse and rotate under pressurized situations.

Six quartz windows with 80 mm in diameter were located on the chamber for optical access to the flow. Four windows were located around the chamber, and one window port was inclined with 30° angle in order to be used for PDPA measurements. To avoid the deposition of droplets on the window surface, inner surface of the windows were 300 mm apart from the inside wall of the chamber. Air curtain system also was installed to prevent droplets from the windows.

The chamber was originally used for a cold flow water injection test [Kim et al., 2007]. Therefore, it was slightly modified for the experiment of cryogenic fluid injection [Cho et al., 2014]. The K-type thermocouple was mounted to measure the temperature inside the chamber, and the water feeding line was changed to the vacuum-insulated flexible tube. The sealing material of the chamber was changed from PTFE o-ring to Viton o-ring which endures lower temperature. Similar consideration was applied to the valves used for the operation of the chamber.

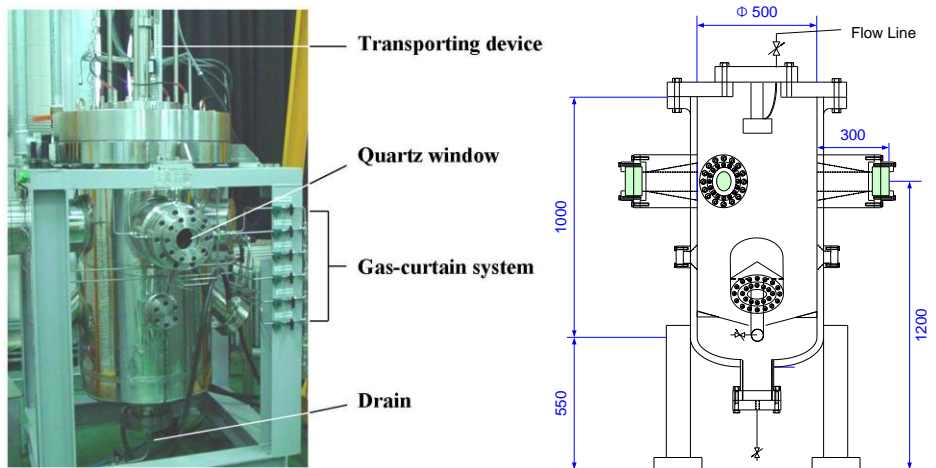


Fig. 2.2 High-pressure chamber

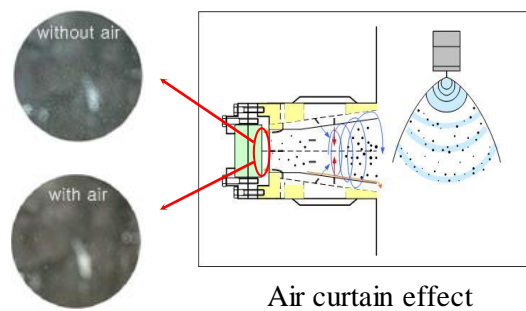


Fig. 2.3 Air curtain system

### 2.1.3 Cryogenic fluid feeding system

The liquid nitrogen was used as working fluid in the experiment. Because of the cryogenic temperature of the fluid, prevention of the heat transfer to the fluid was required. The high pressure condition of the fluid also increased difficulty of the experiment. Therefore, specially designed fluid feeding system was used in this study.

The schematic of the cryogenic fluid feeding system is shown in Fig. 2.4. The cryogenic fluid feeding system contained a run tank, a pressurizing component, and a flow feeding line [Cho et al., 2014]. In the experiment, the run tank was filled with liquid nitrogen and pressurized using nitrogen gas. The cryogenic liquid was fed to the injector via the control of the tank pressure. The run tank and the flow feeding line were vacuum-insulated to minimize the vaporization of the cryogenic liquid caused by heat transfer from outside. The maximum available working pressure of the system was 8 MPa. Sensors, such as thermocouples, pressure transducers, and a turbine flowmeter were installed at the run tank and a flow line to measure the state of the flow inside the system.

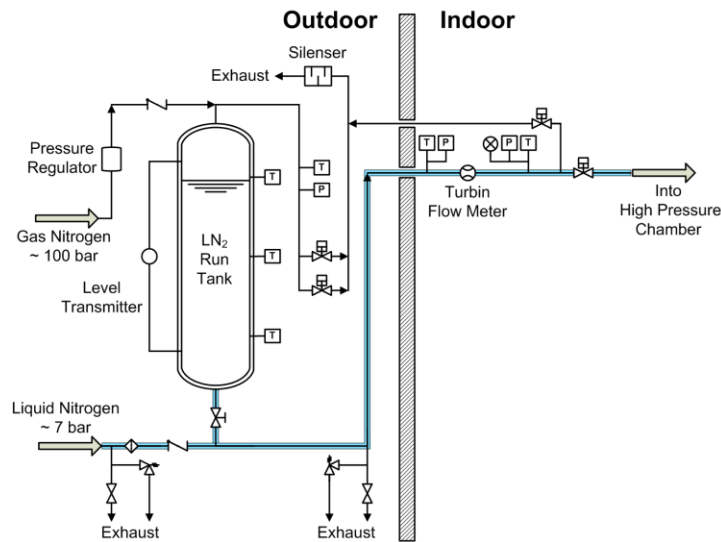


Fig. 2.4 Cryogenic fluid feeding system

## **2.2 Flow Measurement**

The purpose of flow measurement is the investigation of fluid state and the flow behavior. Therefore, the properties of the fluid such as pressure, density and temperature are mainly measured first. The characteristics representing the flow behavior, such as the flow image, velocity and instability frequency, can be also measured. Meanwhile, because of the instability which exist in the cryogenic flow, temporal flow measurement technique was also required.

In research of flow under supercritical conditions, harsh condition for the experiment constrained the measurement of flow characteristics. The first related study conducted in DLR [Mayer and Tamura, 1996] conducted qualitative analysis of the single shot flow image. With the development of the investigation technique, the properties of the fluid were measured by non-intrusive laser diagnostics [Chehroudi et al., 2002a; Decker et al., 1998; Mayer et al., 2003; Oschwald and Schik, 1999] and intrusive measurement [Davis and Chehroudi, 2007]. Although these works investigated important flow characteristics, the dynamic characteristics could not be obtained. Therefore, other studies used flow images to conduct temporal analysis of the flow [Teshome et al., 2012; Wegener et al., 2014].

Optically dense region of the flow was measured in this study. High-speed photography with backlight imaging was used, and instability frequency measurement was conducted. These methods enabled both temporal and spatial analysis of the cryogenic swirl flow. To ensure that the injectant is in liquid state, measurement of pressure and temperature was conducted at the injector manifold as shown in Fig. 2.5.

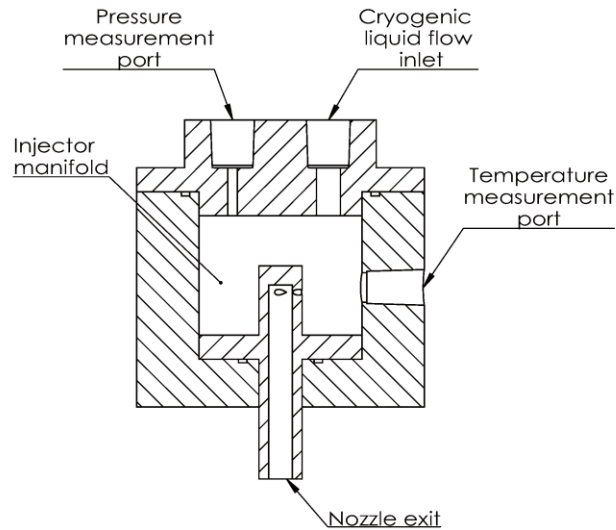


Fig. 2.5 Flow condition measurement inside swirl injector

### 2.2.1 High-speed photography

The characteristics of the flow behavior were investigated via qualitative and quantitative analyses of flow images. In the experiments, the shape of the cryogenic flow was unstable because of its rapid phase change caused by the huge temperature difference between the flow and its surroundings. Therefore, a temporal measurement of the characteristics of the flow was required to study the flow dynamics. Various methods have been employed for the measurement of cryogenic flow, such as shadowgraphy [Chehroudi et al., 2002b; Mayer et al., 2001], Raman scattering [Oschwald and Schik, 1999], and direct measurement of the flow temperature [Davis and Chehroudi, 2007]. Among these methods, Raman scattering and temperature measurement can best determine the quantitative characteristics; however, they are not suitable for measurement of the temporal change of the flow. In addition, the flow image obtained by the shadowgraphy method is sensitive to density variation in the flow field. Because the cryogenic swirl flow, which interacts highly with its surroundings, can affect the density

of the surrounding environment, a distorted flow image can be acquired using shadowgraphy. Considering the abovementioned problems in flow measurement, we chose the use of high-speed photography with backlight imaging for this study.

A schematic of the flow imaging is shown in Fig. 2.6. To obtain a fixed flow image, a Photron Fastcam APX camera was used for high-speed flow imaging. The frame rate of the photography was set at 10,000 frames/sec and the exposure time was  $10 \mu\text{s}$ . A Macro lens (Canon 180 mm Macro) was used to capture the enlarged flow images. A high-power continuous light source (Photron HVC-SL Xenon lamp) was used as backlighting source because the fast phase change of the injectant increases the opacity of the imaging area. Meanwhile, tracing paper was located between the backlight and the flow to flatten the background brightness.

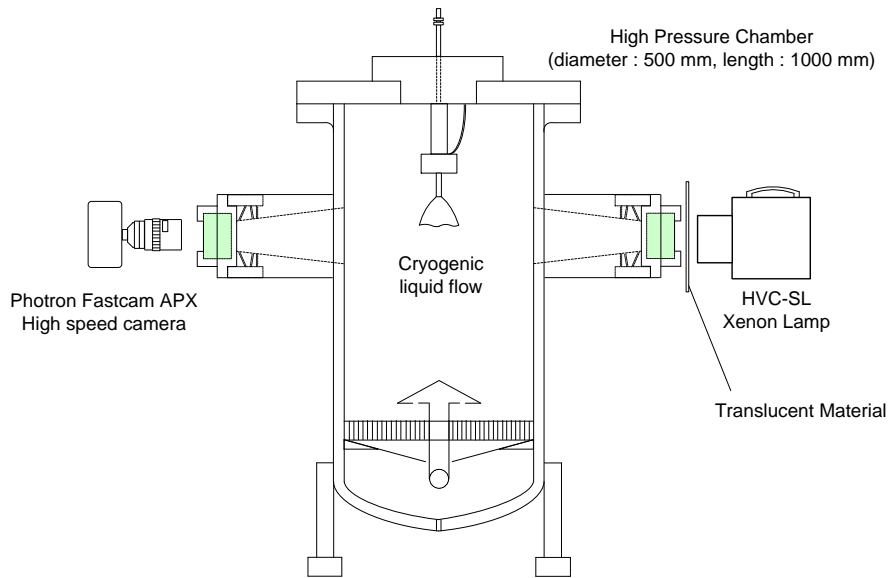


Fig. 2.6 High-speed photography

### 2.2.2 Flow instability frequency measurement

The serious flow instability was observed in the experiment. The oscillation of the flow generated optically dense and sparse regions periodically, and the specific frequency was found. For the quantitative analysis of the instability, flow instability frequency was measured via laser diagnostics method. A schematic of the frequency measurement, which is similar to the flow oscillation measurement system used in a previous study [Im et al., 2009], is shown in Fig. 2.7.

The instability frequency of the flow was measured 5 mm downward from the injector post. A laser line beam (Ar-Ion,  $\lambda_{laser} = 514.5$  nm) was passed through the center of the flow, and the beam intensity was measured via a photodetector with a measurement time of 1 s and a sampling rate of 100 kHz. When the flow region changed due to the instability of the flow surface, the intensity of the laser line beam passing through the flow also changed periodically. From the measured beam intensity, the transmission rate of the laser beam over time was calculated. By means of a spectral analysis, the power spectral density of the transmission rate was calculated and the flow instability frequency was measured.

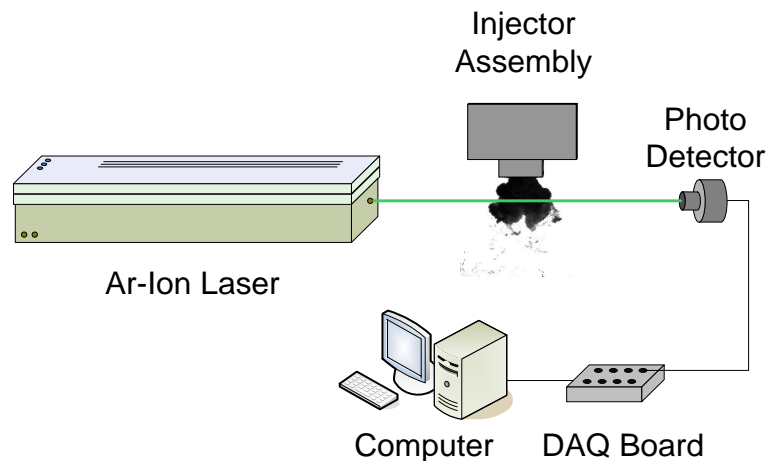


Fig. 2.7 Flow instability frequency measurement using Ar-Ion laser

# **CHAPTER 3**

## **SURFACE INSTABILITY ON CRYOGENIC SWIRL FLOW UNDER SUB- TO SUPERCRITICAL CONDITIONS**

### **3.1 Background and Objectives**

Because recently developed liquid-propellant rocket engines are required to maintain a high level of performance, the engines work under high pressures and temperatures, and a considerable amount of liquid-state propellant is injected into their combustion chambers and burned. As a result, the temperature and pressure in the engine combustion chamber exceed the critical properties of the injected propellant, the phase of which is changed from a liquid to a supercritical fluid through a transcritical process [Schmitt et al., 2012; Yang, 2000]. In this situation, the injected flow is dominated by supercritical fluid characteristics, which include thermophysical properties such as near-zero surface tension and high diffusivity [Oschwald and Schik, 1999]. The conventional model of a liquid flow or spray cannot be adopted [Chehroudi et al., 2002b; Yang, 2000], and the flow characteristics under supercritical conditions must be investigated.

Many studies of cryogenic fluid injection under supercritical conditions have been conducted in Europe and the United States (US). Because the rocket engines developed in these countries mainly used impinging jet injectors (the F-1 engine for the Saturn V) or shear coaxial injectors (the space shuttle main engine and the Vulcain engine for the Arian-5), most studies have concentrated on single or coaxial jet flows and used experimental or numerical methods. Mayer et al. [Mayer and Tamura, 1996; Mayer et al., 2001; Mayer et al., 1998] studied single and coaxial jet flows under non-reacting and reacting conditions and qualitatively observed changes in the flow behavior under various conditions. They found that the atomization process of a cryogenic liquid jet was similar to that of ordinary jets under subcritical conditions, but that the jet showed gas-like

behavior under supercritical conditions [Mayer et al., 2001; Mayer et al., 1998]. During a coaxial reacting flow, it was found that the recirculation zone near the injector tip worked as a flameholder [Mayer and Tamura, 1996]. Chehroudi et al. [Chehroudi, 2010; Chehroudi et al., 2002b; Davis and Chehroudi, 2007] investigated the characteristics of liquid nitrogen jets. These jets behave as a variable-density gas jet under supercritical conditions [Chehroudi et al., 2002b]. The acoustic wave on the coaxial cryogenic jet shortens the dark core length under a subcritical condition [Davis and Chehroudi, 2007], and the sensitivity of the jet core length then affects the combustion instability in a liquid rocket engine [Chehroudi, 2010]. Studies using numerical analyses have also been conducted. The behavior of a non-reacting single jet [Oefelein and Yang, 1998; Zong et al., 2004] and the mixing characteristics of a reactive coaxial jet [Miller et al., 2001; Oefelein and Yang, 1998] were investigated. The results from the analyses were in good agreement with those obtained in experiments.

Instead of jet injectors, swirl-type injectors have been used in many other rocket engines, especially those developed in Russia. A swirl injector creates a hollow cone-shaped spray to distribute the injectant over a larger area than a jet to enhance mixing. It also has a simple structure which is designed to maintain high reliability, and it can be used in various heat engines (i.e., rocket engines, gas turbines and boilers) [Lefebvre, 1989].

Most studies of the characteristics of swirl injectors have focused on the atomization characteristics of the injected liquid flow under subcritical conditions. During a liquid swirl spray, the growth of the surface wave and the nonlinear effect on the unstable liquid sheet determine the breakup length [Clark and Dombrowski, 1972; Dombrowski and Johns, 1963; Han et al., 1997; Kim et al., 2007], and a roll-up vortex structure arising from the liquid sheet surface dominates the atomization process of the spray [Park and Heister, 2006]. The instability of the flow was also studied because it forms the wave on the liquid sheet and causes atomization. Marchione et al. [Marchione et al., 2007] measured the angle of a liquid kerosene swirl spray and found that the angle changes periodically. A fiber-optic method was used to measure the instability frequency of a

water swirl spray at various positions. It was found that two types of instability exist on the liquid sheet: large-amplitude low-frequency instability and small-amplitude high-frequency instability [Musemic et al., 2009]. Other studies investigated the dynamic characteristics of coaxial sprays from spray images, especially the self-pulsation phenomena [Eberhart et al., 2012; Im et al., 2009].

Though the substantial characteristics of a cryogenic fluid injection at supercritical conditions and those of a liquid swirl injection were investigated separately, studies have rarely been conducted on cryogenic swirl flows under supercritical conditions. NASA's Marshall Space Flight Center [Hutt and Cramer, 1996] found different disintegration processes of liquid oxygen swirl flows under subcritical and supercritical conditions during the starting process of a rocket engine combustion test. Zong et al. [Zong and Yang, 2008] conducted a numerical analysis of liquid oxygen swirl flows under supercritical conditions and found that the precessing vortex core (PVC) on the boundary of the central toroidal recirculation zone (CTRZ) and Kelvin-Helmholtz instability dominated the instability of the flow outside the injector. Heo et al. [Heo et al., 2012] also investigated the mixing and instability characteristics of swirl coaxial flows under supercritical conditions. However, more detailed research is still required. The behaviors of swirl flows under sub- to supercritical conditions should be investigated by an experimental approach, and the obtained results have to be compared to previously predicted flow characteristics.

This study investigated the characteristics of cryogenic swirl flows via experiments. Because the flow characteristics are determined by flow instability, and given that this phenomenon appears on the flow surface, images of the flow surface were obtained and analyzed. First, the surface characteristics of the flow were observed and compared to those of a liquid flow under a similar condition in a qualitative manner. Also, changes in the flow surface behavior under sub- to supercritical conditions were investigated. Finally, the instability frequency of the flow was measured and discussed.

## 3.2 Experimental Methods

### 3.2.1 Injector design

The cryogenic swirl flow was injected from an open-type simplex swirl injector mounted inside the chamber. A schematic of the injector is shown in Fig. 3.1, and its geometry is detailed in Table 3.1. The inner diameter of the injector is 5 mm, which is similar to the geometry of the injector used in previous work [Zong and Yang, 2008]. The swirling part of the injector has three tangential holes. The swirl injector's geometrical characteristic parameter  $K$ , which is an important geometric parameter of swirl injectors [Bazarov and Yang, 1998], is 4.4. In the experiment, nitrogen was not injected in a liquid state until the injector was sufficiently cooled. Therefore, a T-type thermocouple and a pressure transducer were used to measure the condition inside the injector manifold and to ensure that the state of the injected flow was liquid.

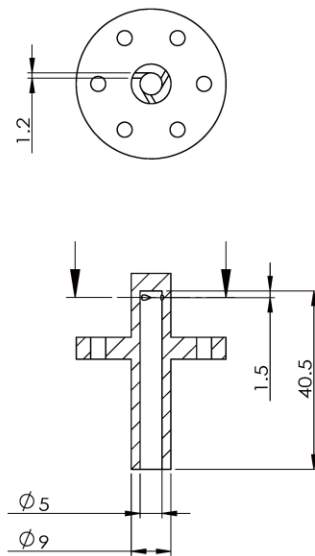


Fig. 3.1 Open-type simplex swirl injector (unit: mm)

Table 3.1 Injector geometry

Injector part	Geometry, mm
Nozzle length, $L_o$	40.5
Nozzle diameter (inner), $d_{o,i}$	5
Nozzle diameter (outer), $d_{o,o}$	9
Tangential inlet diameter, $d_p$	1.2
Number of tangential inlet, $n$	3
Injector geometrical characteristic parameter $K = (d_{o,i} - d_p)d_{o,i}/nd_p^2$	4.4

### 3.2.2 Experimental conditions

The injection differential pressure ( $\Delta P$ ) and ambient pressure ( $P_c$ ) were controlled during the experiment.  $\Delta P$  was maintained at 0.5 MPa and 1 MPa, and the resulting mass flow rates were approximately 50 g/s and 65 g/s, respectively.  $P_c$  was increased to 4 MPa, which is above the critical pressure of nitrogen. The ambient temperature,  $T_c$ , was held at approximately 270 ~ 280 K. As the critical properties change drastically with a slight change of the mixture ratio in gas mixtures [Mayer et al., 2001], nitrogen gas was used as the surrounding gas to maintain the critical properties during the experiment. Under these experimental conditions, the cryogenic liquid was injected into the chamber at sub-, near-, and supercritical pressures. The injection temperature measured at the manifold of the injector was close to the saturation temperature.

Detailed experimental conditions are shown in Fig. 3.2 and Table 3.2. In Fig. 3.2, initial and final condition of the injectant for each experimental case are pointed in Pressure-Temperature diagram of nitrogen, and each points are connected with a solid line. The initial condition point indicates the pressure and temperature condition of the

injectant measured at the injector manifold as mentioned in section 2.2, and it is located at the left side of the figure which means that the nitrogen is in liquid state. In contrast, the final condition point indicates the condition of the high-pressure chamber and located at the right side of the figure.

For the cases that the pressure of the initial condition is above 3.5 MPa, it can be thought that the injected liquid nitrogen might become supercritical fluid in the injection process. In addition, for some experimental cases ( $\Delta P = 1$  MPa,  $P_c \geq 3.4$  MPa), the fast phase change of the injectant disrupted the visualization of the flow, and high-speed photography was not available.

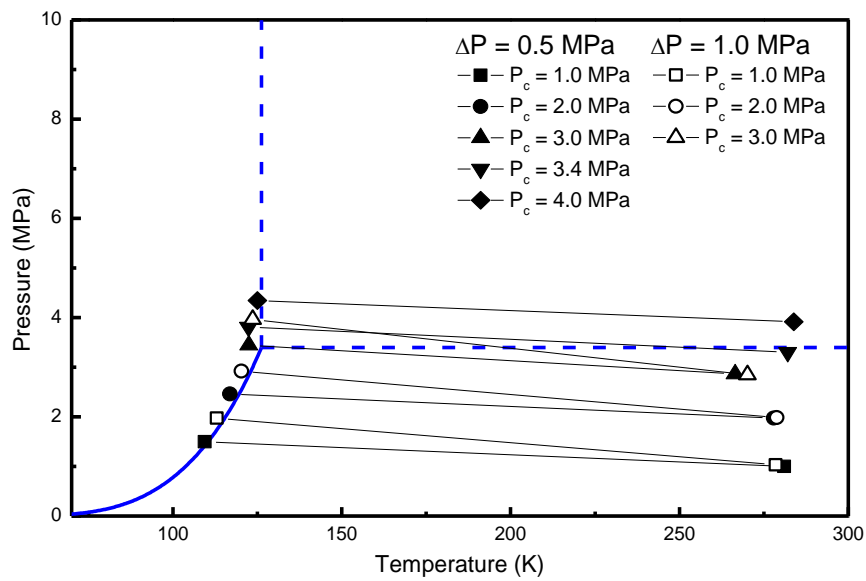


Fig. 3.2 Experimental conditons in Pressure-Temperature diagram of nitrogen

Table 3.2 Experimental conditions

Flow condition	Range
Injection differential pressure (MPa)	0.5/1
Ambient pressure (MPa)	1, 2, 3, 3.4, 4
Injector manifold temperature (K)	105~125
Ambient temperature (K)	280

### 3.2.3 Experimental techniques

The characteristics of the flow surface were investigated via qualitative and quantitative analyses of flow images. Because the cryogenic swirl flow is rapidly vaporized by the temperature difference between the flow and its surroundings, the shape of the flow changes quickly. In this case, high-speed photography with a short exposure time was used to obtain a fixed image to enable a temporal analysis of the flow. The frame rate was 10,000 frames per second, and the exposure time was maintained at 10  $\mu$ s. The imaging area was 28.8 (width)  $\times$  28.8 (height) mm<sup>2</sup>, and the pixel size was 112.5  $\mu$ m. The detailed explanation of this method is in section 2.2.1.

The instability frequency of the flow was measured 5 mm downward from the injector post. This method is similar to the flow oscillation measurement system used in a previous study [Im et al., 2009]. An intensity of the laser line beam measured via a photodetector with a measurement time of 1 s and a sampling rate of 100 kHz. By means of a spectral analysis, the power spectral density of the transmission rate was calculated and the flow instability frequency was measured. The detailed explanation is in section 2.2.2.

## **3.3 Results and Discussion**

### **3.3.1 Characteristics of the cryogenic swirl flow**

Previous studies [Mayer et al., 1998; Oswald and Schik, 1999] noted that cryogenic flows are highly affected by vaporization. Therefore, it is necessary to determine the important characteristics of a cryogenic flow as compared to a common liquid flow before an investigation of a cryogenic flow under sub- to supercritical conditions. To find the unique characteristics of the cryogenic flow studied here, a liquid nitrogen flow and water spray injected from the same injector were compared. To ensure a proper comparison, the experimental conditions were equivalent for each flow. The injection differential pressure was set to 0.5 MPa, and the ambient pressure was set to 2 MPa in order to keep the injectant in a liquid state.

Images of the cryogenic swirl flow and the water swirl spray are shown in Fig. 3.3(a) and Fig. 3.3(b), respectively. The atomization process of the conventional liquid swirl spray can be explained by Dombrowski's hypothesis [Clark and Dombrowski, 1972; Dombrowski and Johns, 1963]. During the atomization process, in which the gas surrounding the liquid sheet is stationary and the vaporization effect can be ignored, a small perturbation is imposed on the liquid sheet and the wave travels along the flow. In the liquid sheet, the amplitude of the surface wave increases to a certain value [Dombrowski and Johns, 1963], and two waves with different modes (sinusoidal and symmetric) are superimposed on the sheet. The thickness of the sheet becomes zero at a certain position where breakup occurs [Clark and Dombrowski, 1972]. Meanwhile, owing to Kelvin-Helmholtz instability, a vortex ring structure develops on the surface and affects the breakup process, ligaments, and droplet diameter [Park and Heister, 2006]. This process is shown in Fig. 3.3(b).

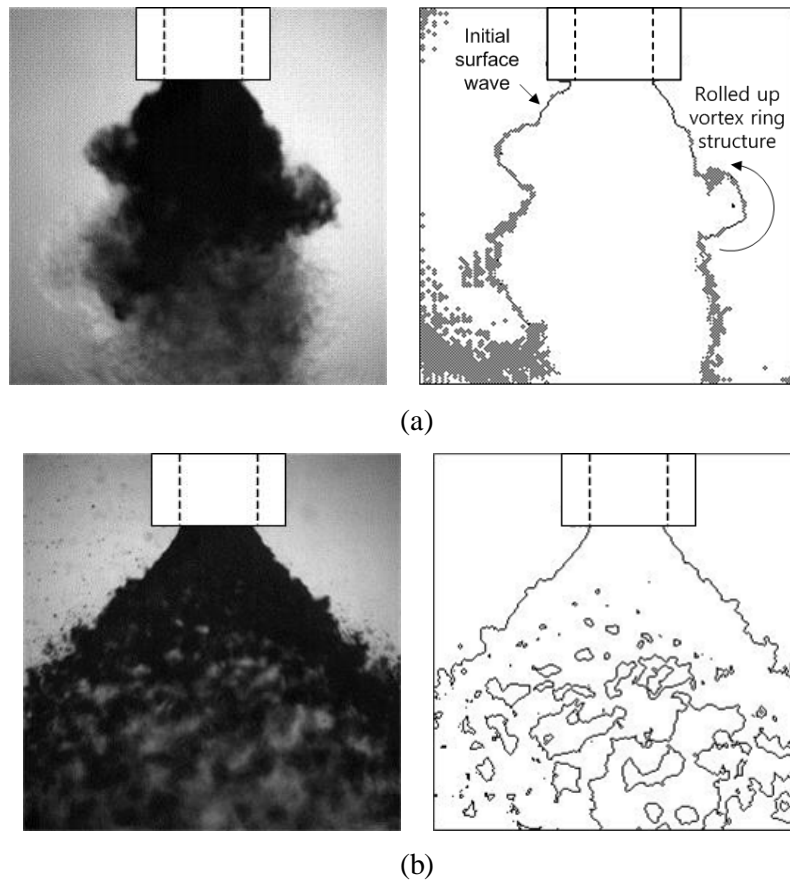


Fig. 3.3 Instantaneous swirl flow image at  $\Delta P = 1$  MPa,  $P_c = 1$  MPa for (a) cryogenic swirl flow and (b) water swirl flow; (left) original image and (right) flow boundary

In the cryogenic swirl flow studied here, however, an unstable helical wave structure was found on the flow surface, and a liquid lump which became detached from the flow was observed. These characteristics of the cryogenic swirl flow are rather similar to that of a gas swirl jet [Syred, 2006], a cryogenic swirl flow under a supercritical condition [Zong and Yang, 2008], and a swirl liquid jet with a precessing flow structure inside the flow [Liang and Maxworthy, 2005]. From these findings, it can be hypothesized that the PVC in the CTRZ dominates the instability of the cryogenic swirl flow; thus, the

assumption of the stationary surrounding gas condition, following Dombrowski's hypothesis, is no longer appropriate. According to PVC instability, a helical vortex structure is created in the flow, and the injected flow causes the recirculation of the surrounding gas, after which gas is entrained on the flow surface. Finally, the wavy structure on the surface is rolled up [Han et al., 1997]. In this flow, droplets from the atomization process were not observed, and the amplitude of the wave structure and the roll-up vortex was significantly larger than that of the water flow. These differences indicate a serious phase change in the flow.

As mentioned earlier, small droplets were not observed during the cryogenic liquid flow. One reason for this absence is the considerable temperature difference between the flow and the surrounding area, which causes the fast vaporization of the small flow structure or the detached fluid, making flow visualization impossible. Another reason may be the brightness of the backlight, which was high enough to saturate the image sensor and prevent the visualization of the small fluid structure. Instead of droplets, liquid lumps that disintegrated from the flow were found. They were approximately 1 mm in size, similar to the scale of the surface structure found in the water flow.

The size of the wave and the roll-up vortex structure at the flow surface was larger for a cryogenic flow than for the water flow due to the differences in the properties of liquid nitrogen and water. Because its viscosity and surface tension are less than 10% of those of water [Linstrom and Mallard], the inertial force affects the cryogenic flow more than the viscous force or surface tension force. Earlier studies [Dombrowski and Johns, 1963; Senecal et al., 1999] implied that the growth rate and wave number would be smaller for a flow with lower viscosity. The result obtained from this study supports such a prediction.

### **3.3.2 Effect of the ambient pressure on the characteristics on a cryogenic swirl flow surface**

The ambient pressure would affect the behavior of liquid swirl spray [Kenny et al., 2009; Kim et al., 2007; Lefebvre, 1989], and the behavior of the cryogenic jet flow would change significantly when the ambient pressure changes from sub- to supercritical conditions for the injectant [Chehroudi et al., 2002b; Hutt and Cramer, 1996; Mayer et al., 1998]. Therefore, the effect of the ambient pressure on the cryogenic swirl flow was studied. The static and dynamic characteristics of the flow were investigated via a flow image analysis.

Instantaneous and averaged flow images acquired via high-speed photography with backlight imaging under various ambient pressure conditions are shown in Fig. 3.4. Representative flow images under subcritical and supercritical conditions are compared in Fig. 3.5. In the flow images, the dark region represents the flow in a liquid state. The downstream flow after a breakup or phase change can be distinguished from the surroundings. In each flow region, the flow characteristics of the behavior of the flow at the boundary, the spray angle, and other characteristics of the wave structure on the flow surface were investigated. Spatial and temporal analyses were conducted by processing the flow image. Matlab™ was used for the processing of the flow image and the analysis. During the processing steps, the flow boundaries were detected using the graythresh function which selects an appropriate threshold value based on Otsu's method [Teshome et al., 2012], and by creating a binary image from the original flow image.

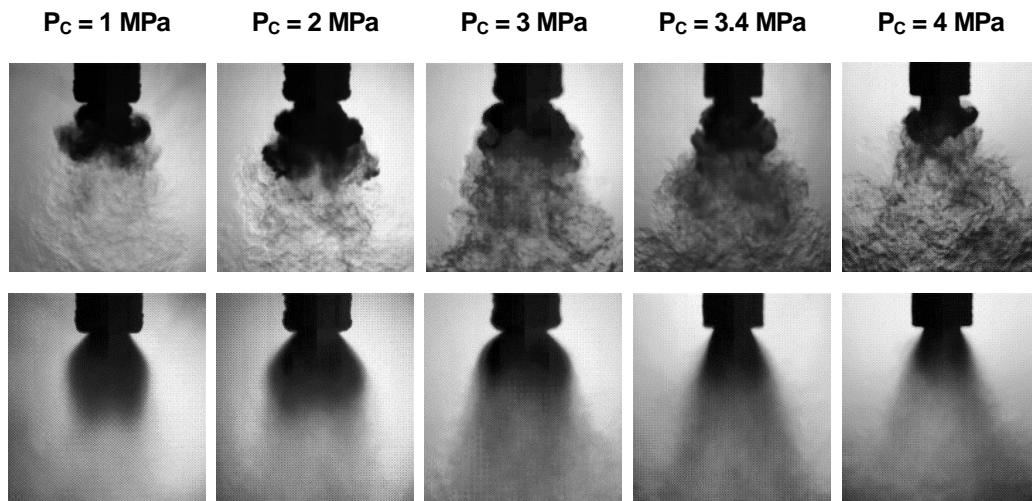


Fig. 3.4 Representative swirl flow images under various ambient pressure conditions for instantaneous image (top row) and averaged image (bottom row) at  $\Delta P = 0.5 \text{ MPa}$

The shape of a common liquid swirl flow is a hollow cone. In a liquid flow region, the flow is slightly contracted along the flow's axial direction under subcritical conditions. When comparing liquid state flows near the injector post, the flow area was larger for a flow in a subcritical condition than it was for a flow in a supercritical condition. Under supercritical conditions, a roll-up vortex structure was found on the flow surface near the injector post, whereas a wave structure was not found. The shape of the injected flow is different from flow under subcritical conditions, for which the surface structure is initially in the shape of a sinusoidal wave and changes to a roll-up vortex, as shown in Fig. 3.3(a) and Fig. 3.5(a), respectively.

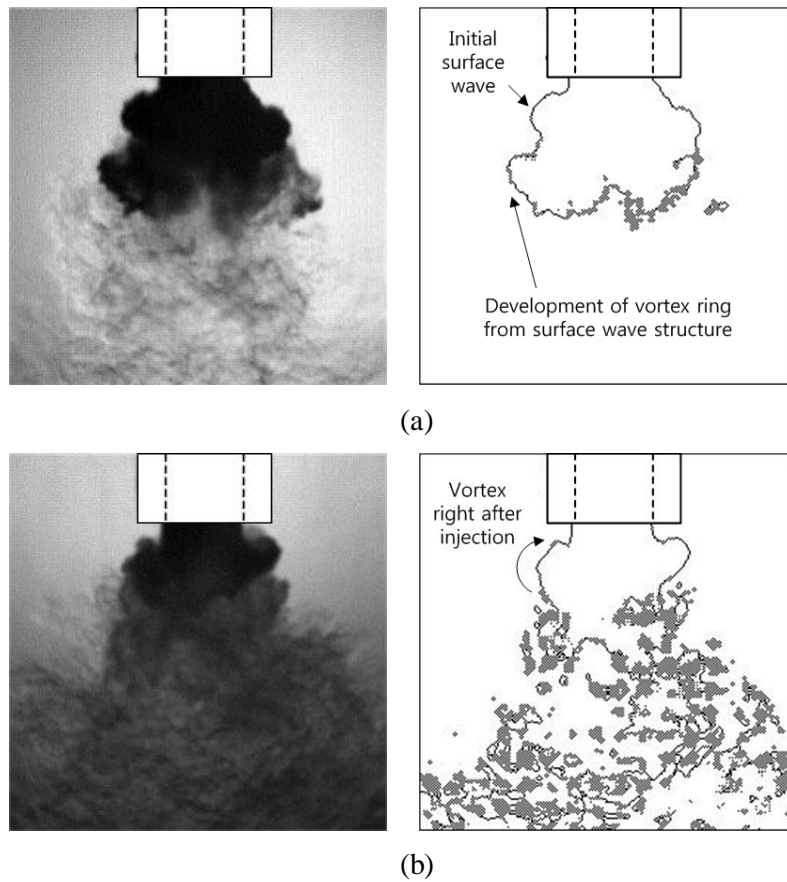


Fig. 3.5 Instantaneous swirl flow image at  $\Delta P = 0.5$  MPa for  
 (a)  $P_c = 2$  MPa (subcritical conditions) and (b)  $P_c = 4$  MPa (supercritical conditions);  
 (left) original image and (right) flow boundary

For a quantitative analysis of the flow in a liquid state, the spray angle was measured from the flow image. The spray angle, which represents the distribution and mixing characteristics of the flow, was measured from the averaged flow image under each condition in the second row of Fig. 3.4. These results are shown in Fig. 3.6. Due to the difficulty involved in boundary detection after a breakup or phase change, the spray angle

was measured near the injector post, where the injectant remains in a liquid state and where the flow is distinguishable from the surroundings. In Fig. 3.6, the measured spray angle under each condition is compared to the results of an empirical equation suggested in a previous work [Fu et al., 2012] regarding the geometric characteristics of open-type injectors and the Reynolds number at a tangential inlet. This research used water as the working fluid, and it was conducted under atmospheric pressure conditions. Due to the similarity of the injector geometry between present study and previous work, it was expected that the experimental results would be similar in terms of the tendencies whereas the values of the results would differ because of different flow conditions. However, the spray angle suggested in the previous work was different from the measured spray angle both qualitatively and quantitatively. While the spray angle remains almost constant in theory and in the experiments [Fu et al., 2012; Kenny et al., 2009; Kim et al., 2007; Lefebvre, 1989] for a common liquid flow, the surface of the cryogenic flow is unstable and the measured angle can increase with the ambient pressure [Kim et al., 2007]. In addition, the larger length-to-diameter ratio of the injector in this experiment caused an increase in the amount of momentum loss inside the injector and a decrease in the measured spray angle as compared to the predicted value. Meanwhile, the angle was decreased sharply when the surroundings were changed from subcritical to supercritical conditions, as in an earlier work [Hutt and Cramer, 1996]. This may have been caused by the drastic change of the physical properties of the injectant, especially the viscosity and the surface tension. However, these properties do not affect the spray angle of the liquid swirl flow under subcritical conditions [Lefebvre, 1989]. In this case, the effects of these properties under supercritical conditions should be considered. While the spray angle of the swirl flow can be denoted as  $\alpha = 2 \tan^{-1} (w/u)$ , where  $w$  is the tangential velocity and  $u$  is the axial velocity of the flow, a decrease of the azimuthal velocity causes a decrease in the spray angle. Under supercritical conditions, the surface tension is diminished and the dissipation of the velocity from the liquid surface to the air core occurs more intensely for the azimuthal component than it does for the axial component [Zong and Yang, 2008], which ultimately causes a significant decrease in the spray angle.

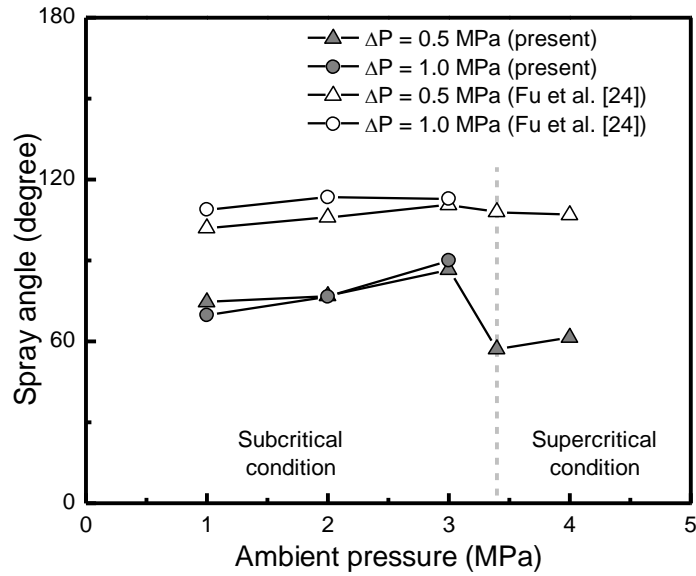


Fig. 3.6 Spray angle of cryogenic swirl flow

After a breakup or phase change, the injected flow remained downstream and could be clearly distinguished from the surroundings, as shown in Fig. 3.5. Under subcritical conditions, though the state of the injected flow changed from liquid to gas, the temperature difference between the downstream area and the surroundings remained large and tiny flow structures were observed, indicating the existence of a density gradient. The downstream flow was contracted and moved downward, and vortices were found at the boundary of the flow region. This behavior is similar to that of droplets created by the atomization of a conical liquid sheet, meaning that the decrease in the azimuthal velocity was larger than the decrease in the axial velocity in the downstream flow. Under supercritical conditions, in contrast, the downstream flow had higher visible opacity and its spreading angle was maintained. In this condition, the state of the injectant changed from a gas to a supercritical fluid and its density changed moderately. Because the opacity of a fluid is related to its density, the opacity of the downstream flow changes less.

Moreover, the effect of the momentum loss on the injected flow will be less than that on the flow under subcritical conditions, where the density changes significantly during the phase change from liquid to gas.

In a cryogenic swirl flow, a wave is imposed on the flow surface and creates a wavy structure periodically, which causes instability of the flow, as shown in Fig. 3.7(a). Therefore, the characteristics of the wave on the flow surface were investigated from an instantaneous flow boundary image in order to determine the characteristics of the instability. The flow surface was assumed to have a sinusoidal wave shape and was assumed to be fitted to a sinusoidal wave, the form which is as follows:  $\eta(x, t) = \eta_0 \exp i(kx - \omega t)$ , where  $x$  is the distance from the injector post along the liquid sheet,  $t$  is the time,  $\eta_0$  is the amplitude of the wave,  $k$  is the wave number, and  $\omega$  is the growth rate. The wavelength  $\lambda$  was calculated from  $k$  via  $\lambda = 2\pi/k$ . The characteristics of the surface wave (i.e., wave amplitude, wavelength) were calculated via the curve fitting function “fit” in Matlab™. Due to PVC instability, a wavy vortex structure was generated on the flow surface, and it changed to a roll-up vortex due to the entrainment of the surrounding gas on the flow surface. Therefore, the growth rate could not be measured. The propagation velocity of the wave,  $v$ , was calculated by measuring the displacement of the flow structure along the liquid sheet. The detailed process of the flow image analysis is shown in Figs. 3.7(b) and (c).

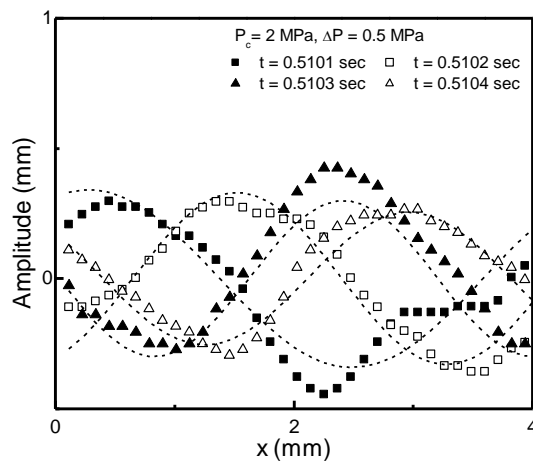
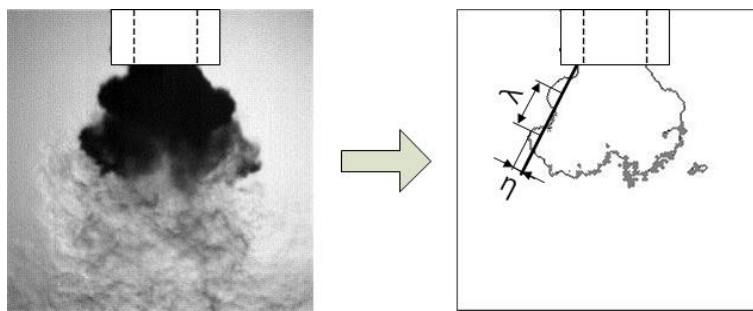
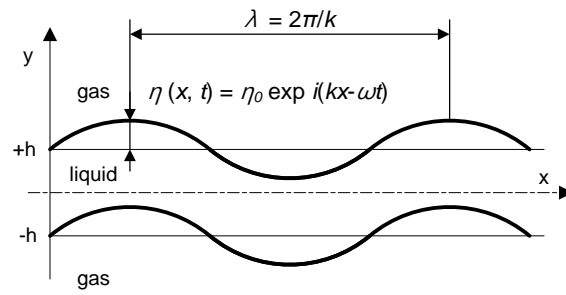


Fig. 3.7 Image analysis of cryogenic swirl flow for  
 (a) sinuous wave imposed on plane liquid sheet, (b) flow boundary detection and  
 (c) sine curve fitting of flow surface

The wave amplitude did not change significantly, independent of the ambient pressure, as shown in Fig. 3.8. As mentioned earlier, the amplitude of the wave was not maintained. In the flow image analysis, a roll-up vortex structure may have existed in the flow boundary and measurement error may have occurred. In contrast to the wave amplitude, the wavelength and propagation velocity both changed along the ambient pressure. As shown in Fig. 3.9, the wavelength shifted from short to long. This shift occurred under transient conditions in which the pressure of the injectant or the surroundings was close to the critical pressure. The wave propagation velocity decreased with an increase in the ambient pressure, as shown in Fig. 3.10. It is clear that the characteristics of the liquid swirl flow changed with the ambient pressure [Kim et al., 2007]. Increasing the ambient pressure prevents the penetration of the injected flow and causes a loss of the kinetic energy of the flow, after which the flow momentum decreases. In the transient region, however, the propagation velocity drastically increased.

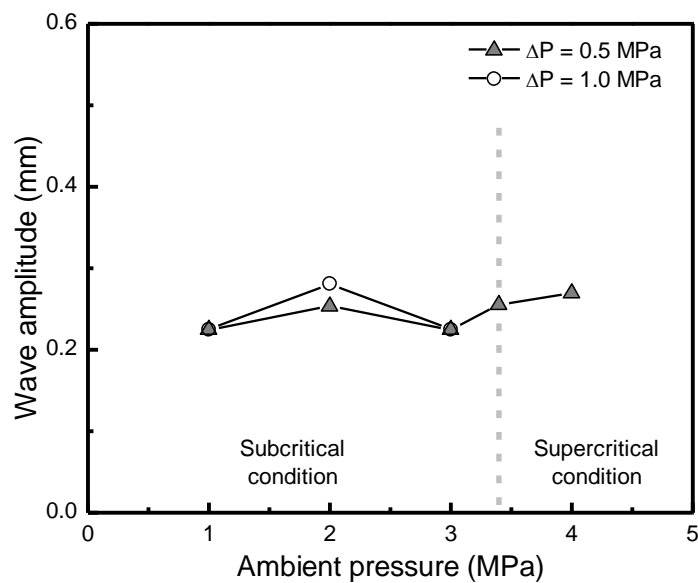


Fig. 3.8 Wave amplitude on surface of cryogenic swirl flow

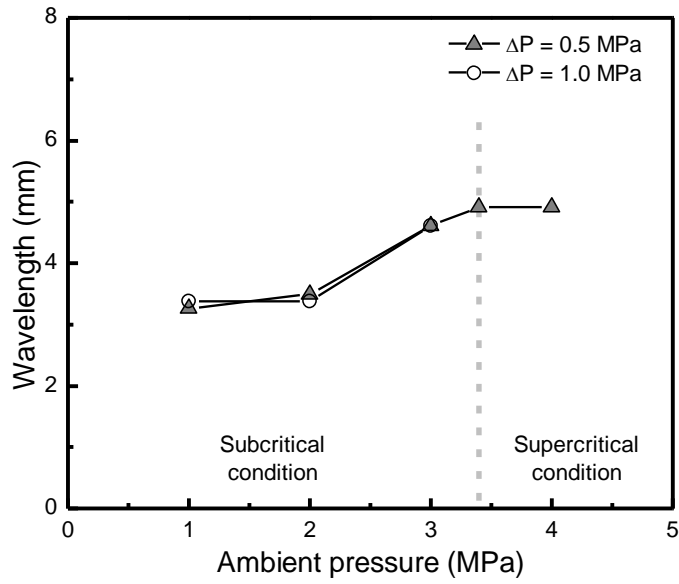


Fig. 3.9 Wavelength on surface of cryogenic swirl flow

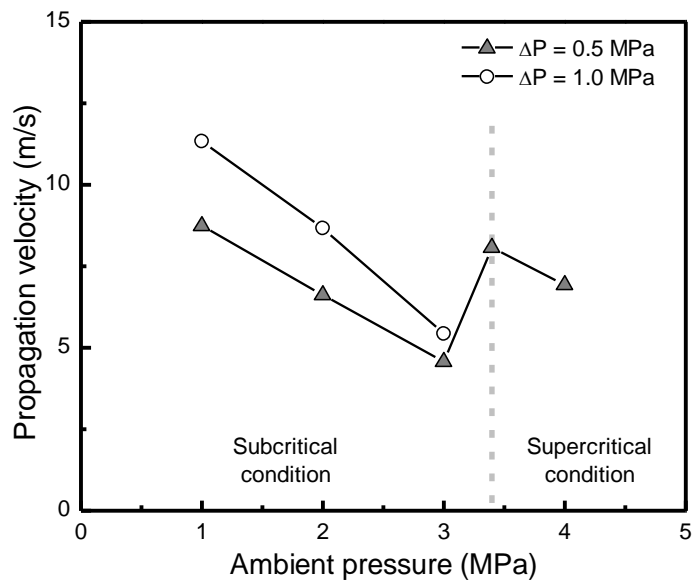


Fig. 3.10 Propagation velocity of surface wave in axial direction

Under supercritical conditions, the wavelength and propagation velocity of the flow surface sharply increased. These phenomena can be explained via the characteristics of a supercritical fluid. Due to the near-zero surface tension, the structure of the flow surface can be scattered easily. Here, only one roll-up vortex, rather than a sinuous wave, was found on the flow surface, as shown in Fig. 3.5(b). The value of the measured wavelength then reaches the measurable range, at around 5 mm. The increased velocity was caused by measurement error at  $P_c = 3$  MPa. Under this condition, the pressure of the injectant reaches the critical pressure, but the surroundings remain at a subcritical pressure. This pressure difference would cause disordered flow behavior and disrupt the reliable measurement of the wave characteristics. In this transient region, both a propagating wave and a rolled-up vortex structure exist at the same position, thereby becoming superimposed. At the very least, the superposition of the surface structures causes an underestimation of the velocity.

### 3.3.3 Instability analysis of a cryogenic swirl flow surface

An instability analysis of a cryogenic swirl flow was conducted via instability frequency measurements. The transmission rate of a laser line beam passing through the flow area was used to measure changes in the flow. The transmission rate is  $I/I_0$ , where  $I_0$  is the original laser beam intensity and  $I$  is the intensity of the beam which passes through the flow. When the liquid flow area increases, the laser beam is attenuated and the transmission rate is decreased. Therefore, when flow instability generates oscillation of the flow interface and finally the flow area, the transmission rate also oscillates and the instability frequency can be obtained by a spectral analysis.

If a certain frequency is found via spectral analysis of the transmission rate, it can be deduced that the structure on the flow surface is created periodically in the flow. Thus, the measured frequency can be defined as the instability frequency of the flow. The transmission rate was measured by a photodetector, and the data acquisition sampling rate of the detector was 100 kHz such that the frequency of the transmission rate oscillation

less than 50 kHz could be measured by a spectral analysis. As the PVC phenomenon generates an unstable flow structure, the frequency of the flow instability is regarded as the PVC instability frequency.

The power spectral density of the transmission rate was calculated via spectral analysis. The results for each condition are shown in Fig. 3.11. The effects of the ambient pressure and the injection differential pressure on the instability frequency are shown in Fig. 3.12. The unexpectedly large value of the spectral density shown in the low-frequency range ( $f < 100$  Hz) was considered as noise. With this data reduction, the peak frequency was located between 1 and 4 kHz, which corresponds to the PVC instability frequency [Syred, 2006]. The value of the measured frequency is comparable to that of the measured frequency of weak instability on a liquid swirl flow (2~3 kHz, at atmospheric pressure) [Museum et al., 2009], and the numerically calculated instability frequency of the liquid oxygen swirl flow under supercritical conditions (1.04 kHz, at 10 MPa) [Zong and Yang, 2008]. The instability frequency decreased with an increase in the ambient pressure and a decrease in the injection differential pressure. When the ambient pressure increases, the penetration of the flow into the surrounding area is obstructed and the axial flow velocity is decreased. A decrease in the injection differential pressure causes a decrease in the mass flow rate, finally having a similar effect on the flow. Consequently, the flow structure will pass the measurement point less frequently and the measured instability frequency will decrease.

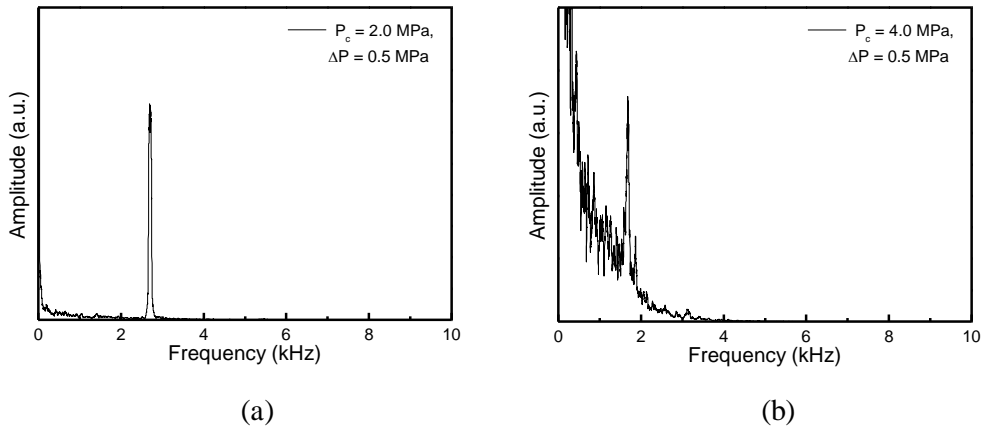


Fig. 3.11 Results from spectral analysis of transmission rate at  $\Delta P = 0.5$  MPa under various ambient pressure conditions: (a)  $P_c = 2$  MPa, (b)  $P_c = 4$  MPa

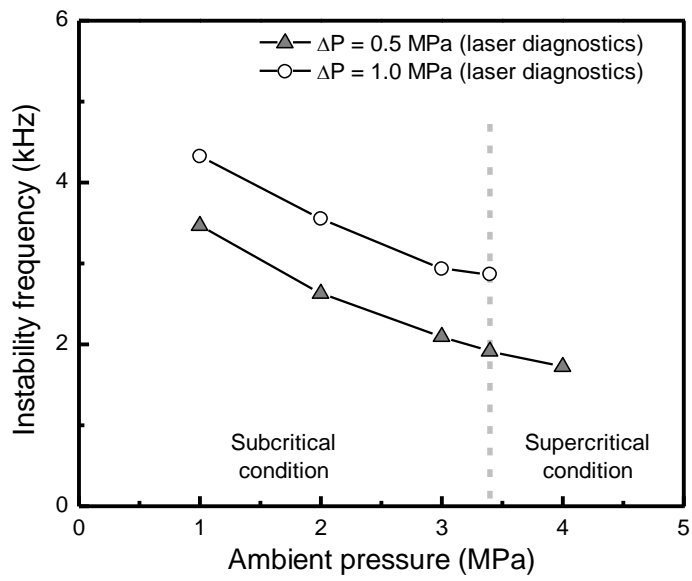


Fig. 3.12 Instability frequency of cryogenic swirl flow

## **Chapter 4**

# **DYNAMIC CHARACTERISTICS OF A CRYOGENIC SWIRL FLOW UNDER SUPERCRITICAL CONDITIONS**

### **4.1 Background and Objectives**

Many type of injectors are used in propulsion or power supply combustion engines for injection and mixing the fuel and oxidizer. In liquid propellant rocket engines, three types of injectors are generally used: impinging type, shear coaxial type and swirl coaxial type. Among these, swirl type injectors have several advantages in the distribution and mixing of injectants. Accordingly, this type of injector has been studied [Bazarov and Yang, 1998; Khavkin, 2004] and used in many of the rocket engines developed in Russia [Lefebvre, 1989].

Serious combustion instability can be induced in the combustion chamber of a liquid rocket engine because of its operational conditions of high pressure and temperature. Combustion instability is caused by the coupling of acoustic pressure oscillation and unsteady heat release [Culick and Yang, 1995]. This phenomenon drastically increases the amplitude of oscillation and ultimately leads to serious engine failure. Particularly in the most recently developed rocket engines, the high energy density condition inside the combustion chamber can provide a large amount of energy leading to instability. Therefore, the reduction of instability is extremely important in the development of liquid propellant rocket engines.

Various factors affect combustion instability: chamber geometry, instability from the propellant feed line, flow instability, etc. [Culick and Yang, 1995]. Among these, the most significant factor is the geometry of the combustion chamber, which determines the acoustic characteristics of combustion instability. Flow instability can affect the distribution and mixing of the injected propellant. This phenomenon can be related to the

disintegration and atomization characteristics of the liquid flow. Thus, numerous studies have been conducted on flow instability in swirl injectors [Cooper and Yule, 2001; Donjat et al., 2003; Im et al., 2009; Kenny et al., 2009; Kim et al., 2009; Landwehr et al., 2006; Marchione et al., 2007; Musemic et al., 2009]. In a simplex swirl injector flow, instability in the low-frequency ( $\sim 10^2$  Hz) and high-frequency ( $\sim 10^3$  Hz) regions were measured simultaneously [Landwehr et al., 2006; Musemic et al., 2009], and the similar instability frequencies caused by spray angle oscillation were observed [Marchione et al., 2007]. In addition, several studies have suggested that the internal flow instability of an injector causes instability in the external flow [Cooper and Yule, 2001; Donjat et al., 2003; Kenny et al., 2009]. In gas-liquid coaxial injector flow, the self-pulsation frequency has been related to the natural frequency of the liquid-only flow [Im et al., 2009].

The dynamic characteristics of cryogenic flow under supercritical conditions have also been investigated. These studies indicated that two kinds of instability in cryogenic swirl flow under supercritical conditions exist: a precessing vortex core (PVC) in the central toroidal recirculation zone (CTRZ) and Kelvin-Helmholtz instability caused by shear between the flow and its surroundings [Zong and Yang, 2008]. These instability characteristics are similar to those of liquid swirl flow injected into liquid surroundings [Gallaire et al., 2004; Liang and Maxworthy, 2005]. The response of the flow to external excitation was also experimentally [Teshome et al., 2012; Wegener et al., 2014] and numerically [Schmitt et al., 2012] investigated. These efforts revealed that the characteristics of flow instability can affect the response of the flow to external excitation.

For in-depth study of flow instability, mode decomposition methods have been recently applied to the flow field dataset. In particular, the Proper Orthogonal Decomposition (POD) method has been used to investigate the dynamics in various types of flows to obtain coherent flow structures and to determine their roles in flow behavior [Arienti and Soteriou, 2009; Berkooz et al., 1993; Eberhart et al., 2012; Markovich et al., 2014; Meyer et al., 2007; Semeraro et al., 2012; Teshome et al., 2012; Wegener et al., 2014; Zong and Yang, 2008]. Although most of these studies used velocity data from the flow field, some of them used flow images [Arienti and Soteriou, 2009; Eberhart et al.,

2012; Teshome et al., 2012; Wegener et al., 2014]. The POD method has already been adopted in investigations of the external behavior of swirl flow under subcritical conditions [Eberhart et al., 2012], jet flow under supercritical conditions [Teshome et al., 2012; Wegener et al., 2014], and the internal flow of the swirl injector under supercritical conditions [Zong and Yang, 2008]. Therefore, it is reasonable that this method be used in a study on swirl flow instability under supercritical conditions.

The main purpose of this study is experimental investigation of the instability characteristics of a cryogenic swirl flow. The ambient pressure was changed as the flow was injected into ambient gas under subcritical to supercritical conditions. The coherent structures of the flow were deduced by analysis of the flow image using the POD method. The spatial and temporal characteristics of the flow and its instability were determined to reveal the instability mechanism that dominated flow behavior.

## 4.2 Experimental Methods

### 4.2.1 Injector design

A simplex swirl type injector was mounted inside the chamber to create a cryogenic swirl flow. The injector was a closed-type swirl injector, creating a single hollow-cone-shaped flow. Its geometry was similar to the oxidizer part of the main injector used in an RD-0110 liquid propellant rocket engine [Rubinsky, 1995]. The detailed geometry of the injector is shown in Fig. 4.1 and Table 4.1. Because the inner diameter of the high-pressure chamber was much larger than that of the injector  $D_{o,i}$ , the confinement effect of the chamber wall to the flow was negligible. The temperature and the pressure of the fluid were measured in the vicinity of the tangential inlet of the injector to ensure that the flow was injected in the liquid state.

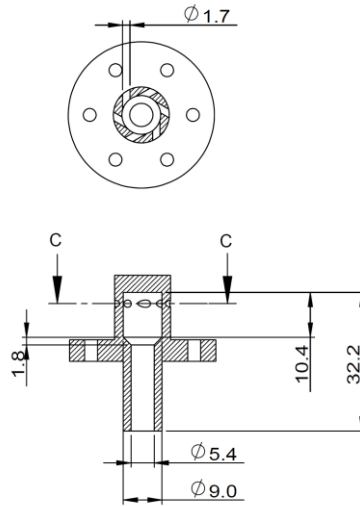


Fig. 4.1 Schematic of the simplex swirl injector (unit: mm)

Table 4.1 Injector geometry

Injector part	Geometry, mm
Swirl arm, $R$	3.5
Swirl chamber diameter (inner), $D_s$	9
Nozzle diameter (inner), $d_{o,i}$	5.4
Nozzle diameter (outer), $d_{o,o}$	9
Tangential inlet diameter, $d_p$	1.7
Number of tangential inlets, $n$	6
Injector geometrical characteristic parameter $K = 2Rd_{o,i}/nd_p^2$	2.2

#### 4.2.2 Experimental conditions

The detailed experimental conditions in this study are shown in Fig. 4.2 and Table 4.2. In Fig. 4.2, as noted in section 3.2.2, initial and final condition of the injectant for each experimental case are pointed and connected with a solid line in Pressure-Temperature diagram of nitrogen. The initial condition point represents the injectant condition at the injector manifold while the final condition point shows the condition of the surrounding nitrogen inside the high-pressure chamber. The injection differential pressure was maintained at 0.5 MPa, which is similar to the actual injection pressure of the oxidizer propellant in an RD-0110 engine [Rubinsky, 1995]. The ambient pressure of the injected flow was increased to 5 MPa, which exceeds the critical pressure of the working fluid. As a result, the liquid flow was injected into the surrounding environment under subcritical to supercritical pressure conditions. The ambient temperature of the flow was maintained around 280 K.

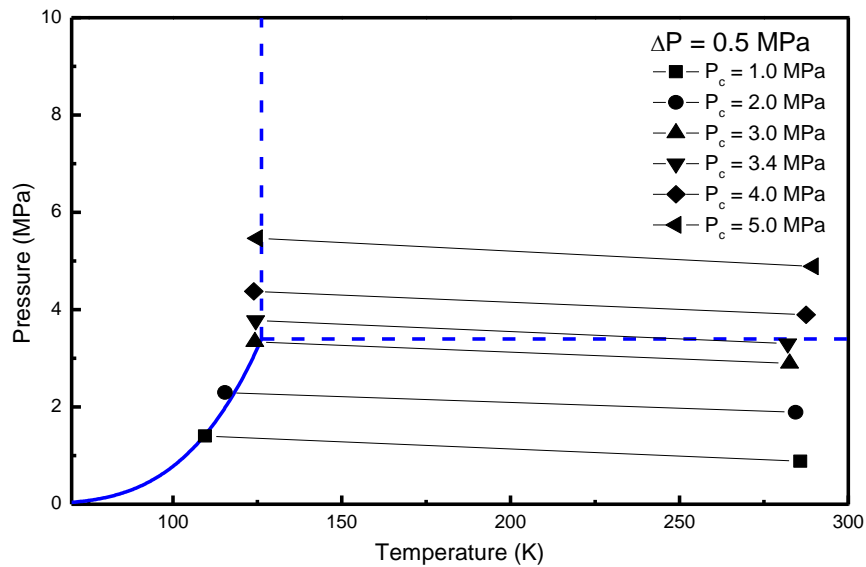


Fig. 4.2 Experimental conditions in Pressure-Temperature diagram of nitrogen

Table 4.2 Experimental conditions

Flow condition	Range
Injection differential pressure (MPa)	0.5
Ambient pressure (MPa)	1.0 – 5.0
Injector manifold temperature (K)	105 – 125
Ambient temperature (K)	280

### 4.2.3 Experimental techniques

The shape of the cryogenic flow was unstable because of its rapid phase change caused by the huge temperature difference between the flow and its surroundings. Therefore, a temporal measurement of the characteristics of the flow was required to study the flow dynamics. In this study, we chose the use of high-speed photography with backlight imaging technique. The whole imaging area was  $42.7$  (width)  $\times$   $21.3$  (height)  $\text{mm}^2$ . The length of each pixel was  $83.3 \mu\text{m}$ . The detailed explanation of this method is in section 2.2.1. The instability frequency of the flow was calculated from the POD analysis. For the validation of the result obtained from POD analysis, the flow frequency was measured with laser diagnostics which is shown in section 2.2.2.

### 4.2.4 Proper Orthogonal Decomposition

The POD method is an application of Principal Component Analysis, which has been used in stochastic analysis of datasets to analyze flow fields. The main purpose of the mode decomposition method is to determine modes from a set of flow field snapshots. These modes are spatially orthogonal to each other, and their coherent structures represent the main characteristics of the flow field [Arienti and Soteriou, 2009; Berkooz

et al., 1993; Meyer et al., 2007].

This section contains a brief explanation of the POD method. The detailed principle and process of POD analysis can be found in Appendix. First, each snapshot of the flow field can be reconstructed by linear summation of the modes. This can be represented as follows:

$$V = [v_1 \quad v_2 \quad \cdots \quad v_{N-1} \quad v_N] \quad (4.1)$$

$$v_n = \sum_{i=1}^N a_{i,n} \phi_i \quad (4.2)$$

In the above equations,  $V$  is a set of flow field snapshots  $v_n$ ,  $\phi_i$  is an  $i$ th spatial POD mode, and  $a_{i,n}$  is a time coefficient related to snapshot  $v_n$  and mode  $\phi_i$ .

Each mode has its own eigenvalue, which can be deduced from the POD mode extraction process.

$$Z = V^*V \quad (4.3)$$

$$Z\phi_i = \lambda_i\phi_i \quad (4.4)$$

$Z$  is the covariance matrix of  $V$ . Symbol  $*$  means conjugate transpose of matrix.  $\lambda_i$  is an eigenvalue of the mode  $\phi_i$  and can be treated as the relative energy of the mode. It is well known that a mode with large eigenvalue is strongly related to  $V$  and contains important information about the flow characteristics. If  $v_n$  contains velocity data in the flow field, then the mode eigenvalue is proportional to the square of the velocity components in the mode. In this case, if the density is constant for the entire flow field, the mode eigenvalue can be directly related to the kinetic energy of the flow.

Although the POD method deduces spatially orthogonal modes, additional analysis is required to determine instability characteristics. Spectral analysis of the time coefficient  $a_i$  can be conducted to determine the instability frequency of the mode.

To apply the POD method to flow image analysis, Matlab™ was used in the image processing. Although velocity field information is mainly used in POD [Berkooz et al., 1993; Meyer et al., 2007; Semeraro et al., 2012], flow image information also can be adopted in the analysis to determine the instability characteristics of the flow [Arienti and Soteriou, 2009; Eberhart et al., 2012]. Moreover, the flow image can be related the distribution of the flow, and the oscillation of the flow distribution is highly dependent on flow instability. Consequently, it is possible to determine the important characteristics of flow instability with POD analysis of the flow image set.

In this study, 4,000 images were used for the POD analysis of each experimental condition. The analysis area for the flow images was 27 (width)  $\times$  10.8 (height) mm<sup>2</sup>. The characteristics of the flow for different positions were investigated by selecting an analysis area with  $y/D_{o,i} = 0 \sim 2$  (upstream region) and  $y/D_{o,i} = 1 \sim 3$  (downstream region) where  $y$  is the axis along the flow propagation starting from the injector post. The analysis area is shown in Fig. 4.3.

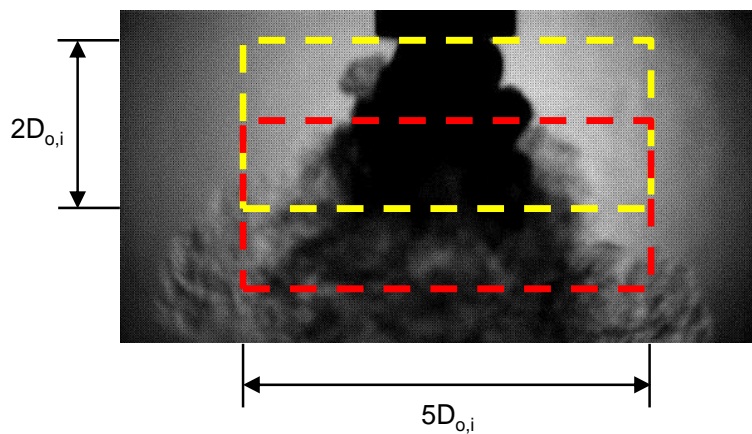


Fig. 4.3 Analysis area of the flow image for the upstream (yellow line) and downstream (red line) regions

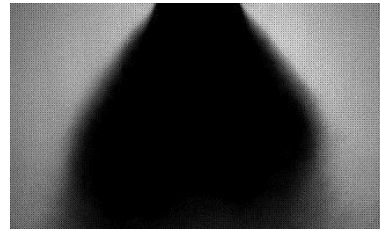
## **4.3 Results and Discussion**

### **4.3.1 Static characteristics of a cryogenic swirl flow**

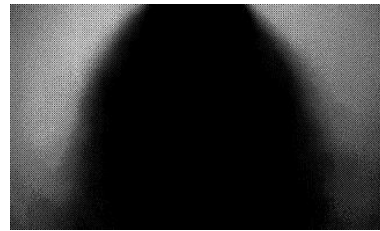
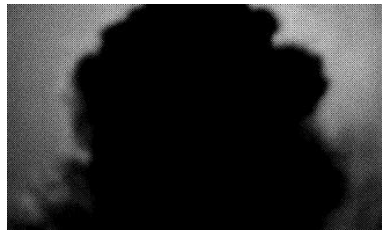
As previously mentioned, a cryogenic flow has significant instability [Cho et al., 2014; Zong and Yang, 2008]. Because of this, the flow was visualized using high-speed photography. The instantaneous and averaged images of the flow for each experimental condition are shown in Fig. 4.4.

In the instantaneous flow images, serious instability was observed on the flow surface. Many structures with various scales were superposed in the vicinity of the injector post region, which created a rough surface shape. The vortex ring structures were generated by Kelvin-Helmholtz instability at the downstream region where the phase change and the disintegration of the injectant occurred. These phenomena were most significant under subcritical conditions, as shown in Fig. 4.4(d).

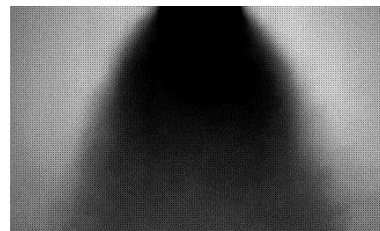
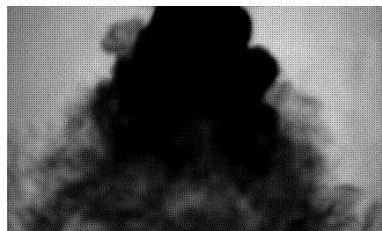
Many factors lead to instability of the flow surface, such as flow instability, relatively low surface tension of the cryogenic fluid, non-periodic surface change caused by phase change of the injectant, or interaction of the flow and its surroundings. If the most influencing factor among these is the natural instability of the flow, it can be supposed that various instability mechanisms can affect the cryogenic swirl flow. However, to prove this supposition, the coherent structures and frequencies that represent certain instability phenomena should be deduced from an analysis of the flow images.



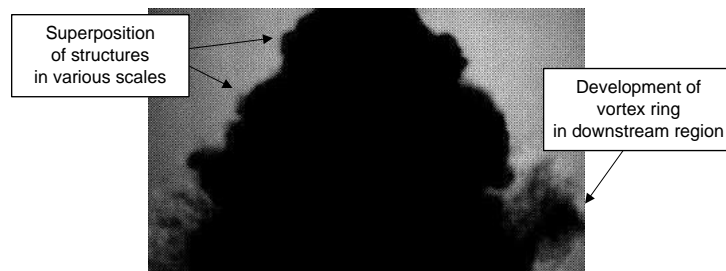
(a)  $P_c = 2.0$  MPa



(b)  $P_c = 3.4$  MPa



(b)  $P_c = 5.0$  MPa



(d)

Fig. 4.4 Representative images of the cryogenic swirl flow; instantaneous (left column) and averaged (right column) images for (a) subcritical, (b) critical, (c) supercritical ambient conditions, and (d) structures on the flow surface

Next, the spray angles were measured from the flow images to investigate the quantitative characteristics of the flow shape. Spray angle is a useful parameter to indicate the distribution of the injected flow. The results are shown in Fig. 4.5.

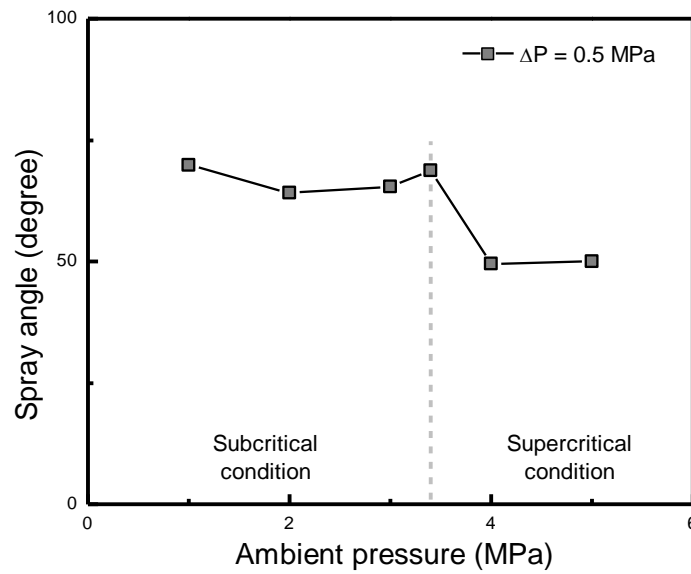


Fig. 4.5 Spray angle of the cryogenic swirl flow

The spray angle was abruptly decreased when the ambient pressure was changed from subcritical to supercritical pressure. The relationship between the angle and flow condition were then considered to account for this drastic decrease. The spray angle can be represented as follows.

$$\frac{\alpha}{2} = \tan^{-1} \frac{w}{u} \quad (4.5)$$

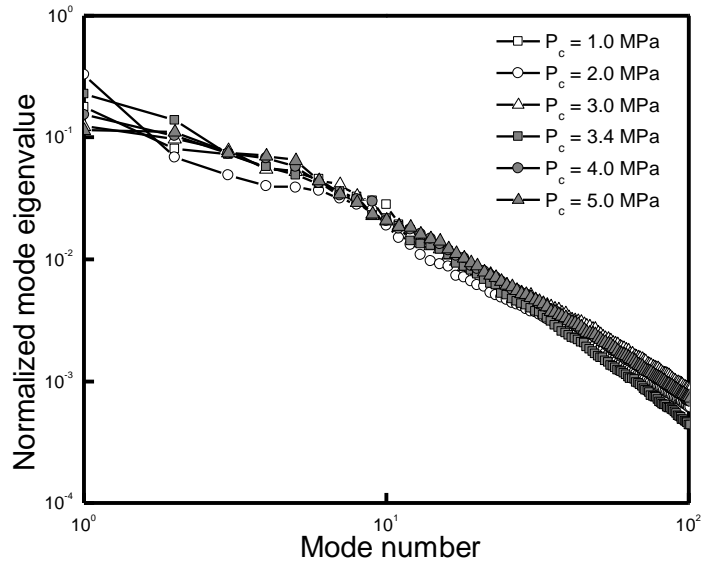
In this equation,  $\alpha$  is the spray angle,  $w$  is the tangential velocity, and  $u$  is the axial velocity of the flow. This equation shows that the spray angle is a parameter determined by the velocity of the flow. From equation (4.5) and Fig. 4.5, it can be deduced that the swirl strength of the flow was significantly decreased under supercritical conditions. Although an explanation for this decrease could not be determined in this study, it can be suggested that the injectant's phase change process, called the transcritical process, decreases the tangential velocity inside the injector more than the axial velocity component, and finally causes a decrease in the spray angle [Cho et al., 2014; Zong and Yang, 2008].

#### 4.3.2 POD analysis of flow image

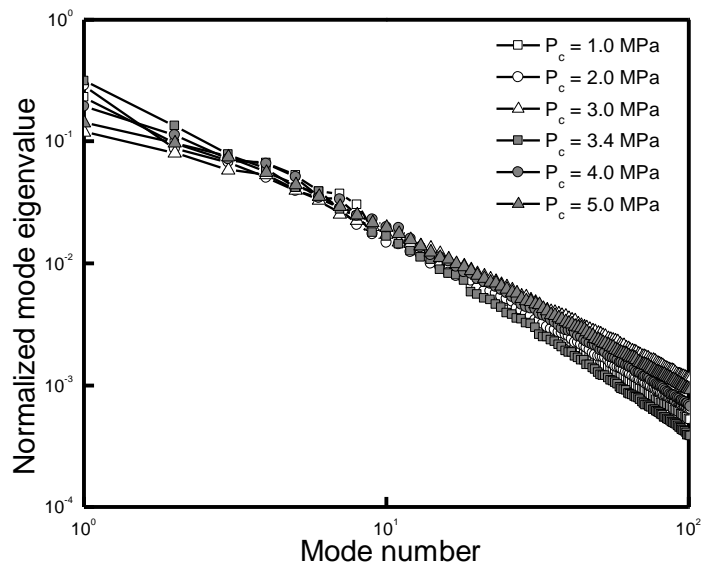
POD analysis was conducted on the set of flow images. First, the normalized mode eigenvalue distributions for each experimental condition were investigated. The following results are demonstrated in Fig. 4.6. It was observed that most of the total mode energies were distributed in the initial 10 ~ 20 modes. Therefore, the initial 10 modes for each condition were investigated in the analysis of the results obtained by POD analysis.

The initial 10 POD modes in upstream and downstream region for subcritical ( $P_c = 2.0$  MPa), critical ( $P_c = 3.4$  MPa), and supercritical ( $P_c = 5.0$  MPa) conditions are shown in Fig 4.7 to 4.12. Because there is no external excitation to the flow, the portion of the flow instability structure to the whole flow shape is small. Therefore, it can be supposed that the eigenvalue of the POD mode related to the instability would be smaller than the mode with mean flow shape.

Although mean flow image was extracted in the POD analysis analysis, the first POD mode under subcritical conditions is similar to the averaged image. Its normalized eigenvalue is between 0.2 to 0.3. In contrast, the first mode under supercritical conditions shows the instability structure on the flow surface and its eigenvalue is around 0.1. It implies that flow instability considerably affects to the behavior of the injectant under supercritical condition.



(a)



(b)

Fig. 4.6 POD mode eigenvalue distribution for the experimental conditions;  
 (a) upstream modes, and (b) downstream modes

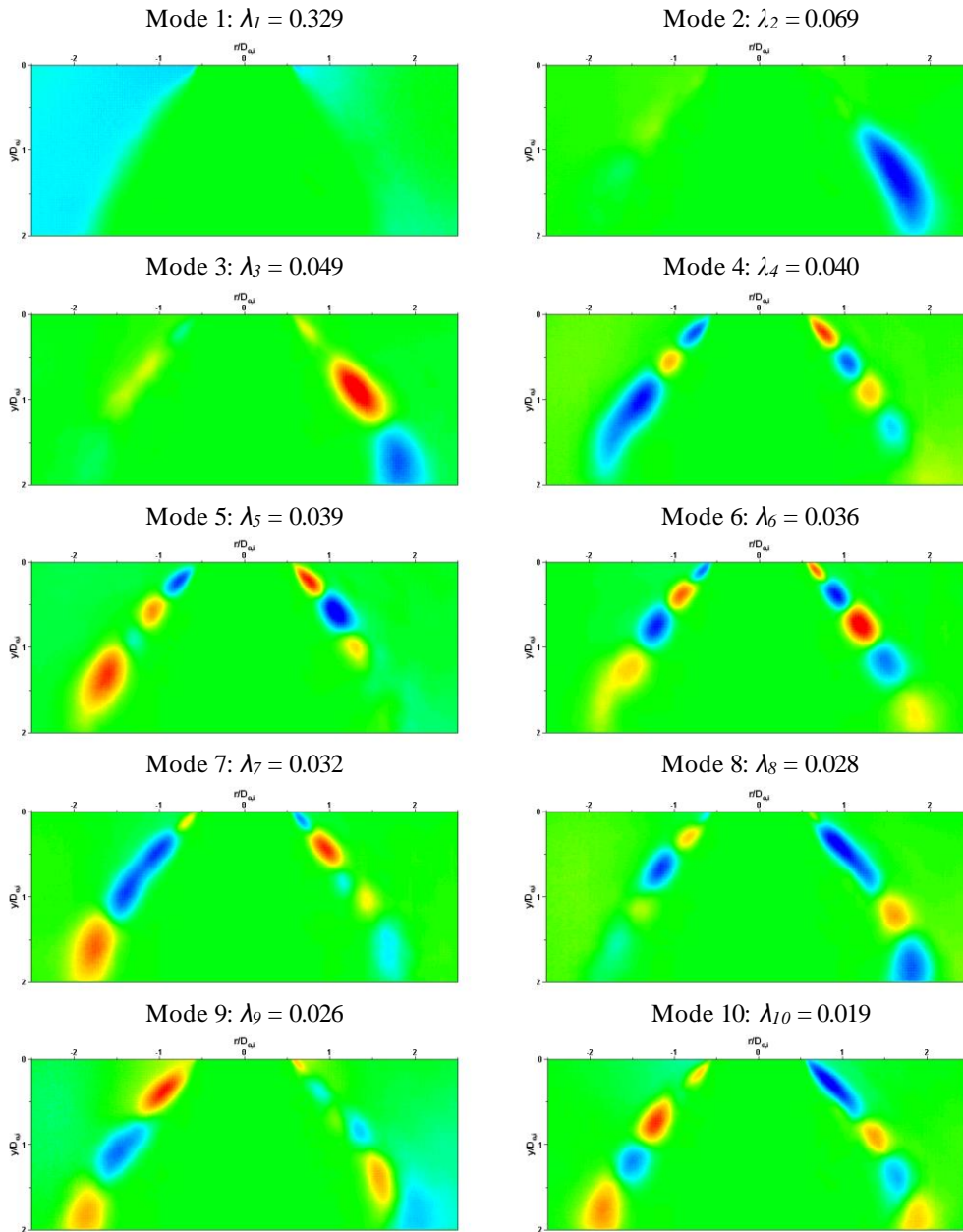


Fig. 4.7 Initial 10 POD modes for subcritical condition ( $P_c = 2.0$  MPa);  
upstream region

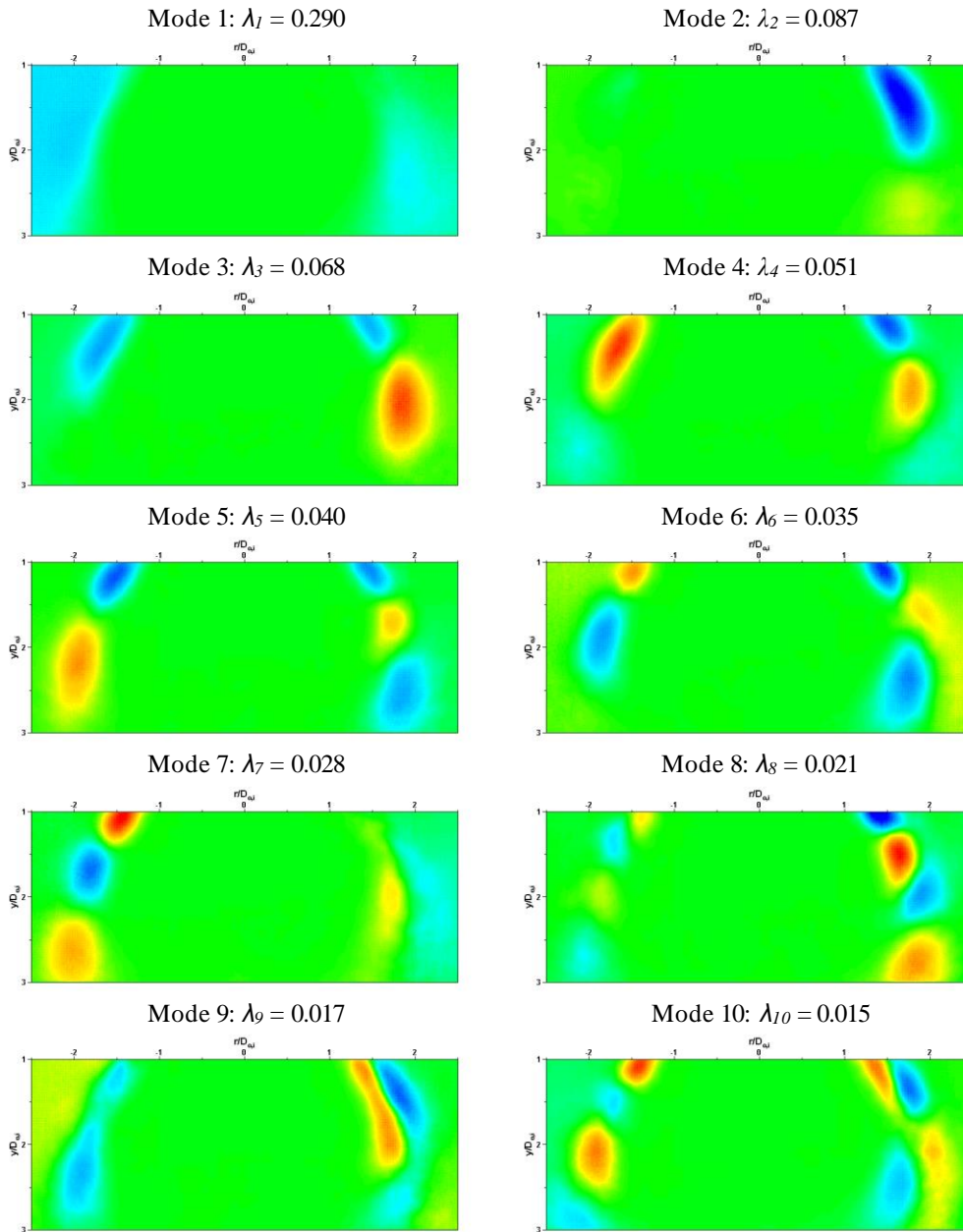


Fig. 4.8 Initial 10 POD modes for subcritical condition ( $P_c = 2.0$  MPa);  
downstream region

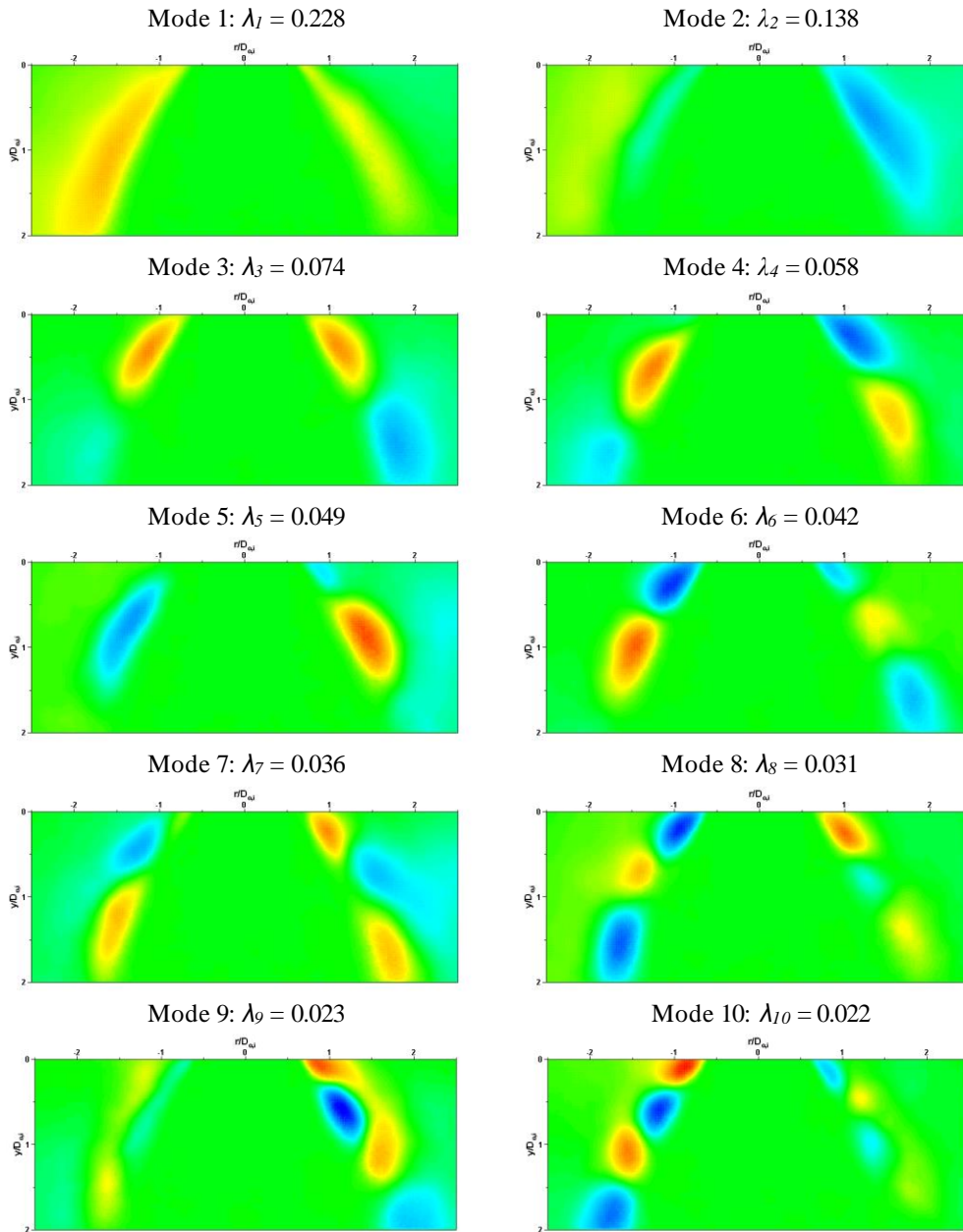


Fig. 4.9 Initial 10 POD modes for critical condition ( $P_c = 3.4$  MPa);  
upstream region

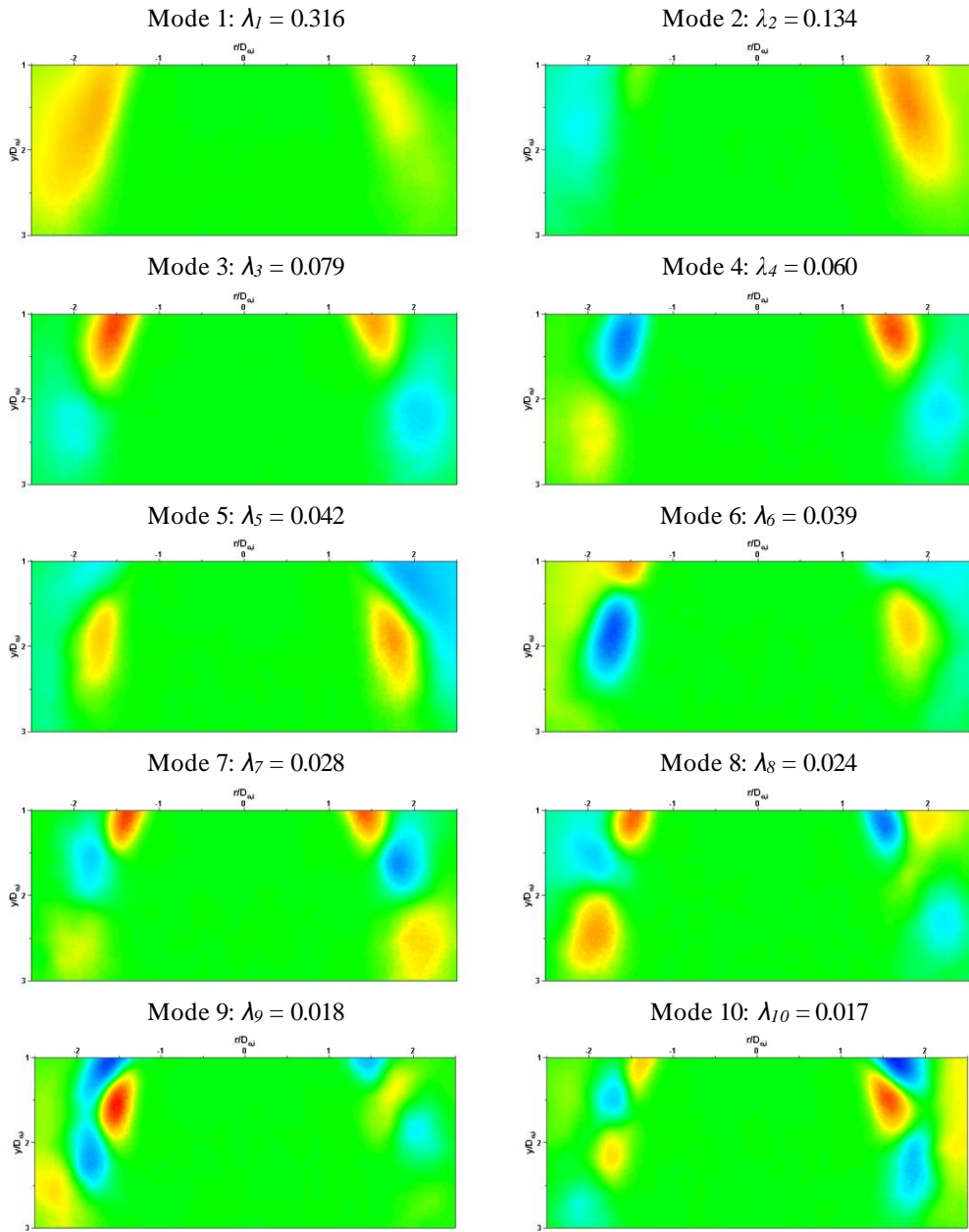


Fig. 4.10 Initial 10 POD modes for critical condition ( $P_c = 3.4$  MPa);  
downstream region

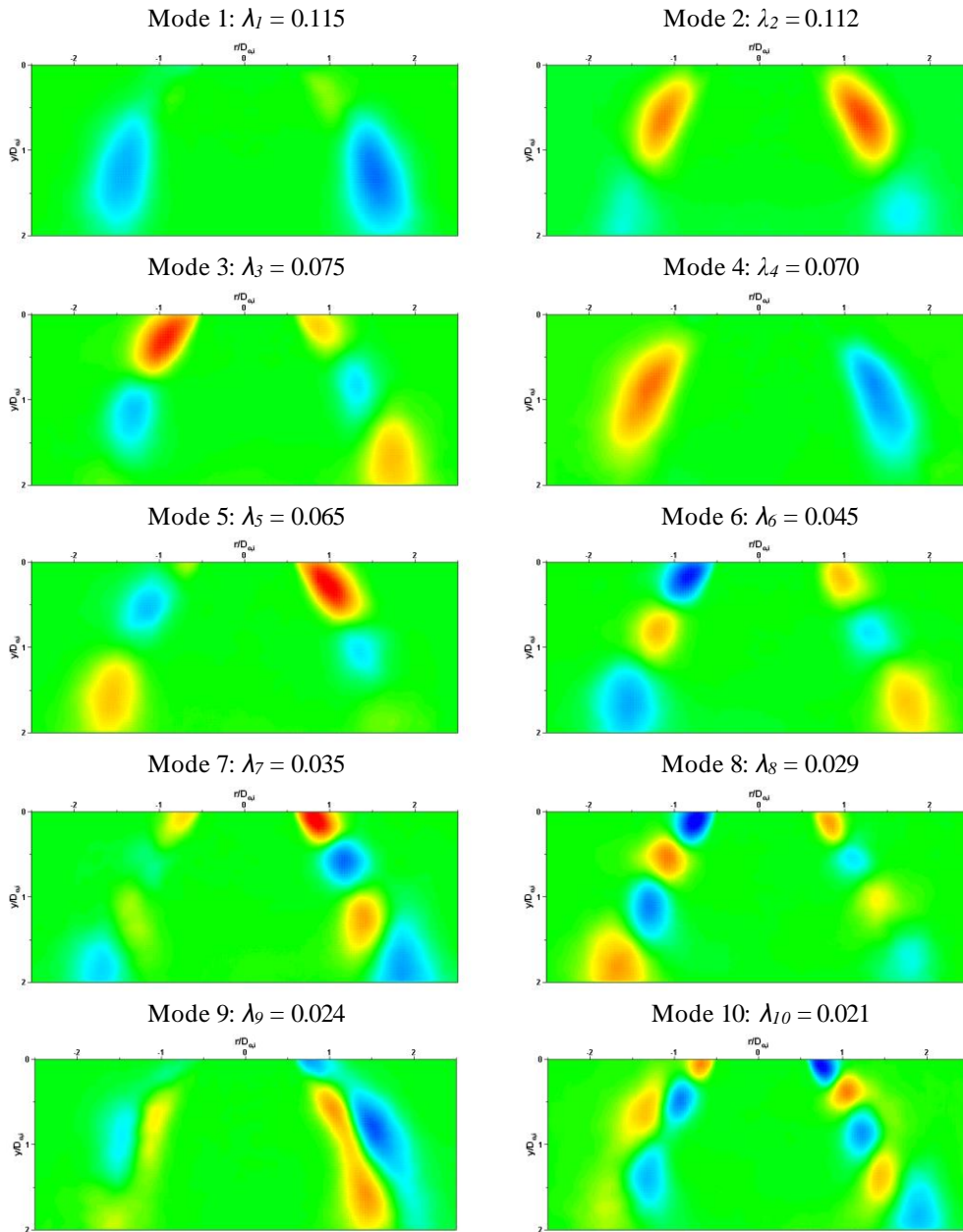


Fig. 4.11 Initial 10 POD modes for supercritical condition ( $P_c = 5.0$  MPa);  
upstream region

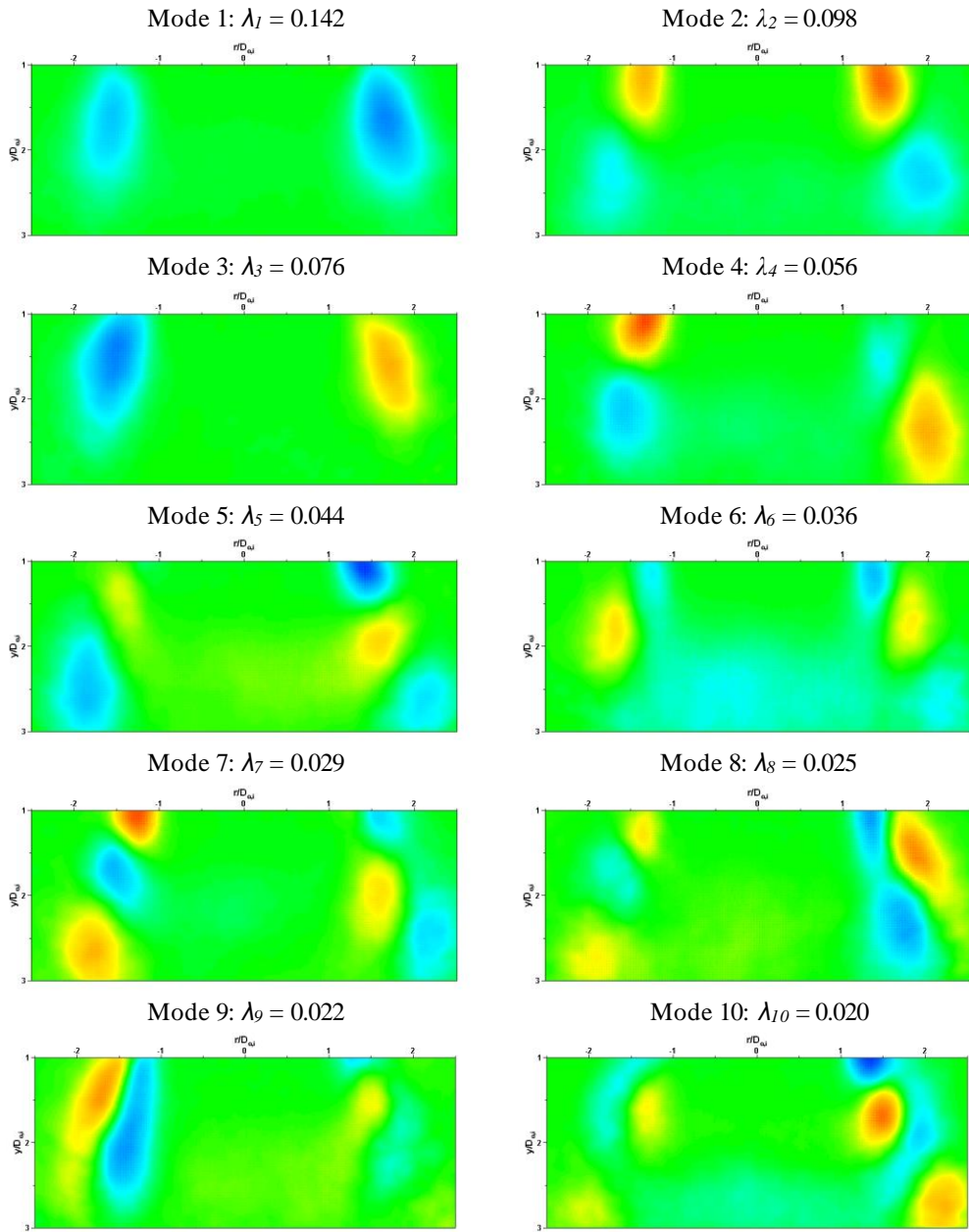


Fig. 4.12 Initial 10 POD modes for supercritical condition ( $P_c = 5.0$  MPa);  
downstream region

From the initial 10 POD modes, representative spatial modes were collected for each condition. The modes for the upstream region are shown in Fig. 4.13; those for the downstream region can be found in Fig. 4.14. The representative modes had their own coherent structures. These structures were aligned along the flow surface line, and the spatial characteristics of the flow were observable.

Two kinds of modes were found using POD analysis: a symmetric/tilted-ring shaped mode and an anti-symmetric shaped mode. The symmetric modes were generally found in the initial 1 to 5 modes. The coherent structures in this type of mode were located in the broad range of the analysis area, mainly in the downstream region. The scale of the structure size and the distance between each structure was large. In contrast, anti-symmetric modes could be found in modes 6 to 10, which have low eigenvalue compared to the symmetric modes. The coherent structures were located in the vicinity of the injector post, and the scale of their size and distance was relatively small. The categorization of the modes with these criteria was used in previous work [Markovich et al., 2014] for the analysis of swirl flow behavior. It was determined in this previous study that the coherent structures in each mode were generated by their own instability mechanisms.

First, the symmetric mode is generated by Kelvin-Helmholtz instability. The coherent structures arranged with symmetric shapes represent the vortex ring structures created by velocity shear between the flow and its surroundings. When the flow has a strong swirl momentum, the shape of the structure is shown as a tilted-ring rather than a symmetric structure. In cryogenic swirl flow, coherent structures in the symmetric mode were located far from the injector post. It can be supposed that this phenomena might be caused by the phase of the injectant which results in a huge influence of Kelvin-Helmholtz instability on flow behavior. As shown in Fig. 4.4, the phase change of the injectant in the downstream region induces a decrease of density and surface tension of the fluid, and finally, the flow easily loses its initial shape by external force.

In contrast, in the anti-symmetric mode, coherent structures are created by helical instability, which is related to the swirl of the flow. It is widely accepted that this

instability is commonly generated by the PVC in the central toroidal recirculation zone [Gallaire et al., 2004; Liang and Maxworthy, 2005; Syred, 2006; Wang et al., 2005]. PVC instability mainly occurs when the state of the injectant and its surroundings is similar when a gas flow is injected into the surrounding gas [Syred, 2006; Wang et al., 2005] or when a liquid flow is injected into the surrounding liquid [Gallaire et al., 2004; Liang and Maxworthy, 2005]. However, the instability mechanism seems different under conventional operating conditions for liquid swirl injectors where a liquid flow is injected into a surrounding gas under subcritical conditions. In this case, helical instability is generated by the instability of the liquid film inside the injector, and this instability affects the disintegration and atomization process of the flow [Cooper and Yule, 2001; Donjat et al., 2003; Kenny et al., 2009; Kim et al., 2009]. It has been suggested that the main reason for this instability is the precession of the air core inside the injector caused by the flow from the tangential inlet [Donjat et al., 2003]. These previous studies successfully explained the phenomena that the anti-symmetric structures were located in the vicinity of the injector post under subcritical conditions where the injectant remains in the liquid phase.

However, under supercritical conditions, the anti-symmetric structures were located in the broad range of the analysis area, as shown in Figs. 4.13 and 4.14. Under this condition, the swirl strength of the flow would be decreased inside the injector and cause the subsequent precession of the air core to diminish. As a result, the instability inside the injector would not be the main factor that dominates the instability of the external swirl flow. In this situation, the PVC instability mechanism would determine the characteristics of the helical instability. Because the properties of the injectant and the surroundings are similar under supercritical conditions, the PVC can dominate the flow behavior. A previous study conducted using numerical analysis [Zong and Yang, 2008] also insisted that the instability of the external swirl flow under supercritical conditions was dominated by PVC instability. Therefore, it can be inferred that when the condition of the surroundings is changed from subcritical to supercritical, the mechanism generating helical instability will also be changed.

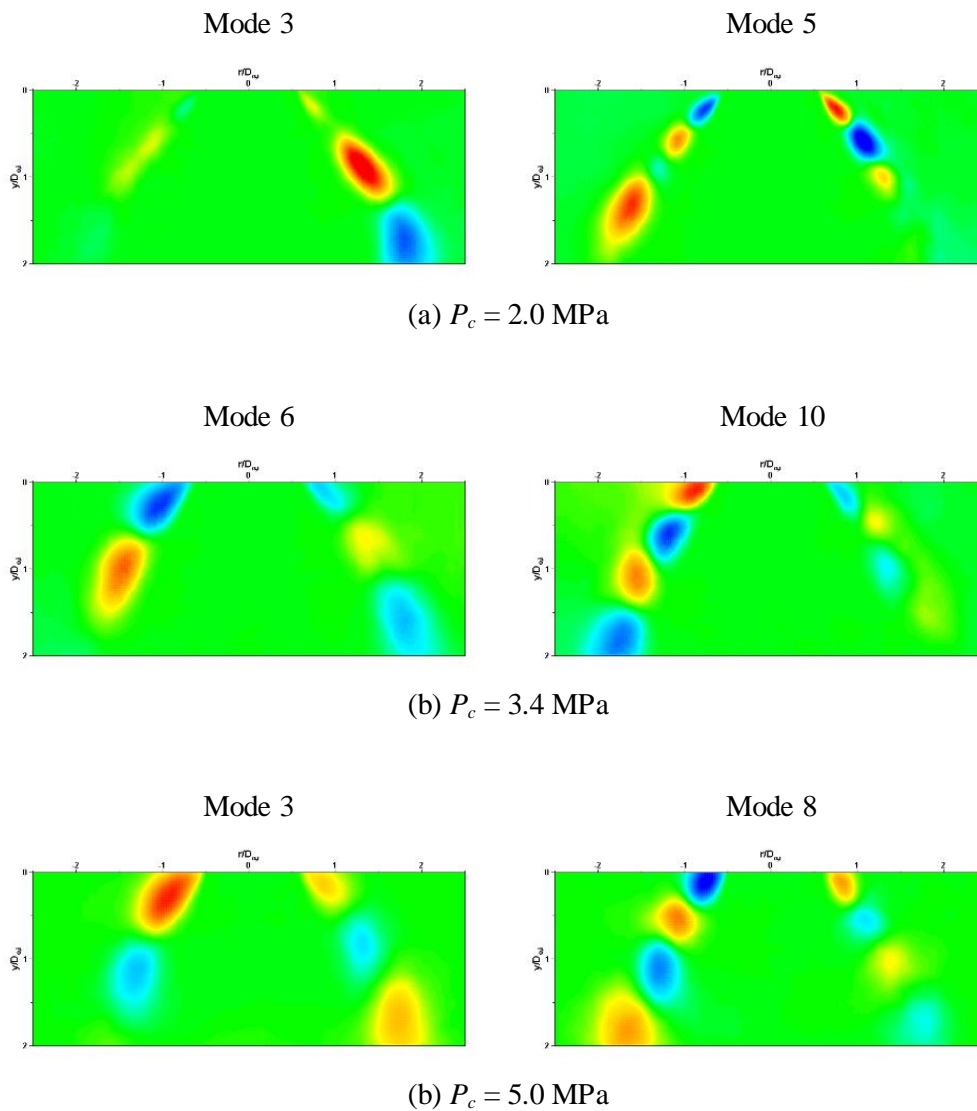


Fig. 4.13 Representative POD modes of the upstream cryogenic swirl flow; symmetric/tilted-ring structure (left column) and anti-symmetric structure (right column) modes for (a) subcritical, (b) critical, and (c) supercritical ambient conditions



### 4.3.3 Analysis of POD mode

Temporal and spatial analyses of the POD modes were conducted to identify the quantitative characteristics of the instabilities for each experimental condition. First, an analysis of a conjugate pair was attempted. A conjugate pair is determined from the cross-power spectrum analysis conducted on the time coefficients of two arbitrary modes. If the maximum amplitude of the spectrum is found at a phase with  $\pm 90^\circ$ , these two modes are thought to be a conjugate pair. The existence of a conjugate pair denotes that the coherent structures in the modes travel in the downstream direction [Arienti and Soteriou, 2009; Wegener et al., 2014]. In the present study, pairs existed in the anti-symmetric mode under most experimental conditions, while they were rarely found in the symmetric mode. This result implies that the vortex ring structure generated by Kelvin-Helmholtz instability does not travel along the flow direction with constant velocity. Because the vortex ring rotates counter to the flow direction, a part of the structure does not move downward. Therefore, it is obvious that a conjugate cannot be found in a set of symmetric modes. On the other hand, the axial velocity component of the flow is maintained in helical instability. With this velocity component, the coherent structures in the anti-symmetric mode propagate along the flow direction and consequently, a conjugate pair can be detected. An example of a conjugate pair in the anti-symmetric mode is shown in Fig. 4.15.

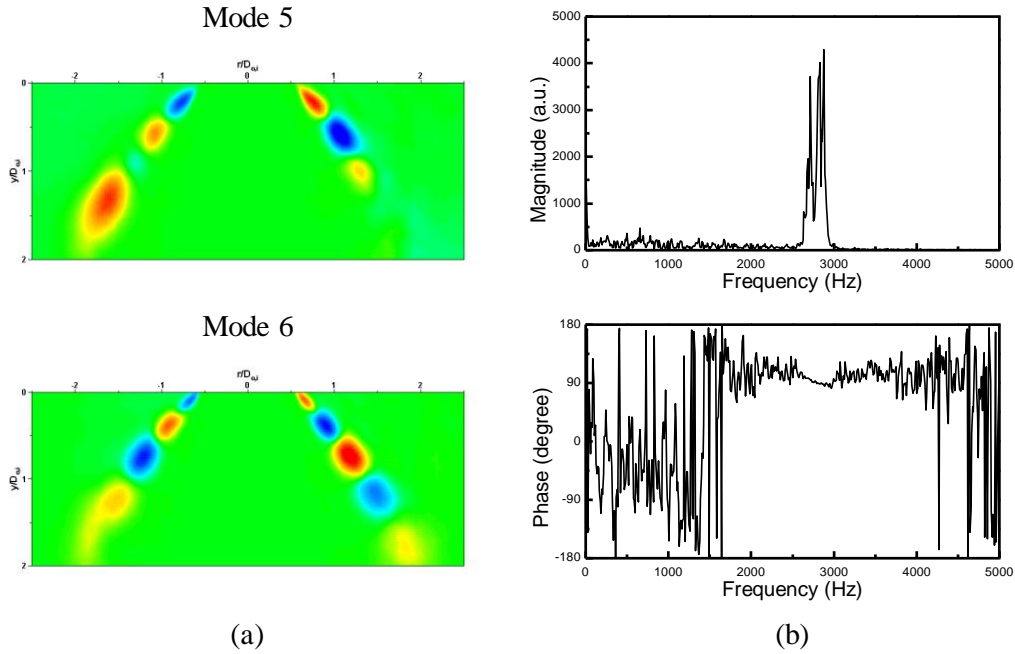


Fig. 4.15 Conjugate pair analysis of POD modes at  $P_c = 2.0$  MPa (upstream region): (a) conjugate mode images, and (b) cross-power spectral density for conjugate modes

For temporal analysis of the POD mode, time coefficients for representative POD modes were selected and spectral analysis was conducted. The peak instability frequency was deduced from the spectrum for each experimental condition. The frequencies obtained from the POD analysis and that from laser diagnostics method are compared in Fig. 4.16. In POD analysis, for each experimental conditions, significant peak frequency was observed only for the anti-symmetric mode obtained in the upstream region. In previous work, it was pointed out that the dissipation of the highly turbulent flow in this region would spread the instability energy to instabilities with other frequencies [Semeraro et al., 2012]. Thus, it is reasonable that the instability frequency was found only in the upstream region.

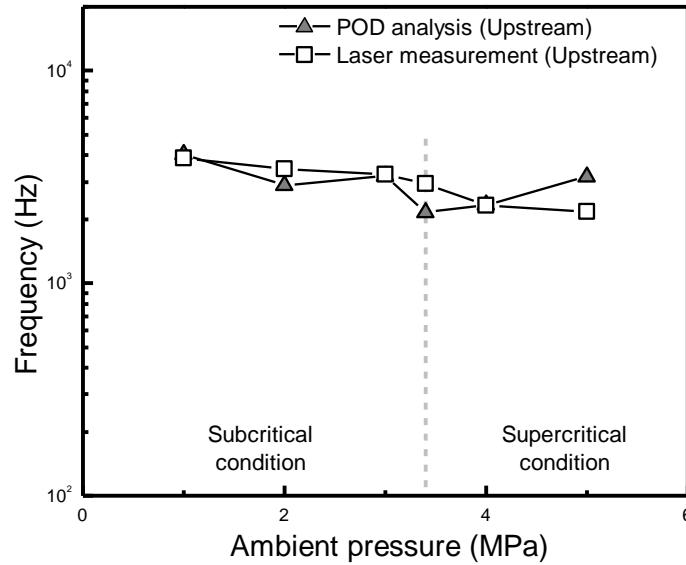


Fig. 4.16 Instability frequency of POD modes in the cryogenic swirl flow

The frequencies of the anti-symmetric modes were higher than 2 kHz, within the frequency range of combustion instability. The change of frequency along with the ambient pressure was different for subcritical and supercritical conditions. The instability frequency of the anti-symmetric mode was decreased along the ambient pressure under subcritical conditions, while it was increased under supercritical conditions.

It is clear that the instability propagated from the inside of the injector is weakened and its frequency is decreased when the ambient pressure increases. However, in the present study, the frequency of the instability generated by the PVC was increased along with the ambient pressure under supercritical conditions. Although further study is required for the explanation of this phenomenon, the results showing that the change of instability frequency is different for each condition support the existence of different instability mechanisms for subcritical and supercritical conditions.

Meanwhile, instability frequencies measured from laser diagnostics were similar to

the frequencies obtained from POD analysis. As shown in Fig. 4.7 to 4.12, anti-symmetric structures of the flow appear in the vicinity of the injector post. Therefore, the result of frequency measurement implies that the helical instability mainly determines the behavior of the flow instability in the region where the injectant remains in liquid state. However, when  $P_c = 5.0$  MPa, frequency measured from laser diagnostics was 2.1 kHz while that of POD analysis was 3.1kHz. The reason of this difference is not clear. Thus, additional study should be conducted.

The wavelength of the coherent structure was measured to discover the spatial characteristics of the spatial modes in the flow. In each mode, the wavelength was measured from the distances between the structures. The obtained results are shown in Fig. 4.17. The wavelength in the anti-symmetric mode was relatively smaller than that of the symmetric structure under the subcritical condition. This denotes that different instability mechanisms are applied to each mode. Meanwhile, the wavelength of the coherent structure increased in the downstream region, which indicates dissipation of the flow.

The wavelengths for each mode had similar values in the downstream regions or under supercritical conditions. Moreover, in such cases, as shown in Figs. 4.7 to 4.12, it was difficult to distinguish the symmetric and anti-symmetric structures. The most significant similar characteristic for both cases is that most of the injectants were changed from liquid to gas or to supercritical fluid, which behaves like dense gas. This result implies that when the phase of the injectant is changed to a gas-like state, its instability characteristics become similar for each experimental condition.

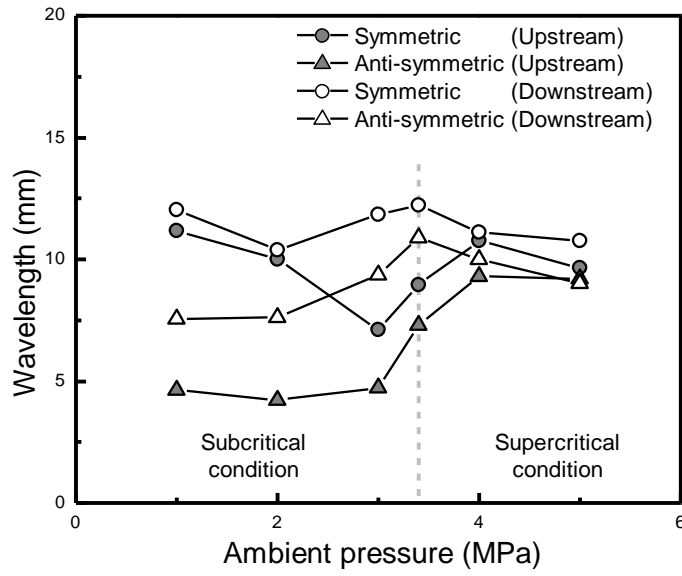


Fig. 4.17 Wavelength of POD modes in the cryogenic swirl flow

## CHAPTER 5

### CONCLUSION AND FUTURE WORK

#### 5.1 Conclusion

The characteristics of the cryogenic swirl flows under subcritical to supercritical conditions were investigated experimentally. High-speed photography and frequency measurement method using laser diagnostics were used to analyze the flow characteristics. The flow characteristics were observed in qualitative and quantitative manner, and spatial and temporal analysis was conducted. Spray angle and other static characteristics were investigated, and surface wave analysis and the POD analysis were used to obtain the surface instability and the dynamic characteristics of the flow. Although the datasets are limited because of the difficulty in flow measurement, the following results were obtained.

1. The characteristics of the cryogenic swirl flow were identified. Due to the fast phase change, and low density, and surface tension of the injectant, unstable structures on the flow surface were generated. The flow instability was caused by a PVC, and the scale of the instability was significantly larger than that of the water flow.
2. The effect of the ambient pressure to the cryogenic swirl flow were investigated. Due to the differences in each condition, the flow characteristics were changed during the transition from subcritical to supercritical pressure, occurring before and then after the phase change as well. These differences also affected the instability on the flow surface, creating a helical wave initially, which then developed into a roll-up vortex structure.
3. The instability frequency of the flow was measured. As the flow changes periodically, the instability frequency can be calculated via spectral analysis of the transmission rate of a laser beam passing through the flow. The frequency decreased when the ambient pressure increased. This result is explained by the decrease in the

propagation velocity of the surface structure.

4. From the POD analysis, the coexistence of two types of modes was ascertained: a symmetric/tilted-ring shaped mode and an anti-symmetric shaped mode. The symmetric structures in the mode represented the vortex ring generated by Kelvin-Helmholtz instability. This mainly occurred in the downstream region of the flow and created large-scale structures.
5. The anti-symmetric mode was created by helical instability. This instability had high-order frequency. The mechanism generating the instability was different for subcritical and supercritical conditions. Under subcritical conditions, the high swirl strength of the flow inside the injector generated the instability and the resulting structure was located in the vicinity of the injector post where the injectant remained in a liquid state. Under supercritical conditions, the swirl strength was decreased and the instability was generated by PVC, which dominates the flow behavior when the states of the injectant and its surroundings are similar. The range of the instability frequencies and the related instability mechanisms is thought to be related to the instabilities that exist in liquid propellant rocket engines.
6. In the downstream region or under supercritical conditions, the spatial characteristics of the coherent structures become similar. This result implies that when the injected flow loses its energy by interaction with the surrounding environment, and when the phase of the injectant is changed and its properties become similar to the surrounding environment, the mixing of the flow and its surroundings would be enhanced and its own instability characteristics would be diminished. Especially under supercritical conditions, because the injectant's phase change process is significantly different from that under subcritical conditions, in-depth consideration of flow behavior is required to understand flow characteristics.

## 5.2 Recommendations for Future Work

This study mainly focused on the analysis of the flow image. Although the image can be related to the density distribution of the injectant, it shows the opacity of the flow. Therefore, the real property data of the flow cross section cannot be adopted. To solve this problem, Raman spectroscopy have been used in many research to investigate the characteristics of the single/coaxial liquid nitrogen jet flow [Chehroudi et al., 2002a; Oswald and Schik, 1999]. This method measures the density distribution of the flow without interrupting the flow. However, some problems can be occurred in use of this method to the cryogenic swirl flow. Because the intensity of Raman signal from the swirl flow would be much smaller than that of the jet flow, serious attenuation and distortion of signal could occur. Therefore, various techniques would be needed in correction of the signal.

Meanwhile, POD analysis was conducted to investigate the characteristics of time-resolved flow images. However, this method deduces spiatially orthogonal flow structures which cannot be directly related to the flow instability. As an alternative of POD method, Dynamic Mode Decomposition (DMD) method was suggested to obtain the temporally orthogonal flow structure [Schmid, 2010]. Because of the characteristics of DMD, it can be expected that the obtained DMD mode could provide important information of flow instability.

Finally, laser-using flow instability frequency measurement should be conducted in detail. Because the flow is dissipated as it moves downward, the instability frequency would be different for each location [Schmitt et al., 2012; Zong and Yang, 2008]. Therefore, measurement of the frequency at various position along radial and axial direction would help the in-depth understanding of the flow instability.

## APPENDIX

### PROPER ORTHOGONAL DECOMPOSITION

#### A.1 Background

Proper Orthogonal Decomposition (POD) is the method which have been used for the analysis of the flow characteristics. This method have been used as the Principal Component Analysis (PCA) in statistics, and Karhunen-Loève Transform (KLT) in signal processing. POD method deduces the “modes” which represent the coherent structure of the flow. Each mode are spatially orthogonal, and the modes are ranked according to the energy/eigenvalue of each mode.

#### A.2 POD Analysis Procedure

The conventional process of POD analysis is shown in this section as follows.

First, the set of flow field data/spatially uncorrelated coherent structure  $V$  can be presented as Eq. A.1.

$$V = [v_1 \quad v_2 \quad v_3 \quad \cdots \quad v_n \quad \cdots \quad v_N]$$
$$= \begin{bmatrix} v_{1,1} & v_{1,2} & v_{1,3} & \cdots & v_{1,n} & \cdots & v_{1,N} \\ v_{2,1} & v_{2,2} & v_{2,3} & \cdots & v_{2,n} & \cdots & v_{2,N} \\ \vdots & \vdots & \vdots & \vdots & \vdots & \vdots & \vdots \\ v_{M,1} & v_{M,2} & v_{M,3} & \cdots & v_{M,n} & \cdots & v_{M,N} \end{bmatrix} \quad (\text{A.1})$$

$$v_n = \begin{bmatrix} v_{1,n} \\ v_{2,n} \\ \vdots \\ v_{M,n} \end{bmatrix} : n^{th} \text{ snapshot data} \quad (\text{A.2})$$



A shows the temporal evolution of coherent structures.

$$\begin{aligned}
 A &= [a_1 \quad a_2 \quad a_3 \quad \cdots \quad a_n \quad \cdots \quad a_N] \\
 &= \begin{bmatrix} a_{1,1} & a_{1,2} & a_{1,3} & \cdots & a_{1,n} & \cdots & a_{1,N} \\ a_{2,1} & a_{2,2} & a_{2,3} & \cdots & a_{2,n} & \cdots & a_{2,N} \\ \vdots & \vdots & \vdots & \vdots & \vdots & \vdots & \vdots \\ a_{n,1} & a_{n,2} & a_{n,3} & \cdots & a_{n,n} & \cdots & a_{n,N} \\ \vdots & \vdots & \vdots & \vdots & \vdots & \vdots & \vdots \\ a_{N,1} & a_{N,2} & a_{N,3} & \cdots & a_{N,n} & \cdots & a_{N,N} \end{bmatrix} \quad (\text{A.7})
 \end{aligned}$$

The symbol ‘\*’ means the conjugate transpose.

From these contents, the flowfield snapshot  $v_n$  can be represented as the linear summation of components of  $\Phi$ ,  $\Sigma$  and  $A$ .

$$\begin{aligned}
 v_n &= \sigma_1 a_{n,1} \phi_1 + \sigma_2 a_{n,2} \phi_2 + \sigma_3 a_{n,3} \phi_3 + \cdots + \sigma_N a_{n,N} \phi_N \\
 &= \sum_{i=1}^N \sigma_i a_{n,i} \phi_i \quad (\text{A.8})
 \end{aligned}$$

It can be thought that  $V$  is  $M$  by  $N$  matrix where  $M$  is number of flow field data point and  $N$  is number of snapshots. Because  $M$  is much larger than  $N$ , the full-size SVD might be impossible with limited computer source. Therefore, the reduced SVD can be adopted in the POD analysis. In this study, eigenvalue decomposition of covariance matrix  $Z$  was used as follows.

$$Z = V^* V = A \Sigma \Phi^* \Phi \Sigma A^* = A \Sigma^2 A^* \quad (\text{A.9})$$

By solving eigenvalue problem of  $Z$ ,

$$ZA = A \Sigma^2 \quad (\text{A.10})$$

$$VA = \Phi \Sigma \quad (\text{A.11})$$

By normalization of column in  $VA$  in Eq. A.11,  $\Phi$  can be calculated.  $\Sigma^2$  shows the eigenvalue or energy content of  $\phi$ . The eigenvalue for each mode can be related to the mode energy when  $v$  contains velocity data only and the flow is incompressible.

## **BIBLIOGRAPHY**

- Arienti M, Soteriou MC (2009) Time-resolved proper orthogonal decomposition of liquid jet dynamics. *Phys Fluids* 21:112104.
- Banuti DT, Hannemann K (2014) Supercritical pseudo-boiling and its relevance for transcritical injection. In: The 50th AIAA/ASME/SAE/ASEE Joint Propulsion Conference, Cleveland, USA.
- Bayvel L (1993) *Liquid Atomization* vol 1040. vol 2756. Taylor & Francis, Washington.
- Bazarov VG, Yang V (1998) Liquid-propellant rocket engine injector dynamics. *J Propul Power* 14:797-806.
- Berkooz G, Holmes P, Lumley JL (1993) The proper orthogonal decomposition in the analysis of turbulent flows. *Annu Rev Fluid Mech* 25:539-575.
- Borodin VA, Dityakin YF, Klyachko LA, Yagodkin VI (1968) *Atomization of Liquids*. Air Force Foreign Technology Division Report, FTD-MT-24-97-68 (AD685151).
- Chehroudi B (2010) Physical hypothesis for the combustion instability in cryogenic liquid rocket engines. *J Propul Power* 26:1153-1160.
- Chehroudi B, Cohn R, Talley D (2002a) Cryogenic shear layers: experiments and phenomenological modeling of the initial growth rate under subcritical and supercritical conditions. *International journal of heat and fluid flow* 23:554-563.
- Chehroudi B, Talley D, Coy E (2002b) Visual characteristics and initial growth rates of round cryogenic jets at subcritical and supercritical pressures. *Phys Fluids* 14:850-861.
- Chehroudi B, Talley D, Mayer W, Branam R, Smith JJ (2003) Understanding injection into high pressure supercritical environments. In: 5th International Symposium on Liquid Space Propulsion, Chattanooga, TN.
- Cho S, Park G, Chung Y, Yoon Y, Bazarov VG (2014) Surface instability on cryogenic swirl flow at sub- to supercritical conditions. *J Propul Power* 30:1038-1046.
- Clark CJ, Dombrowski N (1972) Aerodynamic instability and disintegration of inviscid liquid sheets. *Proceedings of the Royal Society of London A Mathematical and*

- Physical Sciences 329:467-478.
- Cooper D, Yule A (2001) Waves on the air core/liquid interface of a pressure swirl atomizer. In: The 17th Annual Conference on Liquid Atomization and Spray Systems, Zurich, Switzerland. 2001
- Culick FEC, Yang V (1995) Overview of combustion instabilities in liquid-propellant rocket engines. In: Yang V, Anderson WE (eds) Liquid rocket engine combustion instability, Progress in Astronautics and Aeronautics, vol 169. AIAA, Washington, DC, pp 3-37.
- Davis DW, Chehroudi B (2007) Measurements in an acoustically driven coaxial jet under sub-, near-, and supercritical conditions. *J Propul Power* 23:364-374.
- Decker M, Schik A, Meier UE, Stricker W (1998) Quantitative Raman imaging investigations of mixing phenomena in high-pressure cryogenic jets. *Appl Opt* 37:5620-5627.
- Dityakin YF, Klyachko LA, Novikov BV, Yagodkin VI (1977) Atomization of Liquids. Mashinostroenie, Moscow.
- Dombrowski N, Johns WR (1963) The Aerodynamic instability and disintegration of viscous liquid sheets. *Chem Eng Sci* 18:203-214.
- Donjat D, Estivalezes J-L, Michau M, Lavergne G (2003) Phenomenological study of the pressure swirl atomizer internal flow. In: The 9th International Conference on Liquid Atomization and Spray Systems, Sorrento, Italy.
- Eberhart CJ, Lineberry DM, Frederick Jr. RA (2012) Propellant throttling effects on self-pulsation of liquid rocket swirl-coaxial injection. In: 48th AIAA/ASME/SAE/ASEE Joint Propulsion Conference & Exhibit, Atlanta, USA.
- Fu Q-F, Yang L-J, Zhang W, Cui K-D (2012) Spray characteristics of an open-end swirl injector. *Atomization Spray* 22:431-445.
- Gallaire F, Rott S, Chomaz J-M (2004) Experimental study of a free and forced swirling jet. *Phys Fluids* 16:2907-2917.
- Han ZY, Parrish S, Farrell PV, Reitz RD (1997) Modeling atomization processes of pressure-swirl hollow-cone fuel sprays. *Atomization Spray* 7:663-684.

- Heo J-Y, Kim K, Sung H-G, Choi H-S, Yang V (2012) Numerical study for kerosene/LOx supercritical mixing characteristics of a swirl injector. In: 50th AIAA Aerospace Sciences Meeting including the New Horizons Forum and Aerospace Exposition.
- Huo H, Wang X, Yang V (2014) Flow dynamics of a simplex swirl injector at supercritical conditions. In: The 52nd Aerospace Sciences Meeting, National Harbor, USA.
- Hutt JJ, Cramer JM (1996) Advanced rocket injector development at the Marshall Space Flight Center. In: AIAA, Space Programs and Technologies Conference, Huntsville, AL. Sep.
- Im J-H, Kim D, Han P, Yoon Y, Bazarov V (2009) Self-pulsation characteristics of a gas-liquid swirl coaxial injector. *Atomization Spray* 19:57-74.
- Kenny RJ, Hulka JR, Moser MD, Rhys NO (2009) Effect of chamber backpressure on swirl injector fluid mechanics. *J Propul Power* 25:902-913.
- Khavkin Y (2004) *The Theory and Practice of Swirl Atomizers*. Taylor & Francis, New York.
- Kim D, Im J-H, Koh H, Yoon Y (2007) Effect of ambient gas density on spray characteristics of swirling liquid sheets. *J Propul Power* 23:603-611.
- Kim JG (2013) Spray structures in high pressure environment of gas-centered swirl coaxial injector for staged combustion cycle engines. Ph.D. Thesis, Seoul National University
- Kim S, Khil T, Kim D, Yoon Y (2009) Effect of geometric parameters on the liquid film thickness and air core formation in a swirl injector. *Meas Sci Technol* 20:015403.
- Landwehr F, Feggeler D, Walzel P, Weichert F, Schröter N, Müller H (2006) A fibre sensor based frequency analysis of surface waves at hollow cone nozzles. *Exp Fluids* 40:523-532.
- Lefebvre AH (1989) *Atomization and Sprays*. Hemisphere, New York.
- Liang H, Maxworthy T (2005) An experimental investigation of swirling jets. *J Fluid Mech* 525:115-159.
- Linstrom PJ, Mallard WG NIST Chemistry WebBook, NIST Standard Reference

- Database Number 69. National Institute of Standards and Technology, Gaithersburg MD, 20899, <http://webbook.nist.gov>, (retrieved February 6, 2013).
- Marchione T, Allouis C, Amoresano A, Beretta F (2007) Experimental investigation of a pressure swirl atomizer spray. *J Propul Power* 23:1096-1101.
- Markovich DM, Abdurakipov SS, Chikishev LM, Dulin VM, Hanjalić K (2014) Comparative analysis of low- and high-swirl confined flames and jets by proper orthogonal and dynamic mode decompositions. *Phys Fluids* 26:065109.
- Mayer W, Tamura H (1996) Propellant injection in a liquid oxygen/gaseous hydrogen rocket engine. *J Propul Power* 12:1137-1147.
- Mayer W, Telaar J, Branam R, Schneider G, Hussong J (2003) Raman measurements of cryogenic injection at supercritical pressure. *Heat and Mass Transfer* 39:709-719.
- Mayer WOH, Ivancic B, Schik A, Hornung U (2001) Propellant atomization and ignition phenomena in liquid oxygen/gaseous hydrogen rocket combustors. *J Propul Power* 17:794-799.
- Mayer WOH, Schik AH, Vielle B, Chauveau C, Gökalp I, Talley DG, Woodward RD (1998) Atomization and breakup of cryogenic propellants under high-pressure subcritical and supercritical conditions. *J Propul Power* 14:835-842.
- Meyer KE, Pedersen JM, Özcan O (2007) A turbulent jet in crossflow analysed with proper orthogonal decomposition. *J Fluid Mech* 583:199-227.
- Miller RS, Harstad KG, Bellan J (2001) Direct numerical simulations of supercritical fluid mixing layers applied to heptane–nitrogen. *J Fluid Mech* 436:1-39.
- Musemic E, Rojek A, Gaspar M, Weichert F, Müller H, Walzel P (2009) Experimental analysis and 3D-visualization of oscillating hollow-conical liquid sheets in quiescent air. In: *The 11th International Conference on Liquid Atomization and Spray Systems*, Vail, USA.
- Newman JA, Brzustowski T (1971) Behavior of a liquid jet near the thermodynamic critical region. *AIAA journal* 9:1595-1602.
- Oefelein JC, Yang V (1993) Comprehensive review of liquid-propellant combustion instabilities in F-1 engines. *J Propul Power* 9:657-677.

- Oefelein JC, Yang V (1998) Modeling high-pressure mixing and combustion processes in liquid rocket engines. *J Propul Power* 14:843-857.
- Oschwald M, Schik A (1999) Supercritical nitrogen free jet investigated by spontaneous raman scattering. *Exp Fluids* 27:497-506.
- Oschwald M, Smith J, Branam R, Hussong J, Schik A, Chehroudi B, Talley D (2006) Injection of fluids into supercritical environments. *Combustion Science and Technology* 178:49-100.
- Park H, Heister SD (2006) Nonlinear simulation of free surfaces and atomization in pressure swirl atomizers. *Phys Fluids* 18:052103-052111.
- Rubinsky VR (1995) Combustion instability in the RD-0110 engine. In: Yang V, Anderson WE (eds) *Liquid rocket engine combustion instability, Progress in Astronautics and Aeronautics*, vol 169. AIAA, Washington, DC, pp 89-112.
- Schmid PJ (2010) Dynamic mode decomposition of numerical and experimental data. *J Fluid Mech* 656:5-28.
- Schmitt T, Rodriguez J, Leyva IA, Candel S (2012) Experiments and numerical simulation of mixing under supercritical conditions. *Phys Fluids* 24:055104.
- Semeraro O, Bellani G, Lundell F (2012) Analysis of time-resolved PIV measurements of a confined turbulent jet using POD and Koopman modes. *Exp Fluids* 53:1203-1220.
- Senecal PK, Schmidt DP, Nouar I, Rutland CJ, Reitz RD, Corradini ML (1999) Modeling high-speed viscous liquid sheet atomization. *Int J Multiphas Flow* 25:1073-1097.
- Sterling AM, Sleicher CA (1975) The instability of capillary jets. *J Fluid Mech* 68:477-495.
- Strakey P, Talley D, Hutt J (2001) Mixing characteristics of coaxial injectors at high gas/liquid momentum ratios. *J Propul Power* 17:402-410.
- Syred N (2006) A review of oscillation mechanisms and the role of the precessing vortex core (PVC) in swirl combustion systems. *Prog Energ Combust* 32:93-161.
- Talley DG (2002) Recent developments in liquid rocket injectors. In: *Liquid Propulsion Systems—Evolution and Advancements*, Indianapolis, IN, USA. 11-12 July 2002
- Teshome S, Leyva I, Talley D, Karagozian A (2012) Cryogenic high-pressure shear-

- coaxial jets exposed to transverse acoustic forcing. In: The 50th AIAA Aerospace Sciences Meeting including the New Horizons Forum and Aerospace Exposition, Sashville, USA. Jan.
- Wang S, Hsieh S-Y, Yang V (2005) Unsteady flow evolution in swirl injector with radial entry. I. Stationary conditions. *Phys Fluids* 17:045106.
- Wegener JL, Forliti DJ, Leyva IA, Talley DG (2014) Receptivity of a cryogenic coaxial gas-liquid jet to acoustic disturbances. In: The 50th AIAA/ASME/SAE/ASEE Joint Propulsion Conference, Cleveland, USA.
- Yang V (2000) Modeling of supercritical vaporization, mixing, and combustion processes in liquid-fueled propulsion systems. *P Combust Inst* 28:925-942.
- Zong N, Meng H, Hsieh S-Y, Yang V (2004) A numerical study of cryogenic fluid injection and mixing under supercritical conditions. *Phys Fluids* 16:4248-4261.
- Zong N, Yang V (2008) Cryogenic fluid dynamics of pressure swirl injectors at supercritical conditions. *Phys Fluids* 20:056103.

## 초 록

극저온 스월 유동의 불안정 특성에 대한 실험적 연구를 수행하였다. 극저온 액체 질소를 스월 분사기를 통하여 고압 챔버 내에 분사시켰으며, 이때 유동의 주위 환경은 질소의 아임계 및 초임계 압력 조건이 되도록 변화시켰다. 초고속 카메라 촬영 기법을 이용하여 시간에 따라 빠르게 변화하는 유동의 이미지를 획득하였으며, 이미지 처리 기법을 이용하여 유동의 특성을 분석하였다. 또한 레이저 이용 유동 계측 기법 및 유동 이미지 분석을 통하여 유동의 불안정 주파수를 계측하였다.

우선, 아임계 및 초임계 조건에서의 유동 표면 불안정성을 연구하였다. 일반적인 액체 유동과 극저온 유동을 비교하였을 때 뚜렷한 거동의 차이를 확인하였으며, 이는 유동 중앙 재순환 영역에 존재하는 *precessing vortex core*에 의한 것으로 생각되었다. 유동의 주위 환경이 아임계 조건에서 초임계 조건으로 변화하였을 때 분사 유체의 상변화 및 밀도가 변화하였으며, 그에 따라 유동 후류의 거동, 유동의 분무각, 표면 파형 구조의 파장, 전파 속도 등의 유동 특성 또한 급격하게 변화하였다. 유동의 불안정 주파수를 측정하였을 때, 이는 *precessing vortex core* 불안정 주파수를 따르는 것이 발견되었다. 불안정 주파수는 주위기체압력 증가에 따라 유동 속도와 함께 감소하였으나, 주위 환경이 아임계 조건에서 초임계 조건으로 변화함에 따른 급격한 변화는 관찰되지 않았다. 이러한 결과는 유동의 표면 거동은 상변화된 분사 유체의 밀도에 의하여 크게 영향을 받으나, 불안정 특성은 액체 상태의 유동에 의하여 결정됨을 암시한다.

모드 분해 기법을 이용하여 아임계 및 초임계 조건에서의 극저온 스월 유동의 동적 특성을 실험적으로 연구하였다. 유동의 이미지로부터 다양한 불안정 구조의 중첩 및 와류 링 구조가 발견되었다. 유동의 분무각은 초임계 조건

에서 급격하게 감소하였으며, 이는 분사기 내부 유동의 독특한 상변화 과정에 따른 것으로 추측된다. 유동 이미지의 적합직교분해 (POD) 분석을 통하여 두 종류의 모드를 도출하였으며, 대칭/기울어진 링 형상 모드 및 반대칭 형상 모드가 존재함을 확인하였다. 대칭 모드는 Kelvin-Helmholtz 불안정에 의하여 생성되었으며, 반대칭 모드는 헬리컬 불안정에 의하여 발생하였다. 이때 헬리컬 불안정은 아임계 조건에서는 분사기 내부 액막의 불안정에 의하여 생성되는 반면, 초임계 조건에서는 유동 중앙 재순환 영역의 precessing vortex core 에 의하여 생성되는 것으로 추측된다. 한편, 유동의 후류 및 초임계 조건의 POD 모드에서 나타나는 고유 구조의 특성은 서로 유사하였다. 이는 유동의 거동이 분사 유체의 상태에 크게 영향을 받음을 나타낸다.

**중심어:** 액체 추진제 로켓 엔진, 단일 스월 분사기, 극저온 유동, 초임계조건, 유동 불안정, 적합직교분해법

**학 번:** 2009-30169



저작자표시-비영리-변경금지 2.0 대한민국

이용자는 아래의 조건을 따르는 경우에 한하여 자유롭게

- 이 저작물을 복제, 배포, 전송, 전시, 공연 및 방송할 수 있습니다.

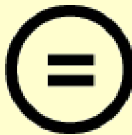
다음과 같은 조건을 따라야 합니다:



저작자표시. 귀하는 원저작자를 표시하여야 합니다.



비영리. 귀하는 이 저작물을 영리 목적으로 이용할 수 없습니다.



변경금지. 귀하는 이 저작물을 개작, 변형 또는 가공할 수 없습니다.

- 귀하는, 이 저작물의 재이용이나 배포의 경우, 이 저작물에 적용된 이용허락조건을 명확하게 나타내어야 합니다.
- 저작권자로부터 별도의 허가를 받으면 이러한 조건들은 적용되지 않습니다.

저작권법에 따른 이용자의 권리는 위의 내용에 의하여 영향을 받지 않습니다.

이것은 [이용허락규약\(Legal Code\)](#)을 이해하기 쉽게 요약한 것입니다.

[Disclaimer](#)

공학박사학위논문

**Instability of Cryogenic Swirl Flows  
under Subcritical to Supercritical Conditions**

아임계 및 초임계 조건에서  
극저온 스월 유동의 불안정성

2015년 2월

서울대학교 대학원

기계항공공학부

조성호

## ABSTRACT

Instability characteristics of cryogenic swirl flows were experimentally investigated. The cryogenic liquid nitrogen was injected into a high-pressure chamber through a simplex swirl injector under subcritical to supercritical conditions of nitrogen. High-speed photography with backlight imaging was used to obtain images of the temporally changing flow. The set of images was analyzed by the image processing method. The instability frequency was measured by flow image processing and the laser beam diagnostics.

Surface instability of the flow under subcritical to supercritical condition was investigated. Comparing the flow images of the cryogenic and conventional swirl flows, different behaviors were noted, and it was hypothesized that the instability of the cryogenic swirl flow was dominated by the precessing vortex core in the central toroidal recirculation zone. When the ambient condition of the flow was changed from subcritical to supercritical, the phase change and subsequent density change of the injectant differed and flow actions, such as the behavior of the downstream flow, the spray angle, the wavelength, and the propagation velocity, changed drastically. When measuring the frequency of the flow instability, it was found to correspond to that of the precessing vortex core instability. The frequency decreased with the ambient pressure due to the decreasing flow velocity, but it did not change drastically when the surrounding conditions changed from subcritical to supercritical. This implies that the interface of the flow is highly affected by the density of the phase-changed injectant, but that the instability of the flow is determined by the flow in a liquid state.

The dynamic characteristics of a cryogenic swirl flow under supercritical conditions were experimentally investigated using a mode decomposition method. Superposed instability structures and vortex ring structures were found in the instantaneous flow image. The spray angle was decreased under supercritical conditions because of the unusual phase change of the injectant inside the injector. Two kinds of modes were deduced by POD analysis of the flow images. The analysis showed that two types of modes exist: a symmetric/tilted-ring shaped mode and an anti-symmetric shaped mode.

The Kelvin-Helmholtz instability mechanism generated the symmetric mode. The anti-symmetric structure was created by helical instability, which was generated by the instability of the liquid film inside the injector under subcritical conditions. However, under supercritical conditions, the precessing vortex core in the central toroidal recirculation zone determined the unstable behavior of the flow. A spatial and temporal analysis of the POD modes supported this explanation for the instability. Meanwhile, the spatial characteristics of the coherent structures became similar in the downstream region or under supercritical conditions, which implicates the strong influence of the state of the injectant in flow behavior.

**Keywords:** Liquid Propellant Rocket Engine, Simplex Swirl Injector, Cryogenic Flow, Supercritical Condition, Flow Instability, Proper Orthogonal Decomposition

**Student Number:** 2009-30169

# LIST

ABSTRACT .....	i
LIST.....	iii
LIST OF FIGURES.....	vi
LIST OF TABLES.....	ix
NOMENCLATURE.....	x

## CHAPTER 1

INTRODUCTION.....	1
1.1 Background and Motivation.....	1
1.2 Survey of Relevant Literature .....	5
1.2.1 Characteristics of fluid under supercritical condition .....	5
1.2.2 Single and coaxial jet flow .....	6
1.2.3 Jet flow with external excitation .....	8
1.2.4 Simplex swirl flow .....	9
1.3 Scope of Study.....	10

## CHAPTER 2

EXPERIMENTAL METHOD .....	11
2.1 Experimental Apparatus .....	11
2.1.1 Design procedure of swirl injector .....	11
2.1.2 High-pressure chamber .....	17
2.1.3 Cryogenic fluid feeding system .....	19
2.2 Flow Measurement .....	20
2.2.1 High-speed photography .....	21
2.2.2 Flow instability frequency measurement .....	23

CHAPTER 3	
SURFACE INSTABILITY ON CRYOGENIC SWIRL FLOW	
UNDER SUB- TO SUPERCRITICAL CONDITIONS.....	24
3.1 Background and Objectives .....	24
3.2 Experimental Methods .....	27
3.2.1 Injector design.....	27
3.2.2 Experimental conditions.....	28
3.2.3 Experimental techniques .....	30
3.3 Results and Discussion .....	31
3.3.1 Characteristics of the cryogenic swirl flow .....	31
3.3.2 Effect of the ambient pressure on a cryogenic swirl flow surface.....	34
3.3.3 Instability analysis of a cryogenic swirl flow surface.....	43
 CHAPTER 4	
DYNAMIC CHARACTERISTICS OF A CRYOGENIC SWIRL FLOW	
UNDER SUPERCRITICAL CONDITIONS.....	46
4.1 Background and Objectives .....	46
4.2 Experimental Methods .....	48
4.2.1 Injector design.....	48
4.2.2 Experimental conditions.....	50
4.2.3 Experimental techniques .....	51
4.2.4 Proper Orthogonal Decomposition.....	51
4.3 Results and Discussion .....	54
4.3.1 Static characteristics of a cryogenic flow .....	54
4.3.2 POD analysis of flow image .....	57
4.3.3 Analysis of POD mode.....	69
 CHAPTER 5	
CONCLUSION AND FUTURE WORK.....	74
5.1 Conclusion .....	74

5.2 Recommendations for Future Work.....	76
APPENDIX	
PROPER ORTHOGONAL DECOMPOSITION.....	77
A.1 Background .....	77
A.2 POD Analysis Procedure .....	77
BIBLIOGRAPHY .....	81
ABSTRACT IN KOREAN.....	87

## LIST OF FIGURES

Fig. 1.1	Combustion process in liquid propellant rocket engine	2
Fig. 1.2	Hierarchy of injector experiments [Talley, 2002]	2
Fig. 1.3	Transcritical process of liquid propellant in combustion chamber of liquid propellant rocket engine	4
Fig. 2.1	Schematic of liquid swirl injector [Kim, 2013]	12
Fig. 2.2	High-pressure chamber	18
Fig. 2.3	Air curtain system	18
Fig. 2.4	Cryogenic fluid feeding system	19
Fig. 2.5	Flow condition measurement inside swirl injector	21
Fig. 2.6	High-speed photography	22
Fig. 2.7	Flow instability frequency measurement using Ar-Ion laser	23
Fig. 3.1	Open-type simplex swirl injector (unit: mm)	27
Fig. 3.2	Experimental conditions in Pressure-Temperature diagram of nitrogen	29
Fig. 3.3	Instantaneous swirl flow image at $\Delta P = 1$ MPa, $P_c = 1$ MPa for (a) cryogenic swirl flow and (b) water swirl flow; (left) original image and (right) flow boundary	32
Fig. 3.4	Representative swirl flow images under various ambient pressure conditions for instantaneous image (top row) and averaged image (bottom row) at $\Delta P = 0.5$ MPa	35
Fig. 3.5	Instantaneous swirl flow image at $\Delta P = 0.5$ MPa for (a) $P_c = 2$ MPa (subcritical conditions) and (b) $P_c = 4$ MPa (supercritical conditions); (left) original image and (right) flow boundary	36
Fig. 3.6	Spray angle of cryogenic swirl flow	38
Fig. 3.7	Image analysis of cryogenic swirl flow for (a) sinusoidal wave imposed on plane liquid sheet, (b) flow boundary detection and (c) sine curve fitting of flow surface	40

Fig. 3.8	Wave amplitude on surface of cryogenic swirl flow	41
Fig. 3.9	Wavelength on surface of cryogenic swirl flow	42
Fig. 3.10	Propagation velocity of surface wave in axial direction	42
Fig. 3.11	Results from spectral analysis of transmission rate at $\Delta P = 0.5$ MPa under various ambient pressure conditions: (a) $P_c = 2$ MPa, (b) $P_c = 4$ MPa	45
Fig. 3.12	Instability frequency of cryogenic swirl flow	45
Fig. 4.1	Schematic of the simplex swirl injector (unit: mm)	49
Fig. 4.2	Experimental conditions in Pressure-Temperature diagram of nitrogen	50
Fig. 4.3	Analysis area of the flow image for the upstream (yellow line) and downstream (red line) regions	53
Fig. 4.4	Representative images of the cryogenic swirl flow; instantaneous (left column) and averaged (right column) images for (a) subcritical, (b) critical, (c) supercritical ambient conditions, and (d) structures on the flow surface	55
Fig. 4.5	Spray angle of the cryogenic swirl flow	56
Fig. 4.6	POD mode eigenvalue distribution for the experimental conditions; (a) upstream modes, and (b) downstream modes	58
Fig. 4.7	Initial 10 POD modes for subcritical condition ( $P_c = 2.0$ MPa); upstream region	59
Fig. 4.8	Initial 10 POD modes for subcritical condition ( $P_c = 2.0$ MPa); downstream region	60
Fig. 4.9	Initial 10 POD modes for critical condition ( $P_c = 3.4$ MPa); upstream region	61
Fig. 4.10	Initial 10 POD modes for critical condition ( $P_c = 3.4$ MPa); downstream region	62
Fig. 4.11	Initial 10 POD modes for supercritical condition ( $P_c = 5.0$ MPa); upstream region	63

Fig. 4.12	Initial 10 POD modes for supercritical condition ( $P_c = 5.0$ MPa); downstream region	64
Fig. 4.13	Representative POD modes of the upstream cryogenic swirl flow; symmetric/tilted-ring structure (left column) and anti-symmetric structure (right column) modes for (a) subcritical, (b) critical, and (c) supercritical ambient conditions	67
Fig. 4.14	Representative POD modes of the downstream cryogenic swirl flow; symmetric/tilted-ring structure (left column) and anti-symmetric structure (right column) modes for (a) subcritical, (b) critical, and (c) supercritical ambient conditions	68
Fig. 4.15	Conjugate pair analysis of POD modes at $P_c = 2.0$ MPa (upstream region): (a) conjugate mode images, and (b) cross-power spectral density for conjugate modes	70
Fig. 4.16	Instability frequency of POD modes in the cryogenic swirl flow	71
Fig. 4.17	Wavelength of POD modes in the cryogenic swirl flow	73

## LIST OF TABLES

Table 1.1	Recently developed liquid propellant rocket engines [Talley, 2002]	3
Table 1.2	Table 1.2 Critical properties of fluids	4
Table 3.1	Injector geometry	28
Table 3.2	Experimental conditions	30
Table 4.1	Injector geometry	49
Table 4.2	Experimental conditions	51

## NOMENCLATURE

### *Alphabet*

$A_0$	cross-section area of discharge orifice
$a_{i,n}$	time coefficient of POD mode
$C$	open coefficient
$C_d$	discharge coefficient
$C_{d,eq}$	equivalent discharge coefficient
$D_s$	swirl chamber diameter
$d_L$	manufacture diameter
$d_{o,i}$	inner diameter of orifice exit
$d_{o,o}$	outer diameter of orifice exit
$d_p$	diameter of tangential inlet
$f$	frequency
$I$	laser beam intensity
$I_0$	Initial laser beam intensity
$K$	injector geometric constant, $Rr_o/ir_p^2$
$K_D$	injector geometric constant concerning deformation effect
$K_{eq}$	equivalent injector geometric constant
$k$	wave number
$L$	length of the injector
$M$	number of data points in flow field
$\dot{m}_l$	spray mass flow rate
$N$	number of snapshots/images used in POD analysis
$n$	number of tangential inlet
$P_c$	chamber pressure
$R$	swirl arm from axis of injector to center of tangential inlet
$Re_p$	Reynolds number of tangential entry
$r_o$	radius of orifice exit

$r_p$	radius of tangential inlet
$r_{p,eq}$	equivalent radius of tangential inlet
$r_r'$	radius of gas core at orifice exit
$S$	dimensionless radius of gas core in discharge orifice, $r_r'/r_0$
$T_c$	ambient chamber temperature
$t$	time
$u$	axial velocity
$V$	set of flow field snapshots
$v$	flow field snapshot
$w$	tangential velocity
$x$	distance from injector post along liquid sheet
$Z$	companion matrix of POD

### ***Greek***

$\alpha$	Spray angle
$\alpha_{ideal}$	Ideal spray angle
$\alpha_{eq}$	Equivalent spray angle
$\Delta_{in}$	Energy loss at tangential entry
$\Delta_k$	Energy loss at wall of vortex chamber
$\Delta_L$	Energy loss due to swirl chamber wall length
$\Delta_{noz}$	Energy loss at converging part
$\Delta P_{ideal}$	ideal injection differential pressure
$\Delta P_{eq}$	equivalent injection differential pressure
$\varepsilon$	Jet deformation rate
$\eta_0$	wave amplitude
$\lambda_i$	eigenvalue of POD mode
$\lambda_k$	friction coefficient
$\lambda_{laser}$	Laser wavelength

$\Phi$	set of POD modes
$\varphi$	filling efficiency
$\varphi_c$	corrected filling efficiency
$\phi_i$	$i$ th POD mode
$\Psi$	injector contraction angle
$\omega$	wave growth rate

### ***Subscripts***

$c$	chamber
$eq$	equivalent value
$l$	liquid
$o$	discharge orifice

# CHAPTER 1

## INTRODUCTION

### 1.1 Background and Motivation

A combustion occurred in a liquid propellant rocket engine is an important process which determines performance of the engine. Comprehensive study of the combustion process in the rocket engine is required to improve the understanding and acquire crucial information of combustion phenomena which can be used in the engine development.

The detailed combustion process is shown in Fig. 1.1. In the liquid propellant rocket engine, fuel and oxidizer are injected into the chamber through the injector. Propellants in liquid state are then atomized, vaporized and mixed inside the chamber. The combustion process of the propellants starts and the combusted gas is created. These products of combustion expands through the nozzle of the engine and finally generates the thrust. In this process, injector dominates the atomization process and affects the combustion of the propellants.

Because the injector has a huge influence on the performance of the liquid propellant rocket engine, the development of liquid propellant rocket engine starts from the design of the injector in consideration of engine performance requirement [Talley, 2002]. After injector design, cold flow test under atmospheric pressure is usually conducted using single injector element. Then the experiment under high pressure or supercritical condition is carried out. Hot fire test is followed after cold flow test; single element test and subscale multi-element test are conducted. Finally, full scale testing is carried out and the engine development is finished. This process is shown in Fig. 2.2.

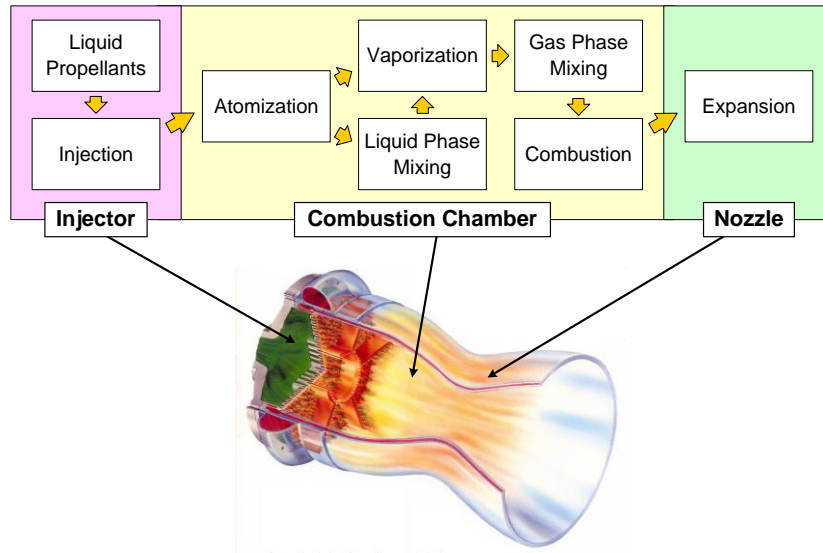


Fig. 1.1 Combustion process in liquid propellant rocket engine

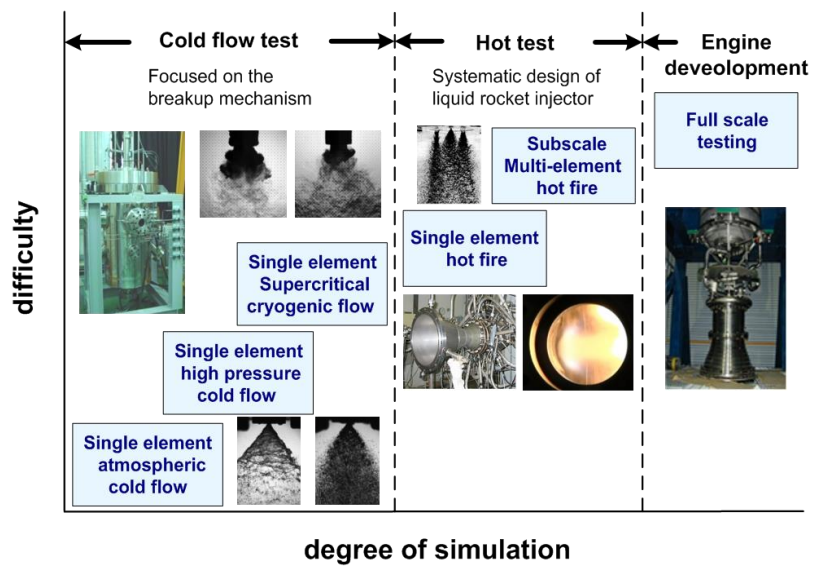


Fig. 1.2 Hierarchy of injector experiments [Talley, 2002]

It is well known that the higher chamber pressure allows the higher specific impulse for the engine [Oschwald et al., 2006]. Thus, as shown in Table 1.1, recently developed liquid propellant rocket engines operates under high pressure and temperature conditions to acquire the high performance. In this situation, the pressure and temperature inside the combustion chamber exceeds the critical conditions of the injected propellants. As a result, the state of the propellants injected into the chamber is changed from liquid to supercritical fluid. This phase change process is called “transcritical process” [Chehroudi et al., 2003; Mayer et al., 1998; Yang, 2000]. In this process, propellants are injected first. The pressure is decreased and temperature is increased, and the propellants are remained in liquid state. Because of the high temperature of the combustion chamber (~ 3000 K), propellants are then heated. The propellants are then changed from liquid to supercritical fluid, and the thermophysical properties are changed drastically.

Table 1.1 Recently developed liquid propellant rocket engines [Talley, 2002]

Vehicle	Year	Engine	Injector type	Propellants	Combustion pressure (MPa)
Ariane 5	1996	Vulcain	Shear coaxial	LOx / H <sub>2</sub>	10
Ariane 5E	Dev.	VINCI	Shear coaxial	LOx / H <sub>2</sub>	6
Atlas V	2002	RD-180	Swirl coaxial	LOx / RP-1	26.7
Delta IV	2002	RS-68	Shear coaxial	LOx / H <sub>2</sub>	10.2
H-II	1994	LE-7	Shear coaxial	LOx / H <sub>2</sub>	12.7
Space Shuttle	1981	RS-25	Shear coaxial	LOx / H <sub>2</sub>	20.6
Titan IV	1997	LR-87	Shear coaxial	N <sub>2</sub> O <sub>4</sub> / Aerozine-50	6
Falcon-9	2010	Merlin	Pintle	LOx / RP-1	9.7
Antares	2013	NK-33	Swirl coaxial	LOx / RP-1	14.5

Table 1.2 Critical properties of fluids

Fluid	Critical pressure (MPa)	Critical Temperature (K)
N <sub>2</sub>	3.39	126.2
O <sub>2</sub>	5.04	154.6
H <sub>2</sub>	1.31	33.2
He	0.23	5.2
CH <sub>4</sub>	4.59	190
RP-1	2.17	662

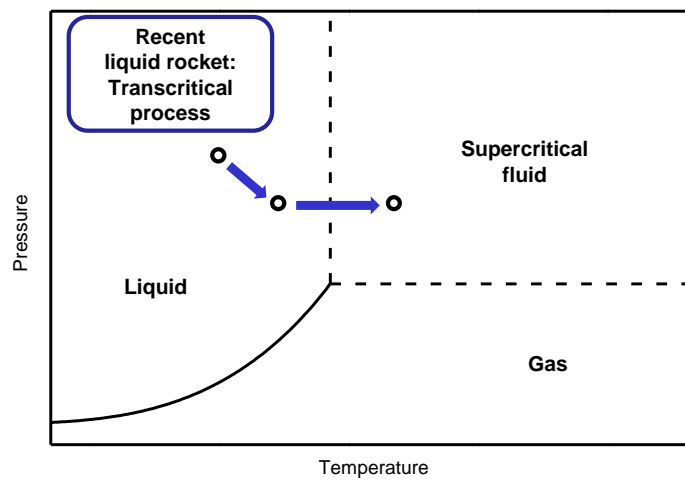


Fig. 1.3 Transcritical process of liquid propellant in combustion chamber of liquid propellant rocket engine

In case of the propellant injection under supercritical condition, conventional liquid atomization model cannot be used to explain the breakup process inside the combustion chamber. Therefore, the combustion characteristics to the new model should be suggested which can explain the behavior of the liquid propellant in transcritical process. Various studies of the fluid injection under supercritical condition have been conducted for this purpose with experimental and numerical approach.

## **1.2 Survey of Relevant Literature**

The first study about liquid atomization in near-critical region was conducted in 1970's [Newman and Brzustowski, 1971]. However, because of the difficulty of experiment and lack of interest, systematic investigations about this topic was started after 1990's. Most of the related studies were conducted by the German Aerospace Center (DLR) and the Air Force Research Laboratory in USA (AFRL).

The studies conducted using experimental approach mainly used liquid nitrogen as a simulant of LOx; the critical properties of the nitrogen and oxygen are similar, and the handling of liquid nitrogen was easier than LOx. The LOx flow was investigated by numerical analysis. Because the study of transcritical injection process was conducted to reveal the breakup mechanism and characteristics of non-reacting flow, single/coaxial jet with/without external excitation was considered and the reacting flow is not included in this section.

### **1.2.1 Characteristics of fluid under supercritical condition**

Among the various properties of the fluid, surface tension is the most important property in breakup process. With this property, liquid resists expansion of its surface area [Lefebvre, 1989]. The external force must exceed the surface tension force to achieve atomization. In supercritical fluid, however, surface tension is diminished [Mayer et al., 2001; Oswald et al., 2006]. As a result, the liquid-gas like breakup process and gas-gas

like mixing behavior can be observed in transcritical process [Chehroudi et al., 2003].

For coaxial injection of  $O_2$  and  $H_2$  in the liquid propellant rocket engine, mixing and burning phenomena of oxidizer and fuel occurs at the shear layer between two fluids. The critical properties of a mixture should be considered. Single critical point cannot be defined, but critical mixing lines define the state of the mixture. The solubility and the surface tension is determined by the pressure, temperature and mole fraction of the mixture. Previous study [Mayer et al., 2001] found that the critical temperature decreases with increasing pressure. Surface tension would exist in the mixture while the pressure is above the critical pressure of pure  $O_2$ . It implies that the solubility of liquid droplet would be decreased when the surrounding gas is the mixture [Mayer et al., 1998]. Surface tension decreased with the increase of pressure and temperature.

The properties of the fluid become very sensitive at the near-critical pressure condition. The specific heat would reach maximum peak value at certain temperature. At this temperature, the fluid would behave like a liquid at boiling point. This point is called pseudo-boiling point, and the thermal diffusivity reaches a distinct minimum. Because of the unusual characteristics of this point, further study of flow behavior should be conducted in consideration of pseudo-boiling [Banuti and Hannemann, 2014].

### **1.2.2 Single and coaxial jet flow**

Jet flow can be observed in the liquid propellant rocket engines developed in USA and Europe, which uses impinging type injector and shear coaxial type injector. To understand the mechanism of liquid breakup under supercritical conditions, the simplest and most fundamental case of the flow was investigated first. Various experimental methods have been adopted for the research of the jet flow in qualitative and quantitative manner. The investigation of coaxial jet was followed.

The qualitative analysis of jet surface was conducted first [Chehroudi et al., 2002b; Mayer and Tamura, 1996; Mayer et al., 1998]. In these studies, the different breakup mechanism of single jet was observed. Under subcritical condition, annular liquid jet was

atomized and droplet was found on the flow surface. However, the comb-like structure caused by transcritical process existed on the surface under supercritical conditions. This phenomena was caused by the existance of mixing layer around the jet surface. The injectant behaved like a dense gas in this condition. Although the density variation was very large, the buoyancy effect could be ignored [Chehroudi et al., 2002b].

The length of the single jet was measured by flow imaging [Chehroudi et al., 2003]. The measured dark core region of the jet was thought as potential core. However, the results obtained from the flow imaging was slightly different to the result obtained from Raman scattering method [Mayer et al., 2003].

Research of the growth rate of the single jet has been conducted intensively because it provides a mixing characteristics of the jet. In AFRL, the first quantitative analysis of the growth rate of single jet was conducted [Chehroudi et al., 2002b]. They plotted the growth rate along the density ratio of injectant and ambient gas, and compared the result to the previous works about gas jet. The obtained results showed that the co-existence of liquid-like and gas-like behavior of the jet. By adopting the concept of appropriate characteristic time such as bulge formation time and the gasification time, phenomenological model of the jet growth rate was developed. The results showed good agreement with the results obtained from Raman scattering method [Chehroudi et al., 2002a].

For the quantitative measurement of the flow, Raman scattering measurement method was adopted [Chehroudi et al., 2002a; Oswald and Schik, 1999]. The density and temperature distribution of the flow field were then measured by this method. As the initial injection temperature decreased, the density decay was slower. Because of pseudo-boiling effect, the temperature of jet was maintained while the specific volume was increased with the heat transfer to the jet [Oswald and Schik, 1999]. The self-similarity of the density field was observed in jet flow [Chehroudi et al., 2002a].

The investigation of coaxial jet used measurement methods similar to the single jet. One more parameter, the velocity ratio between inner liquid jet and outer gas jet, was considered in this subject. In LN<sub>2</sub>/GN<sub>2</sub> coaxial jet, the outer coaxial gas jet played two

roles; the assistance of inner jet breakup and the heat transfer behavior [Davis and Chehroudi, 2007]. The dark core length decreased along the increase of velocity ratio, and the length was drastically decreased under supercritical conditions.

### **1.2.3 Jet flow with external excitation**

The study of jet with external excitation is required to reveal the effect of combustion instability to the behavior of the injected propellant. For example, the fluctuation of the flow can interact with the velocity fluctuation parallel to the injector face [Oefelein and Yang, 1993].

In both single and coaxial jets, the impact of the external forcing to the jet was significant under subcritical conditions [Davis and Chehroudi, 2007]; the fluctuation of dark core length was larger than that under supercritical conditions. In coaxial jet flow, higher outer jet velocity would decrease the fluctuation of jet length. From these results, it can be deduced that flow under supercritical condition with high velocity of coaxial flow is less sensitive to the external excitation. Therefore it would be announced that the probability of combustion instability can be reduced under this flow condition.

A numerical analysis about the coaxial jet with external excitation was conducted [Schmitt et al., 2012]. The results obtained from this study was similar to that from experimenatal studies. However, the analysis of dynamic characteristics of the flow showed interesting results. When the flow has natural frequency, then the response of the flow to the excitation followed its natural frequency; the flow oscillated with the sub-harmonic of excitation frequency, which is similar to the natural frequency of the flow.

#### 1.2.4 Simplex swirl flow

Although lots of research about jet flow have been conducted, the swirl flow under supercritical flow was rarely studied. In contrast with shear-coaxial injector which generates jet flow, swirl injector enhances mixing because of the impartment of radial momentum to the injectant. Therefore, his type of injector have been used in many liquid propellant rocket engines developed in Russia [Bazarov and Yang, 1998; Borodin et al., 1968; Khavkin, 2004]. However, many research about the swirl injector was not introduced to USA or Europe which mainly concerned about single and coaxial jet flow found in the rocket engines using shear-coaxial injector. Moreover, the swirl flow is more complicated than the jet flow and difficult to examine. Therefore, the swirl flow under supercritical condition was less favored from DLR and AFRL.

It is difficult to find the experimental study of swirl flow under supercritical condition. In Marshall Space Flight Center, characteristics of the swirling LO<sub>x</sub>/GH<sub>2</sub> jet coaxial flow were investigated experimentally [Hutt and Cramer, 1996]. They found the periodic occurrence of globules in LO<sub>x</sub> spray breakup process, and the vanishment of the surface tension near the critical pressure. However, this study conducted qualitative investigation only, and additory research was not carried out.

The numerical analysis of swirl flow under supercritical condition have been attempted more frequently than experimental approach. Dynamic characteristics of LO<sub>x</sub> flow under supercritical condition was investigated first [Zong and Yang, 2008]. The flow was injected from open-type swirl injector, and the instability mechanism inside and outside of the injector was revealed. While the hydrodynamic instability and the acoustic oscillation generated instability of the flow inside the injector element, Kelvin-Helmholtz instability and Precessing Vortex Core instability dominated the external flow instability. The effect of injector geometry and swirl strength also was investigated. Additional research of the injector with similar geometry was followed [Heo et al., 2012; Huo et al., 2014].

### **1.3 Scope of Study**

This study aimed to conduct experimental investigation of the characteristics of the cryogenic swirl flows under subcritical to supercritical conditions, especially LOx swirl flow. The liquid nitrogen was used as a simulant of the LOx, and the simplex swirl injector was used to create conical liquid sheet. The ambient condition of the flow was controlled by high-pressure chamber. The behavior of the flow was measured with high-speed photography and laser diagnostics method. The static and dynamic characteristics of the flow along the ambient conditions were observed.

In Chapter 2, the experimental methods used in this study was explained. The design process of the swirl injector, high-pressure chamber and cryogenic fluid feeding system were described. The high-speed photography and flow instability frequency measurement were also introduced. In Chapter 3, flow characteristics injected by open-type swirl injector were studied. Differences between cryogenic flow and conventional liquid flow were observed first, and the characteristics of flow pattern were investigated. Wavy structure on flow surface was analyzed in quantitative manner. The frequency of flow instability were measured. In Chapter 4, dynamic characteristics of flow injected by closed-type swirl injector were studied. The spatial and temporal characteristics of flow dynamics was revealed by application of mode decomposition method to the flow image set. Finally, whole results were concluded in Chapter 5.

## **CHAPTER 2**

### **EXPERIMENTAL METHOD**

#### **2.1 Experimental Apparatus**

The experiments conducted in this study aimed to simulate the liquid oxygen flow in the combustion chamber of the liquid propellant rocket engine. Therefore, liquid nitrogen was injected into a high-pressure chamber through a simplex swirl type injector. Liquid nitrogen was used as a working fluid to simulate liquid oxygen. Owing to the similar critical properties of these fluids (nitrogen: 3.39 MPa/126.2 K; oxygen: 5.04 MPa/154.6 K) as shown in Table 1.1, liquid nitrogen has been used in many studies as a simulant of liquid oxygen for safety purposes [Chehroudi et al., 2002b; Mayer and Tamura, 1996; Schmitt et al., 2012; Zong et al., 2004]. The simplex swirl type injector was mounted inside the high-pressure chamber to create the hollow-cone shape swirl flow. The cryogenic fluid feeding system was used to maintain nitrogen in liquid state and feed the fluid into the high-pressure chamber. The high-pressure chamber was used to control the ambient condition of the flow and change it from subcritical to supercritical condition of the liquid nitrogen.

##### **2.1.1 Design procedure of swirl injector**

Many type of the injectors such as jet injector, impinging injector, pintle injector and swirl injector are used in the liquid propellant rocket engines. Among these, the swirl type injector is widely used in the engine developed in Russia [Bazarov and Yang, 1998; Khavkin, 2004]. This injector type has many advantages compared to the other injectors [Bazarov and Yang, 1998; Borodin et al., 1968; Dityakin et al., 1977; Khavkin, 2004; Lefebvre, 1989]. A schematic of the liquid swirl injector is shown in Fig. 2.1.

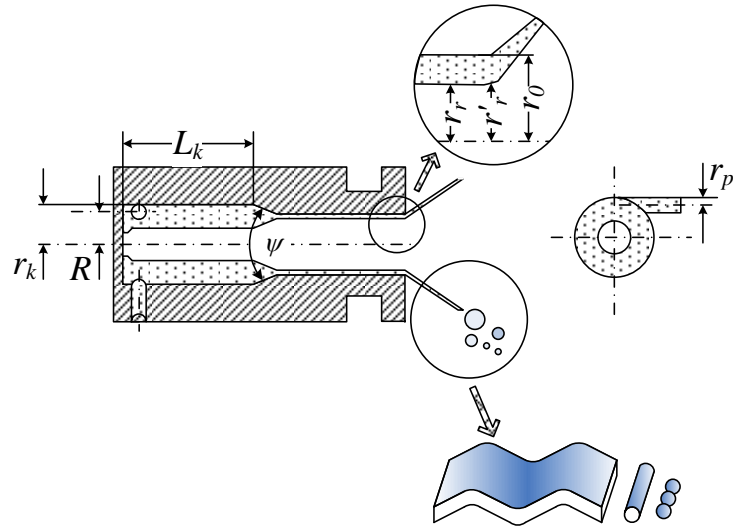


Fig. 2.1 Schematic of liquid swirl injector [Kim, 2013]

Before the design of swirl type injector, the performance and the size of the engine should be confirmed [Kim, 2013]. After this process, density of the propellant  $\rho$ , mass flow rate  $\dot{m}_l$ , injector nozzle diameter  $d_o$ , number of tangential inlet  $n$ , length of the injector  $L$  and ideal value of injection differential pressure  $\Delta P_{ideal}$  are determined. The design process of the injector starts with these variables, and the equivalent tangential inlet radius  $r_{p,eq}$  and equivalent injection differential pressure  $\Delta P_{eq}$  are finally obtained.

The design process is based on the ideal liquid theory and viscous liquid theory (reference). Approximated injector design is deduced from the ideal liquid theory, and the deformation and viscous effect on the flow is concerned in viscous liquid theory for correction of the design.

### 1. Ideal liquid theory

From the ideal liquid theory, discharge orifice area  $A_o$ , discharge coefficient  $C_d$ , and the filling efficiency  $\varphi$  should be calculated first.

$$A_o = \frac{\pi}{4} d_{o,i}^2 \quad (2.1)$$

$$C_d = \frac{\dot{m}_l}{A_o \sqrt{2\rho\Delta p_{ideal}}} \quad (2.2)$$

$$C_d = \sqrt{\frac{\varphi^3}{2-\varphi}} \rightarrow \varphi \quad (2.3)$$

$$K = \frac{(1-\varphi)\sqrt{2}}{\varphi\sqrt{\varphi}} \quad (2.4)$$

$K$  is the geometric constant. It determines the swirling strength of the injected fluid.

$$C = \frac{R}{r_o} \rightarrow R = Cr_o \quad (2.5)$$

$C$  is the open coefficient. The value of  $C$  is 0.915 for open type injector and 1.25 ~ 5.0 for closed type injector [Bayvel, 1993; Khavkin, 2004]. The swirl arm  $R$  can be determined with Eq. 2.5.

The tangential inlet radius  $r_p$  and the spray angle  $\alpha_2$  is finally deduced by Eq. 2.6 ~ 2.9.

$$K = \frac{Rr_o}{nr_p^2} \rightarrow r_p = \sqrt{\frac{Rr_o}{nK}} \quad (2.6)$$

$$C_d = \sqrt{1 - C_d^2 K^2} - S \sqrt{S^2 - C_d^2 K^2} - C_d^2 K^2 \ln \frac{1 + \sqrt{1 - C_d^2 K^2}}{S + \sqrt{S^2 - C_d^2 K^2}} \quad (2.7)$$

$$S = \frac{r_r'}{r_o} \quad (2.8)$$

$$\tan \frac{\alpha_2}{2} = \frac{2C_d K}{\sqrt{(1+S)^2 - 4C_d^2 K^2}} \quad (2.9)$$

## 2. Viscous liquid theory

In the real flow inside the swirl injector, non-negligible deformation of the jet can be occurred at the tangential entries inside the vortex chamber.  $K_D$ , geometric constant concerning deformation effect, and the corrected filling efficiency  $\varphi_c$  are calculated via Eq. 2.10 using jet deformation factor  $\varepsilon$  [Borodin et al., 1968].

$$K_D = \frac{K}{\varepsilon} = \frac{(1 - \varphi_c) \sqrt{2}}{\varphi_c \sqrt{\varphi_c}} \rightarrow \varphi_c \quad (2.10)$$

From  $K_D$ , the tangential inlet radius  $r_{p,eq}$  can be deduced.

$$K_D = \frac{Rr_o}{ir_{p,eq}^2} \rightarrow r_{p,eq} = \sqrt{\frac{Rr_o}{nK_D}} \quad (2.11)$$

The swirl chamber diameter  $D_s$  can be calculated by Eq. 2.12.

$$D_s = 2R + 2r_p + 2d_L, \quad (2.12)$$

$d_L$  is manufacture diameter.

In the viscous flow, friction effect should be considered to explain the flow motion. Friction due to the rotating flow in vortex chamber can cause the decrease in the spray angle. Therefore, friction factor  $\theta$  should be calculated from  $K_D$ , Reynolds number of a tangential entry  $Re_p$  and friction coefficient  $\lambda_k$  to obtain the equivalent spray angle in viscous flow  $\alpha_{eq}$  [Sterling and Sleicher, 1975].

$$\theta = \frac{\lambda_k}{2} K_D \left( \frac{r_k}{r_o} - 1 \right), \quad Re_p = \frac{\dot{m}_l}{\frac{\pi}{4} \mu_l d_p \sqrt{n}} \quad (2.13)$$

$$\text{where } \lambda_k = \frac{1.22}{Re_p^{0.36}} \left( Re_p > 2.3 \times 10^3 \right), \quad \lambda_k = \frac{24.6}{Re_p^{0.75}} \left( Re_p < 2.3 \times 10^3 \right)$$

$$\bar{\alpha} = \frac{\alpha_{eq}}{\alpha_{ideal}} = f(\theta) \quad \rightarrow \quad \alpha_{eq} = \bar{\alpha} \times \alpha_{ideal} \quad (2.14)$$

In the swirl injector, hydraulic losses caused by friction can be found at the tangential entry, wall of the vortex chamber, and the converging part [Bayvel, 1993; Borodin et al., 1968; Dityakin et al., 1977]. These losses change the discharge coefficient and the required injection differential pressure.

First, the energy loss at tangential entry  $\Delta_{in}$  can be determined in Eq. 2.15.

$$\Delta_{in} = \xi_{in} \frac{K_D^2}{C^2}; \quad C = \frac{R}{r_0} \quad (2.15)$$

The energy loss at the wall of the vortex chamber  $\Delta_k$  can be calculated by Eq. 2.16

$$\Delta_k = \frac{\lambda_k}{\sigma^2} \left\{ \frac{1}{\sigma} \left( 1 - \frac{1}{C_k} \right) + \lambda_k \left[ \left( \frac{K_e}{2} - \frac{1}{2\sigma - \lambda_k} \right) \left( \frac{2}{\sigma} + \frac{K_e}{2} + \frac{1}{2\sigma - \lambda_k} \right) + \frac{3}{2\sigma^2} \ln \frac{(2\sigma - \lambda_k) K_e C_k}{2} \right] \right\}; \quad (2.16)$$

$$\text{where } \sigma = \frac{1}{K_e} + \frac{\lambda_K}{2} C_K, \quad K_e = \frac{K_D}{1+\theta}, \quad C_K = \frac{r_K}{r_0}$$

The energy loss due to swirl chamber wall length  $\Delta_L$  is in Eq. 2.17.

$$\Delta_L = \frac{K_D^2}{2C_K} (1 + C_{d,pr} K_D C_K) \left[ 1 - \frac{1}{\left(1 + \theta \frac{C_K}{C_K - 1} \bar{\lambda} \cdot \bar{L}_K\right)^2} \right] \quad (2.17)$$

$$\text{where } \bar{\lambda} = 1.0, \quad \bar{L}_K = \frac{L_K}{D_K}, \quad K_{pr} = K_D C_K = \frac{(1 - \varphi_{pr}) \sqrt{2}}{\varphi_{pr}^{1.5}}, \quad C_{d,pr} = \sqrt{\frac{\varphi_{pr}^3}{2 - \varphi_{pr}}}$$

Finally, energy loss at converging part  $\Delta_{noz}$  is in Eq. 2.18.

$$\Delta_{noz} = \frac{\xi_{noz}}{\varphi_\theta^2} \quad (2.18)$$

In Eq.18, the hydraulic resistance  $\xi_{noz}$  is affected by contraction angle  $\psi$ :  $\xi_{noz} = 0.11$  at  $\psi = 90^\circ$  and  $\xi_{noz} = 0.16$  at  $\psi = 120^\circ$ .

Considering the energy losses mentioned above, the equivalent discharge coefficient  $C_{d,eq}$ , geometric constant  $K_{eq}$ , and injection differential pressure  $\Delta P_{eq}$ .

$$C_{d,eq} = \frac{1}{\sqrt{\left(\frac{1}{\varphi_\theta^2} + \frac{K_{eq}^2}{1 + \varphi_\theta} + \Delta_{sum}\right)}} \quad ; \quad \Delta_{sum} = \Delta_K + \Delta_{in} + \Delta_{noz} + \Delta_L \quad (2.19)$$

$$K_{eq} = \frac{K_D}{1 + \theta \left(1 + \frac{C_K}{C_K - 1} \bar{\lambda} \bar{L}_k\right)} \quad (2.20)$$

$$\Delta P_{eq} = \frac{\Delta P_{ideal}}{\left(\frac{C_{d,eq}}{C_d}\right)^2} \quad (2.21)$$

### 2.1.2 High-pressure chamber

The combustion chamber of the liquid propellant rocket engine operates under high pressure and temperature. In this conditions, behavior of the liquid flow is much different from those at atmospheric conditions [Lefebvre, 1989; Strakey et al., 2001]. Therefore, the high-pressure chamber was used in the experiments to control the conditions surrounding the flow.

The schematic and the photograph of the chamber is shown in Fig. 2.2. The chamber was pressurized by gas nitrogen. Although the endurance pressure of the chamber was designed to 12 MPa, the maximum available working pressure was 6 MPa for safety. Because the maximum working pressure exceeds the critical pressure of the nitrogen (3.39 MPa), the experiment under supercritical condition for the injected flow was available. Since the chamber pressure was increased when the flow was injected and vaporized, the controller automatically reduced and maintained the chamber pressure by sensing the chamber pressure and then opening and closing the exhaust valve. The inner diameter of the chamber was 500 mm and the length was 1,000 mm; total inner volume of the chamber was 200 L. The injector was mounted on the transporting device inside the chamber. This device was able to vertically transverse and rotate under pressurized situations.

Six quartz windows with 80 mm in diameter were located on the chamber for optical access to the flow. Four windows were located around the chamber, and one window port was inclined with 30° angle in order to be used for PDPA measurements. To avoid the deposition of droplets on the window surface, inner surface of the windows were 300 mm apart from the inside wall of the chamber. Air curtain system also was installed to prevent droplets from the windows.

The chamber was originally used for a cold flow water injection test [Kim et al., 2007]. Therefore, it was slightly modified for the experiment of cryogenic fluid injection [Cho et al., 2014]. The K-type thermocouple was mounted to measure the temperature inside the chamber, and the water feeding line was changed to the vacuum-insulated flexible tube. The sealing material of the chamber was changed from PTFE o-ring to Viton o-ring which endures lower temperature. Similar consideration was applied to the valves used for the operation of the chamber.

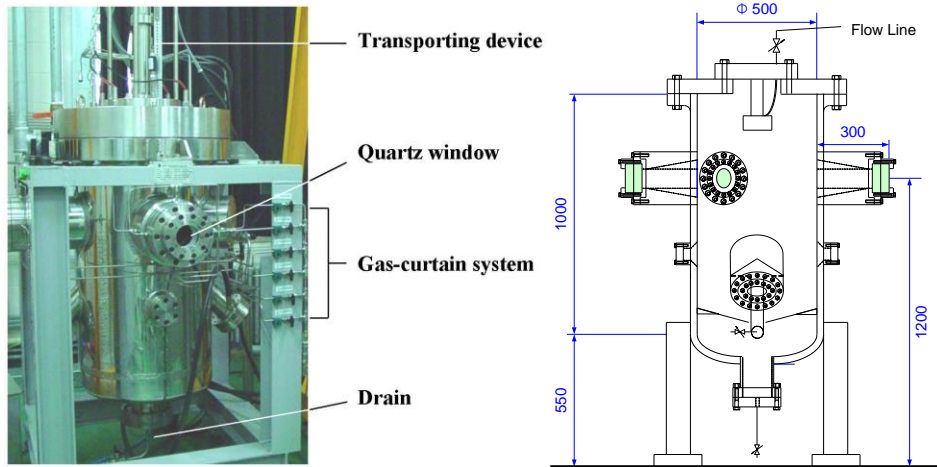


Fig. 2.2 High-pressure chamber

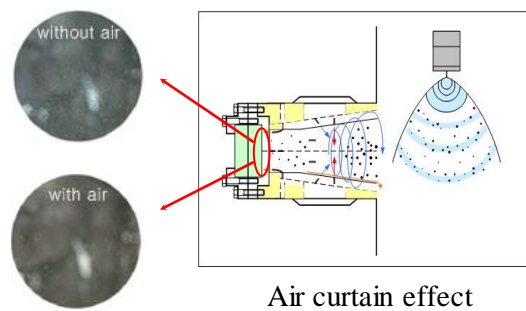


Fig. 2.3 Air curtain system

### 2.1.3 Cryogenic fluid feeding system

The liquid nitrogen was used as working fluid in the experiment. Because of the cryogenic temperature of the fluid, prevention of the heat transfer to the fluid was required. The high pressure condition of the fluid also increased difficulty of the experiment. Therefore, specially designed fluid feeding system was used in this study.

The schematic of the cryogenic fluid feeding system is shown in Fig. 2.4. The cryogenic fluid feeding system contained a run tank, a pressurizing component, and a flow feeding line [Cho et al., 2014]. In the experiment, the run tank was filled with liquid nitrogen and pressurized using nitrogen gas. The cryogenic liquid was fed to the injector via the control of the tank pressure. The run tank and the flow feeding line were vacuum-insulated to minimize the vaporization of the cryogenic liquid caused by heat transfer from outside. The maximum available working pressure of the system was 8 MPa. Sensors, such as thermocouples, pressure transducers, and a turbine flowmeter were installed at the run tank and a flow line to measure the state of the flow inside the system.

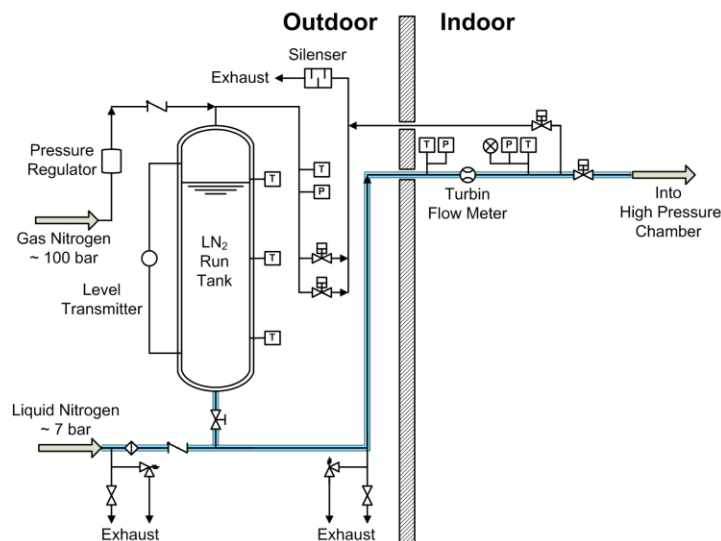


Fig. 2.4 Cryogenic fluid feeding system

## 2.2 Flow Measurement

The purpose of flow measurement is the investigation of fluid state and the flow behavior. Therefore, the properties of the fluid such as pressure, density and temperature are mainly measured first. The characteristics representing the flow behavior, such as the flow image, velocity and instability frequency, can be also measured. Meanwhile, because of the instability which exist in the cryogenic flow, temporal flow measurement technique was also required.

In research of flow under supercritical conditions, harsh condition for the experiment constrained the measurement of flow characteristics. The first related study conducted in DLR [Mayer and Tamura, 1996] conducted qualitative analysis of the single shot flow image. With the development of the investigation technique, the properties of the fluid were measured by non-intrusive laser diagnostics [Chehroudi et al., 2002a; Decker et al., 1998; Mayer et al., 2003; Oschwald and Schik, 1999] and intrusive measurement [Davis and Chehroudi, 2007]. Although these works investigated important flow characteristics, the dynamic characteristics could not be obtained. Therefore, other studies used flow images to conduct temporal analysis of the flow [Teshome et al., 2012; Wegener et al., 2014].

Optically dense region of the flow was measured in this study. High-speed photography with backlight imaging was used, and instability frequency measurement was conducted. These methods enabled both temporal and spatial analysis of the cryogenic swirl flow. To ensure that the injectant is in liquid state, measurement of pressure and temperature was conducted at the injector manifold as shown in Fig. 2.5.

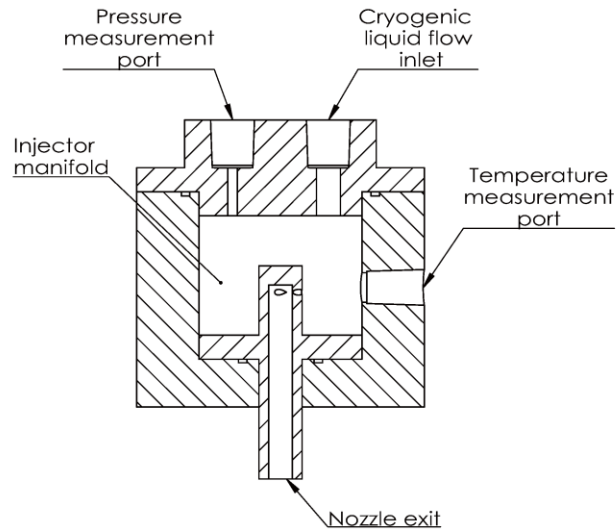


Fig. 2.5 Flow condition measurement inside swirl injector

### 2.2.1 High-speed photography

The characteristics of the flow behavior were investigated via qualitative and quantitative analyses of flow images. In the experiments, the shape of the cryogenic flow was unstable because of its rapid phase change caused by the huge temperature difference between the flow and its surroundings. Therefore, a temporal measurement of the characteristics of the flow was required to study the flow dynamics. Various methods have been employed for the measurement of cryogenic flow, such as shadowgraphy [Chehroudi et al., 2002b; Mayer et al., 2001], Raman scattering [Oschwald and Schik, 1999], and direct measurement of the flow temperature [Davis and Chehroudi, 2007]. Among these methods, Raman scattering and temperature measurement can best determine the quantitative characteristics; however, they are not suitable for measurement of the temporal change of the flow. In addition, the flow image obtained by the shadowgraphy method is sensitive to density variation in the flow field. Because the cryogenic swirl flow, which interacts highly with its surroundings, can affect the density

of the surrounding environment, a distorted flow image can be acquired using shadowgraphy. Considering the abovementioned problems in flow measurement, we chose the use of high-speed photography with backlight imaging for this study.

A schematic of the flow imaging is shown in Fig. 2.6. To obtain a fixed flow image, a Photron Fastcam APX camera was used for high-speed flow imaging. The frame rate of the photography was set at 10,000 frames/sec and the exposure time was  $10 \mu\text{s}$ . A Macro lens (Canon 180 mm Macro) was used to capture the enlarged flow images. A high-power continuous light source (Photron HVC-SL Xenon lamp) was used as backlighting source because the fast phase change of the injectant increases the opacity of the imaging area. Meanwhile, tracing paper was located between the backlight and the flow to flatten the background brightness.

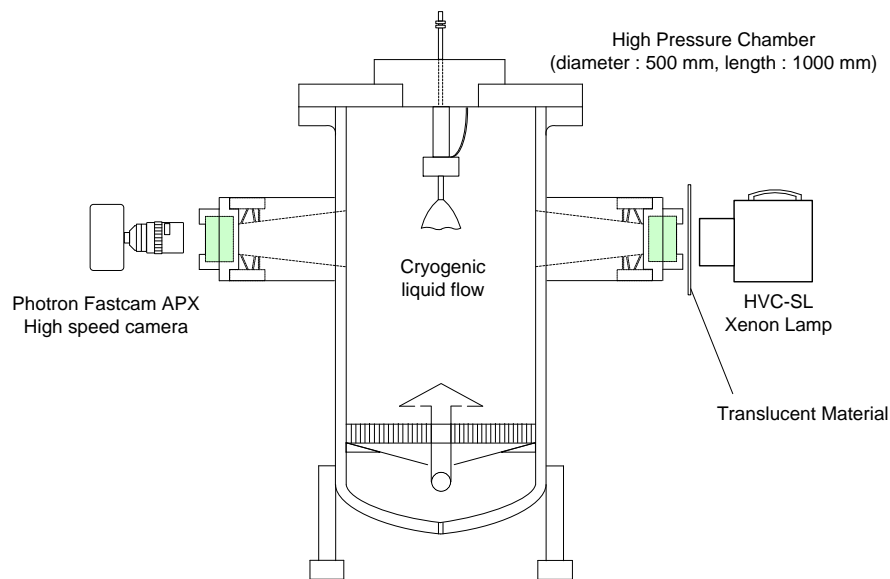


Fig. 2.6 High-speed photography

### 2.2.2 Flow instability frequency measurement

The serious flow instability was observed in the experiment. The oscillation of the flow generated optically dense and sparse regions periodically, and the specific frequency was found. For the quantitative analysis of the instability, flow instability frequency was measured via laser diagnostics method. A schematic of the frequency measurement, which is similar to the flow oscillation measurement system used in a previous study [Im et al., 2009], is shown in Fig. 2.7.

The instability frequency of the flow was measured 5 mm downward from the injector post. A laser line beam (Ar-Ion,  $\lambda_{laser} = 514.5$  nm) was passed through the center of the flow, and the beam intensity was measured via a photodetector with a measurement time of 1 s and a sampling rate of 100 kHz. When the flow region changed due to the instability of the flow surface, the intensity of the laser line beam passing through the flow also changed periodically. From the measured beam intensity, the transmission rate of the laser beam over time was calculated. By means of a spectral analysis, the power spectral density of the transmission rate was calculated and the flow instability frequency was measured.

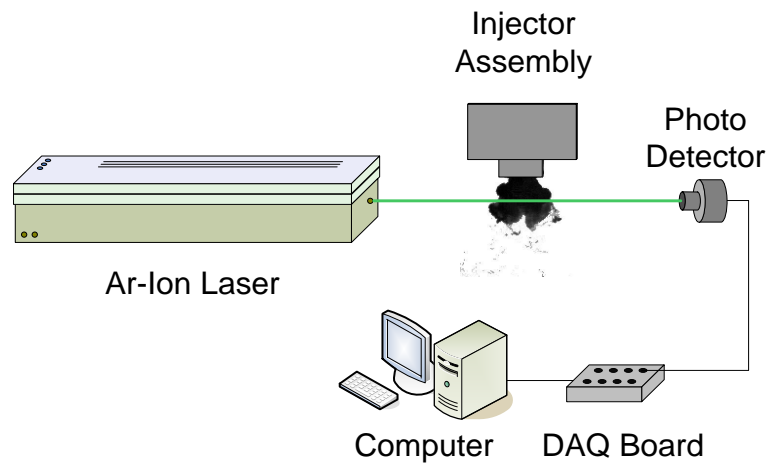


Fig. 2.7 Flow instability frequency measurement using Ar-Ion laser

# **CHAPTER 3**

## **SURFACE INSTABILITY ON CRYOGENIC SWIRL FLOW UNDER SUB- TO SUPERCRITICAL CONDITIONS**

### **3.1 Background and Objectives**

Because recently developed liquid-propellant rocket engines are required to maintain a high level of performance, the engines work under high pressures and temperatures, and a considerable amount of liquid-state propellant is injected into their combustion chambers and burned. As a result, the temperature and pressure in the engine combustion chamber exceed the critical properties of the injected propellant, the phase of which is changed from a liquid to a supercritical fluid through a transcritical process [Schmitt et al., 2012; Yang, 2000]. In this situation, the injected flow is dominated by supercritical fluid characteristics, which include thermophysical properties such as near-zero surface tension and high diffusivity [Oschwald and Schik, 1999]. The conventional model of a liquid flow or spray cannot be adopted [Chehroudi et al., 2002b; Yang, 2000], and the flow characteristics under supercritical conditions must be investigated.

Many studies of cryogenic fluid injection under supercritical conditions have been conducted in Europe and the United States (US). Because the rocket engines developed in these countries mainly used impinging jet injectors (the F-1 engine for the Saturn V) or shear coaxial injectors (the space shuttle main engine and the Vulcain engine for the Arian-5), most studies have concentrated on single or coaxial jet flows and used experimental or numerical methods. Mayer et al. [Mayer and Tamura, 1996; Mayer et al., 2001; Mayer et al., 1998] studied single and coaxial jet flows under non-reacting and reacting conditions and qualitatively observed changes in the flow behavior under various conditions. They found that the atomization process of a cryogenic liquid jet was similar to that of ordinary jets under subcritical conditions, but that the jet showed gas-like

behavior under supercritical conditions [Mayer et al., 2001; Mayer et al., 1998]. During a coaxial reacting flow, it was found that the recirculation zone near the injector tip worked as a flameholder [Mayer and Tamura, 1996]. Chehroudi et al. [Chehroudi, 2010; Chehroudi et al., 2002b; Davis and Chehroudi, 2007] investigated the characteristics of liquid nitrogen jets. These jets behave as a variable-density gas jet under supercritical conditions [Chehroudi et al., 2002b]. The acoustic wave on the coaxial cryogenic jet shortens the dark core length under a subcritical condition [Davis and Chehroudi, 2007], and the sensitivity of the jet core length then affects the combustion instability in a liquid rocket engine [Chehroudi, 2010]. Studies using numerical analyses have also been conducted. The behavior of a non-reacting single jet [Oefelein and Yang, 1998; Zong et al., 2004] and the mixing characteristics of a reactive coaxial jet [Miller et al., 2001; Oefelein and Yang, 1998] were investigated. The results from the analyses were in good agreement with those obtained in experiments.

Instead of jet injectors, swirl-type injectors have been used in many other rocket engines, especially those developed in Russia. A swirl injector creates a hollow cone-shaped spray to distribute the injectant over a larger area than a jet to enhance mixing. It also has a simple structure which is designed to maintain high reliability, and it can be used in various heat engines (i.e., rocket engines, gas turbines and boilers) [Lefebvre, 1989].

Most studies of the characteristics of swirl injectors have focused on the atomization characteristics of the injected liquid flow under subcritical conditions. During a liquid swirl spray, the growth of the surface wave and the nonlinear effect on the unstable liquid sheet determine the breakup length [Clark and Dombrowski, 1972; Dombrowski and Johns, 1963; Han et al., 1997; Kim et al., 2007], and a roll-up vortex structure arising from the liquid sheet surface dominates the atomization process of the spray [Park and Heister, 2006]. The instability of the flow was also studied because it forms the wave on the liquid sheet and causes atomization. Marchione et al. [Marchione et al., 2007] measured the angle of a liquid kerosene swirl spray and found that the angle changes periodically. A fiber-optic method was used to measure the instability frequency of a

water swirl spray at various positions. It was found that two types of instability exist on the liquid sheet: large-amplitude low-frequency instability and small-amplitude high-frequency instability [Musemic et al., 2009]. Other studies investigated the dynamic characteristics of coaxial sprays from spray images, especially the self-pulsation phenomena [Eberhart et al., 2012; Im et al., 2009].

Though the substantial characteristics of a cryogenic fluid injection at supercritical conditions and those of a liquid swirl injection were investigated separately, studies have rarely been conducted on cryogenic swirl flows under supercritical conditions. NASA's Marshall Space Flight Center [Hutt and Cramer, 1996] found different disintegration processes of liquid oxygen swirl flows under subcritical and supercritical conditions during the starting process of a rocket engine combustion test. Zong et al. [Zong and Yang, 2008] conducted a numerical analysis of liquid oxygen swirl flows under supercritical conditions and found that the precessing vortex core (PVC) on the boundary of the central toroidal recirculation zone (CTRZ) and Kelvin-Helmholtz instability dominated the instability of the flow outside the injector. Heo et al. [Heo et al., 2012] also investigated the mixing and instability characteristics of swirl coaxial flows under supercritical conditions. However, more detailed research is still required. The behaviors of swirl flows under sub- to supercritical conditions should be investigated by an experimental approach, and the obtained results have to be compared to previously predicted flow characteristics.

This study investigated the characteristics of cryogenic swirl flows via experiments. Because the flow characteristics are determined by flow instability, and given that this phenomenon appears on the flow surface, images of the flow surface were obtained and analyzed. First, the surface characteristics of the flow were observed and compared to those of a liquid flow under a similar condition in a qualitative manner. Also, changes in the flow surface behavior under sub- to supercritical conditions were investigated. Finally, the instability frequency of the flow was measured and discussed.

## 3.2 Experimental Methods

### 3.2.1 Injector design

The cryogenic swirl flow was injected from an open-type simplex swirl injector mounted inside the chamber. A schematic of the injector is shown in Fig. 3.1, and its geometry is detailed in Table 3.1. The inner diameter of the injector is 5 mm, which is similar to the geometry of the injector used in previous work [Zong and Yang, 2008]. The swirling part of the injector has three tangential holes. The swirl injector's geometrical characteristic parameter  $K$ , which is an important geometric parameter of swirl injectors [Bazarov and Yang, 1998], is 4.4. In the experiment, nitrogen was not injected in a liquid state until the injector was sufficiently cooled. Therefore, a T-type thermocouple and a pressure transducer were used to measure the condition inside the injector manifold and to ensure that the state of the injected flow was liquid.

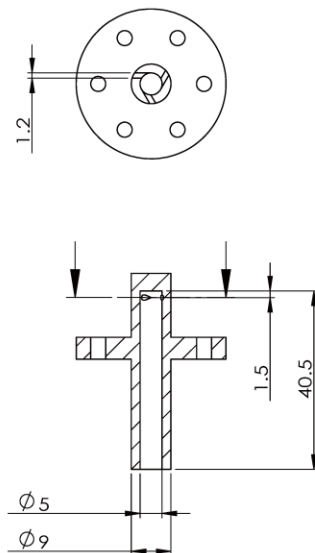


Fig. 3.1 Open-type simplex swirl injector (unit: mm)

Table 3.1 Injector geometry

Injector part	Geometry, mm
Nozzle length, $L_o$	40.5
Nozzle diameter (inner), $d_{o,i}$	5
Nozzle diameter (outer), $d_{o,o}$	9
Tangential inlet diameter, $d_p$	1.2
Number of tangential inlet, $n$	3
Injector geometrical characteristic parameter $K = (d_{o,i} - d_p)d_{o,i}/nd_p^2$	4.4

### 3.2.2 Experimental conditions

The injection differential pressure ( $\Delta P$ ) and ambient pressure ( $P_c$ ) were controlled during the experiment.  $\Delta P$  was maintained at 0.5 MPa and 1 MPa, and the resulting mass flow rates were approximately 50 g/s and 65 g/s, respectively.  $P_c$  was increased to 4 MPa, which is above the critical pressure of nitrogen. The ambient temperature,  $T_c$ , was held at approximately 270 ~ 280 K. As the critical properties change drastically with a slight change of the mixture ratio in gas mixtures [Mayer et al., 2001], nitrogen gas was used as the surrounding gas to maintain the critical properties during the experiment. Under these experimental conditions, the cryogenic liquid was injected into the chamber at sub-, near-, and supercritical pressures. The injection temperature measured at the manifold of the injector was close to the saturation temperature.

Detailed experimental conditions are shown in Fig. 3.2 and Table 3.2. In Fig. 3.2, initial and final condition of the injectant for each experimental case are pointed in Pressure-Temperature diagram of nitrogen, and each points are connected with a solid line. The initial condition point indicates the pressure and temperature condition of the

injectant measured at the injector manifold as mentioned in section 2.2, and it is located at the left side of the figure which means that the nitrogen is in liquid state. In contrast, the final condition point indicates the condition of the high-pressure chamber and located at the right side of the figure.

For the cases that the pressure of the initial condition is above 3.5 MPa, it can be thought that the injected liquid nitrogen might become supercritical fluid in the injection process. In addition, for some experimental cases ( $\Delta P = 1$  MPa,  $P_c \geq 3.4$  MPa), the fast phase change of the injectant disrupted the visualization of the flow, and high-speed photography was not available.

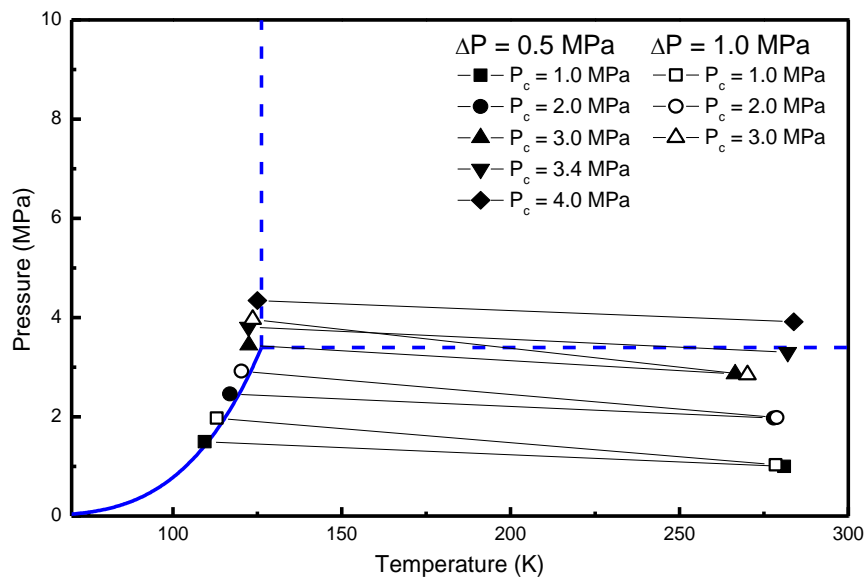


Fig. 3.2 Experimental conditons in Pressure-Temperature diagram of nitrogen

Table 3.2 Experimental conditions

Flow condition	Range
Injection differential pressure (MPa)	0.5/1
Ambient pressure (MPa)	1, 2, 3, 3.4, 4
Injector manifold temperature (K)	105~125
Ambient temperature (K)	280

### 3.2.3 Experimental techniques

The characteristics of the flow surface were investigated via qualitative and quantitative analyses of flow images. Because the cryogenic swirl flow is rapidly vaporized by the temperature difference between the flow and its surroundings, the shape of the flow changes quickly. In this case, high-speed photography with a short exposure time was used to obtain a fixed image to enable a temporal analysis of the flow. The frame rate was 10,000 frames per second, and the exposure time was maintained at 10  $\mu$ s. The imaging area was 28.8 (width)  $\times$  28.8 (height) mm<sup>2</sup>, and the pixel size was 112.5  $\mu$ m. The detailed explanation of this method is in section 2.2.1.

The instability frequency of the flow was measured 5 mm downward from the injector post. This method is similar to the flow oscillation measurement system used in a previous study [Im et al., 2009]. An intensity of the laser line beam measured via a photodetector with a measurement time of 1 s and a sampling rate of 100 kHz. By means of a spectral analysis, the power spectral density of the transmission rate was calculated and the flow instability frequency was measured. The detailed explanation is in section 2.2.2.

## **3.3 Results and Discussion**

### **3.3.1 Characteristics of the cryogenic swirl flow**

Previous studies [Mayer et al., 1998; Oswald and Schik, 1999] noted that cryogenic flows are highly affected by vaporization. Therefore, it is necessary to determine the important characteristics of a cryogenic flow as compared to a common liquid flow before an investigation of a cryogenic flow under sub- to supercritical conditions. To find the unique characteristics of the cryogenic flow studied here, a liquid nitrogen flow and water spray injected from the same injector were compared. To ensure a proper comparison, the experimental conditions were equivalent for each flow. The injection differential pressure was set to 0.5 MPa, and the ambient pressure was set to 2 MPa in order to keep the injectant in a liquid state.

Images of the cryogenic swirl flow and the water swirl spray are shown in Fig. 3.3(a) and Fig. 3.3(b), respectively. The atomization process of the conventional liquid swirl spray can be explained by Dombrowski's hypothesis [Clark and Dombrowski, 1972; Dombrowski and Johns, 1963]. During the atomization process, in which the gas surrounding the liquid sheet is stationary and the vaporization effect can be ignored, a small perturbation is imposed on the liquid sheet and the wave travels along the flow. In the liquid sheet, the amplitude of the surface wave increases to a certain value [Dombrowski and Johns, 1963], and two waves with different modes (sinusoidal and symmetric) are superimposed on the sheet. The thickness of the sheet becomes zero at a certain position where breakup occurs [Clark and Dombrowski, 1972]. Meanwhile, owing to Kelvin-Helmholtz instability, a vortex ring structure develops on the surface and affects the breakup process, ligaments, and droplet diameter [Park and Heister, 2006]. This process is shown in Fig. 3.3(b).

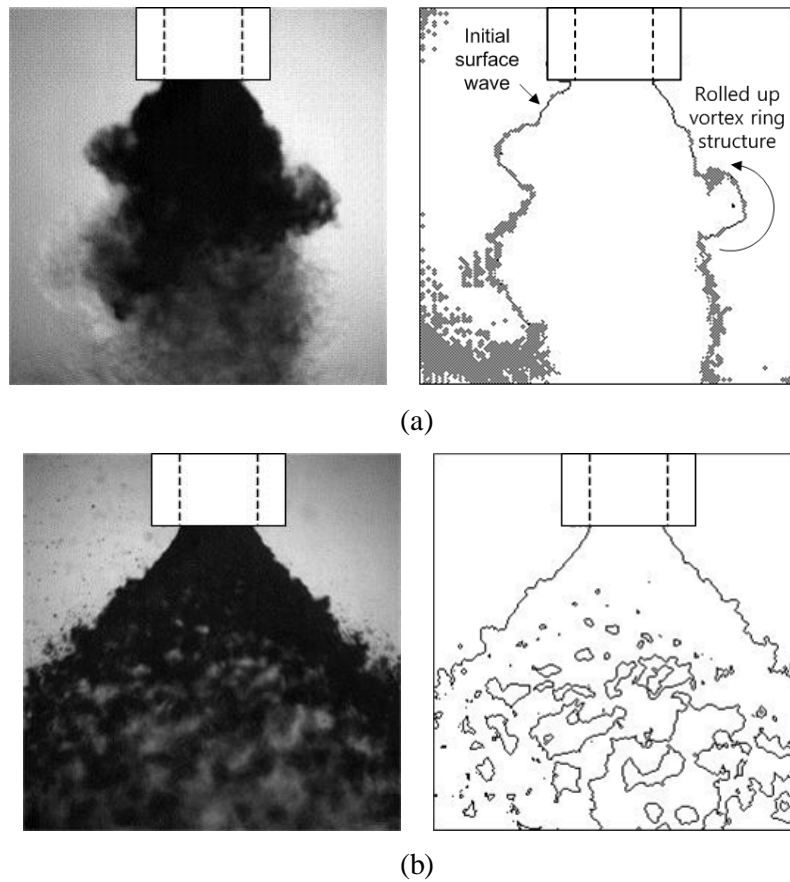


Fig. 3.3 Instantaneous swirl flow image at  $\Delta P = 1$  MPa,  $P_c = 1$  MPa for (a) cryogenic swirl flow and (b) water swirl flow; (left) original image and (right) flow boundary

In the cryogenic swirl flow studied here, however, an unstable helical wave structure was found on the flow surface, and a liquid lump which became detached from the flow was observed. These characteristics of the cryogenic swirl flow are rather similar to that of a gas swirl jet [Syred, 2006], a cryogenic swirl flow under a supercritical condition [Zong and Yang, 2008], and a swirl liquid jet with a precessing flow structure inside the flow [Liang and Maxworthy, 2005]. From these findings, it can be hypothesized that the PVC in the CTRZ dominates the instability of the cryogenic swirl flow; thus, the

assumption of the stationary surrounding gas condition, following Dombrowski's hypothesis, is no longer appropriate. According to PVC instability, a helical vortex structure is created in the flow, and the injected flow causes the recirculation of the surrounding gas, after which gas is entrained on the flow surface. Finally, the wavy structure on the surface is rolled up [Han et al., 1997]. In this flow, droplets from the atomization process were not observed, and the amplitude of the wave structure and the roll-up vortex was significantly larger than that of the water flow. These differences indicate a serious phase change in the flow.

As mentioned earlier, small droplets were not observed during the cryogenic liquid flow. One reason for this absence is the considerable temperature difference between the flow and the surrounding area, which causes the fast vaporization of the small flow structure or the detached fluid, making flow visualization impossible. Another reason may be the brightness of the backlight, which was high enough to saturate the image sensor and prevent the visualization of the small fluid structure. Instead of droplets, liquid lumps that disintegrated from the flow were found. They were approximately 1 mm in size, similar to the scale of the surface structure found in the water flow.

The size of the wave and the roll-up vortex structure at the flow surface was larger for a cryogenic flow than for the water flow due to the differences in the properties of liquid nitrogen and water. Because its viscosity and surface tension are less than 10% of those of water [Linstrom and Mallard], the inertial force affects the cryogenic flow more than the viscous force or surface tension force. Earlier studies [Dombrowski and Johns, 1963; Senecal et al., 1999] implied that the growth rate and wave number would be smaller for a flow with lower viscosity. The result obtained from this study supports such a prediction.

### **3.3.2 Effect of the ambient pressure on the characteristics on a cryogenic swirl flow surface**

The ambient pressure would affect the behavior of liquid swirl spray [Kenny et al., 2009; Kim et al., 2007; Lefebvre, 1989], and the behavior of the cryogenic jet flow would change significantly when the ambient pressure changes from sub- to supercritical conditions for the injectant [Chehroudi et al., 2002b; Hutt and Cramer, 1996; Mayer et al., 1998]. Therefore, the effect of the ambient pressure on the cryogenic swirl flow was studied. The static and dynamic characteristics of the flow were investigated via a flow image analysis.

Instantaneous and averaged flow images acquired via high-speed photography with backlight imaging under various ambient pressure conditions are shown in Fig. 3.4. Representative flow images under subcritical and supercritical conditions are compared in Fig. 3.5. In the flow images, the dark region represents the flow in a liquid state. The downstream flow after a breakup or phase change can be distinguished from the surroundings. In each flow region, the flow characteristics of the behavior of the flow at the boundary, the spray angle, and other characteristics of the wave structure on the flow surface were investigated. Spatial and temporal analyses were conducted by processing the flow image. Matlab™ was used for the processing of the flow image and the analysis. During the processing steps, the flow boundaries were detected using the graythresh function which selects an appropriate threshold value based on Otsu's method [Teshome et al., 2012], and by creating a binary image from the original flow image.

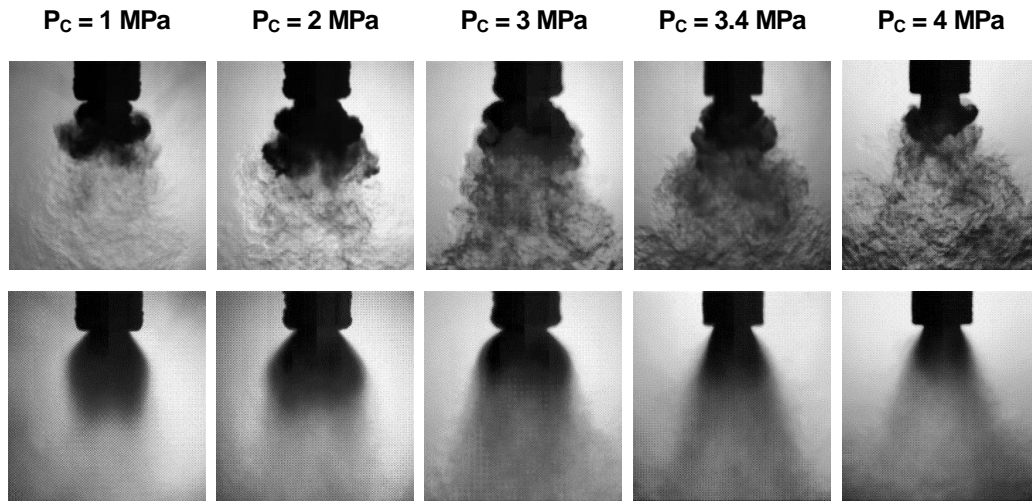


Fig. 3.4 Representative swirl flow images under various ambient pressure conditions for instantaneous image (top row) and averaged image (bottom row) at  $\Delta P = 0.5 \text{ MPa}$

The shape of a common liquid swirl flow is a hollow cone. In a liquid flow region, the flow is slightly contracted along the flow's axial direction under subcritical conditions. When comparing liquid state flows near the injector post, the flow area was larger for a flow in a subcritical condition than it was for a flow in a supercritical condition. Under supercritical conditions, a roll-up vortex structure was found on the flow surface near the injector post, whereas a wave structure was not found. The shape of the injected flow is different from flow under subcritical conditions, for which the surface structure is initially in the shape of a sinusoidal wave and changes to a roll-up vortex, as shown in Fig. 3.3(a) and Fig. 3.5(a), respectively.

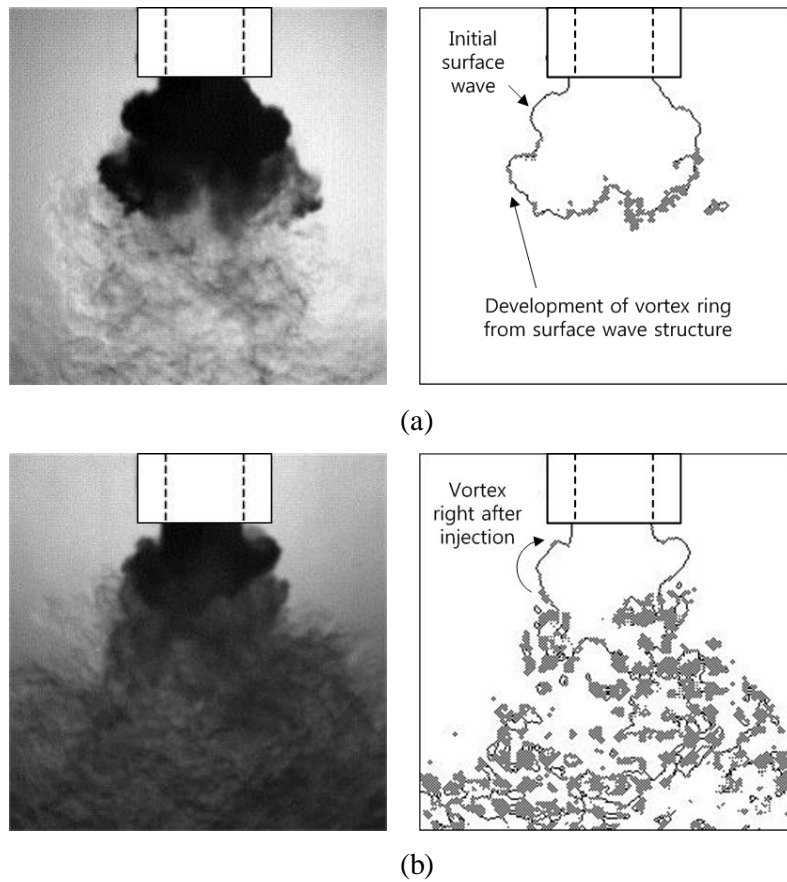


Fig. 3.5 Instantaneous swirl flow image at  $\Delta P = 0.5$  MPa for  
 (a)  $P_c = 2$  MPa (subcritical conditions) and (b)  $P_c = 4$  MPa (supercritical conditions);  
 (left) original image and (right) flow boundary

For a quantitative analysis of the flow in a liquid state, the spray angle was measured from the flow image. The spray angle, which represents the distribution and mixing characteristics of the flow, was measured from the averaged flow image under each condition in the second row of Fig. 3.4. These results are shown in Fig. 3.6. Due to the difficulty involved in boundary detection after a breakup or phase change, the spray angle

was measured near the injector post, where the injectant remains in a liquid state and where the flow is distinguishable from the surroundings. In Fig. 3.6, the measured spray angle under each condition is compared to the results of an empirical equation suggested in a previous work [Fu et al., 2012] regarding the geometric characteristics of open-type injectors and the Reynolds number at a tangential inlet. This research used water as the working fluid, and it was conducted under atmospheric pressure conditions. Due to the similarity of the injector geometry between present study and previous work, it was expected that the experimental results would be similar in terms of the tendencies whereas the values of the results would differ because of different flow conditions. However, the spray angle suggested in the previous work was different from the measured spray angle both qualitatively and quantitatively. While the spray angle remains almost constant in theory and in the experiments [Fu et al., 2012; Kenny et al., 2009; Kim et al., 2007; Lefebvre, 1989] for a common liquid flow, the surface of the cryogenic flow is unstable and the measured angle can increase with the ambient pressure [Kim et al., 2007]. In addition, the larger length-to-diameter ratio of the injector in this experiment caused an increase in the amount of momentum loss inside the injector and a decrease in the measured spray angle as compared to the predicted value. Meanwhile, the angle was decreased sharply when the surroundings were changed from subcritical to supercritical conditions, as in an earlier work [Hutt and Cramer, 1996]. This may have been caused by the drastic change of the physical properties of the injectant, especially the viscosity and the surface tension. However, these properties do not affect the spray angle of the liquid swirl flow under subcritical conditions [Lefebvre, 1989]. In this case, the effects of these properties under supercritical conditions should be considered. While the spray angle of the swirl flow can be denoted as  $\alpha = 2 \tan^{-1} (w/u)$ , where  $w$  is the tangential velocity and  $u$  is the axial velocity of the flow, a decrease of the azimuthal velocity causes a decrease in the spray angle. Under supercritical conditions, the surface tension is diminished and the dissipation of the velocity from the liquid surface to the air core occurs more intensely for the azimuthal component than it does for the axial component [Zong and Yang, 2008], which ultimately causes a significant decrease in the spray angle.

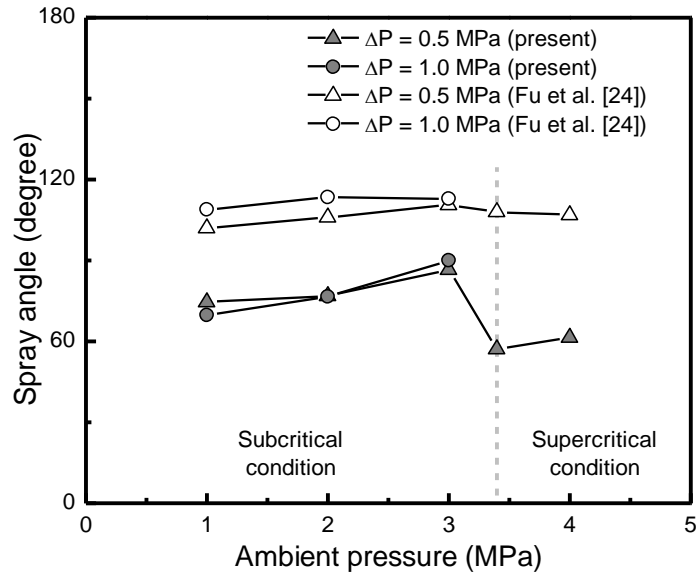
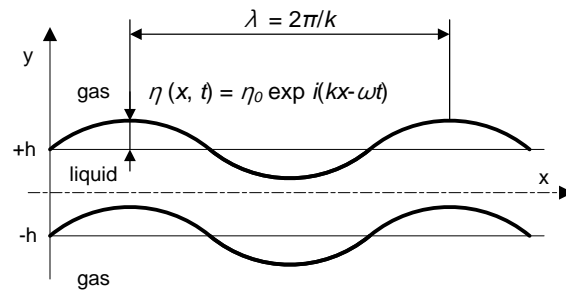


Fig. 3.6 Spray angle of cryogenic swirl flow

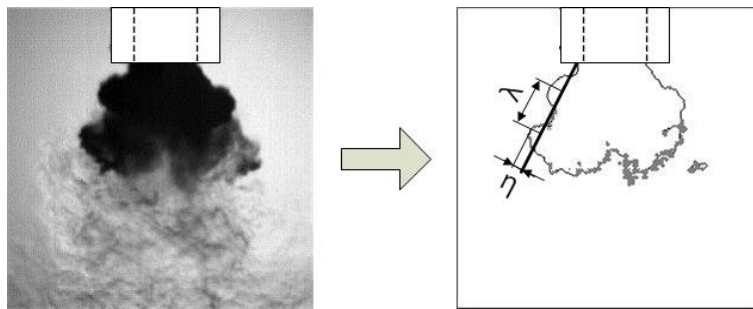
After a breakup or phase change, the injected flow remained downstream and could be clearly distinguished from the surroundings, as shown in Fig. 3.5. Under subcritical conditions, though the state of the injected flow changed from liquid to gas, the temperature difference between the downstream area and the surroundings remained large and tiny flow structures were observed, indicating the existence of a density gradient. The downstream flow was contracted and moved downward, and vortices were found at the boundary of the flow region. This behavior is similar to that of droplets created by the atomization of a conical liquid sheet, meaning that the decrease in the azimuthal velocity was larger than the decrease in the axial velocity in the downstream flow. Under supercritical conditions, in contrast, the downstream flow had higher visible opacity and its spreading angle was maintained. In this condition, the state of the injectant changed from a gas to a supercritical fluid and its density changed moderately. Because the opacity of a fluid is related to its density, the opacity of the downstream flow changes less.

Moreover, the effect of the momentum loss on the injected flow will be less than that on the flow under subcritical conditions, where the density changes significantly during the phase change from liquid to gas.

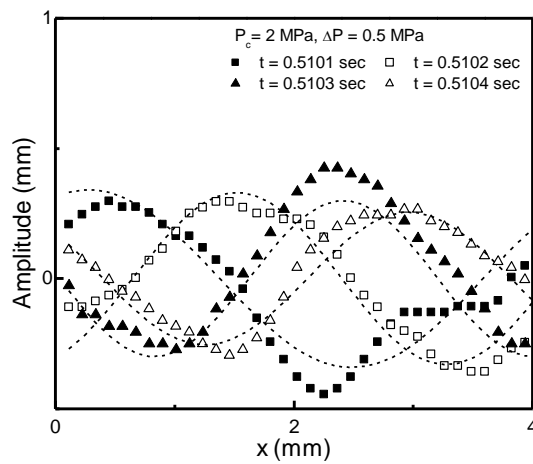
In a cryogenic swirl flow, a wave is imposed on the flow surface and creates a wavy structure periodically, which causes instability of the flow, as shown in Fig. 3.7(a). Therefore, the characteristics of the wave on the flow surface were investigated from an instantaneous flow boundary image in order to determine the characteristics of the instability. The flow surface was assumed to have a sinusoidal wave shape and was assumed to be fitted to a sinusoidal wave, the form which is as follows:  $\eta(x, t) = \eta_0 \exp i(kx - \omega t)$ , where  $x$  is the distance from the injector post along the liquid sheet,  $t$  is the time,  $\eta_0$  is the amplitude of the wave,  $k$  is the wave number, and  $\omega$  is the growth rate. The wavelength  $\lambda$  was calculated from  $k$  via  $\lambda = 2\pi/k$ . The characteristics of the surface wave (i.e., wave amplitude, wavelength) were calculated via the curve fitting function “fit” in Matlab™. Due to PVC instability, a wavy vortex structure was generated on the flow surface, and it changed to a roll-up vortex due to the entrainment of the surrounding gas on the flow surface. Therefore, the growth rate could not be measured. The propagation velocity of the wave,  $v$ , was calculated by measuring the displacement of the flow structure along the liquid sheet. The detailed process of the flow image analysis is shown in Figs. 3.7(b) and (c).



(a)



(b)



(c)

Fig. 3.7 Image analysis of cryogenic swirl flow for  
 (a) sinuous wave imposed on plane liquid sheet, (b) flow boundary detection and  
 (c) sine curve fitting of flow surface

The wave amplitude did not change significantly, independent of the ambient pressure, as shown in Fig. 3.8. As mentioned earlier, the amplitude of the wave was not maintained. In the flow image analysis, a roll-up vortex structure may have existed in the flow boundary and measurement error may have occurred. In contrast to the wave amplitude, the wavelength and propagation velocity both changed along the ambient pressure. As shown in Fig. 3.9, the wavelength shifted from short to long. This shift occurred under transient conditions in which the pressure of the injectant or the surroundings was close to the critical pressure. The wave propagation velocity decreased with an increase in the ambient pressure, as shown in Fig. 3.10. It is clear that the characteristics of the liquid swirl flow changed with the ambient pressure [Kim et al., 2007]. Increasing the ambient pressure prevents the penetration of the injected flow and causes a loss of the kinetic energy of the flow, after which the flow momentum decreases. In the transient region, however, the propagation velocity drastically increased.

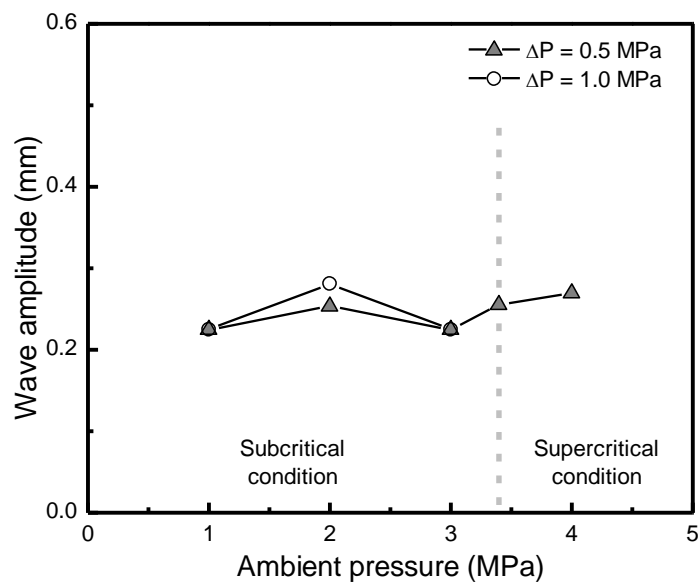


Fig. 3.8 Wave amplitude on surface of cryogenic swirl flow

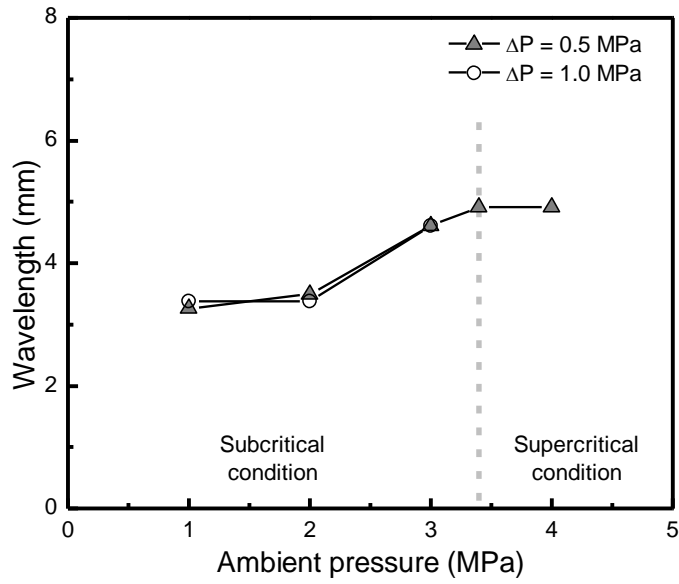


Fig. 3.9 Wavelength on surface of cryogenic swirl flow

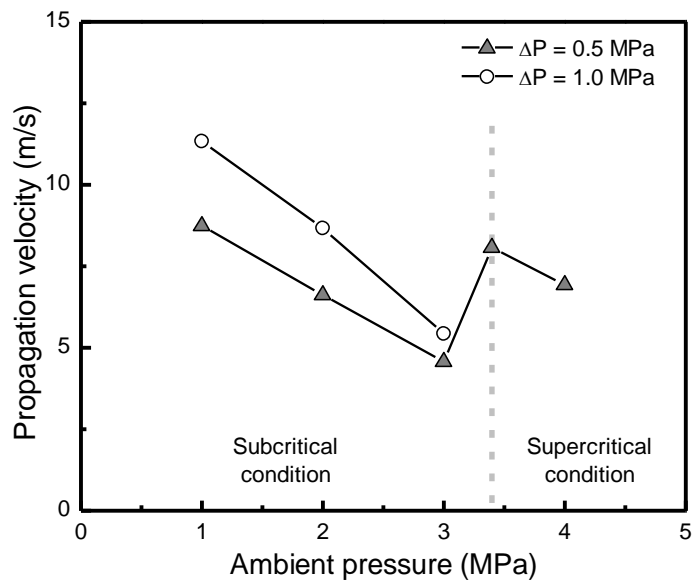


Fig. 3.10 Propagation velocity of surface wave in axial direction

Under supercritical conditions, the wavelength and propagation velocity of the flow surface sharply increased. These phenomena can be explained via the characteristics of a supercritical fluid. Due to the near-zero surface tension, the structure of the flow surface can be scattered easily. Here, only one roll-up vortex, rather than a sinuous wave, was found on the flow surface, as shown in Fig. 3.5(b). The value of the measured wavelength then reaches the measurable range, at around 5 mm. The increased velocity was caused by measurement error at  $P_c = 3$  MPa. Under this condition, the pressure of the injectant reaches the critical pressure, but the surroundings remain at a subcritical pressure. This pressure difference would cause disordered flow behavior and disrupt the reliable measurement of the wave characteristics. In this transient region, both a propagating wave and a rolled-up vortex structure exist at the same position, thereby becoming superimposed. At the very least, the superposition of the surface structures causes an underestimation of the velocity.

### 3.3.3 Instability analysis of a cryogenic swirl flow surface

An instability analysis of a cryogenic swirl flow was conducted via instability frequency measurements. The transmission rate of a laser line beam passing through the flow area was used to measure changes in the flow. The transmission rate is  $I/I_0$ , where  $I_0$  is the original laser beam intensity and  $I$  is the intensity of the beam which passes through the flow. When the liquid flow area increases, the laser beam is attenuated and the transmission rate is decreased. Therefore, when flow instability generates oscillation of the flow interface and finally the flow area, the transmission rate also oscillates and the instability frequency can be obtained by a spectral analysis.

If a certain frequency is found via spectral analysis of the transmission rate, it can be deduced that the structure on the flow surface is created periodically in the flow. Thus, the measured frequency can be defined as the instability frequency of the flow. The transmission rate was measured by a photodetector, and the data acquisition sampling rate of the detector was 100 kHz such that the frequency of the transmission rate oscillation

less than 50 kHz could be measured by a spectral analysis. As the PVC phenomenon generates an unstable flow structure, the frequency of the flow instability is regarded as the PVC instability frequency.

The power spectral density of the transmission rate was calculated via spectral analysis. The results for each condition are shown in Fig. 3.11. The effects of the ambient pressure and the injection differential pressure on the instability frequency are shown in Fig. 3.12. The unexpectedly large value of the spectral density shown in the low-frequency range ( $f < 100$  Hz) was considered as noise. With this data reduction, the peak frequency was located between 1 and 4 kHz, which corresponds to the PVC instability frequency [Syred, 2006]. The value of the measured frequency is comparable to that of the measured frequency of weak instability on a liquid swirl flow (2~3 kHz, at atmospheric pressure) [Museum et al., 2009], and the numerically calculated instability frequency of the liquid oxygen swirl flow under supercritical conditions (1.04 kHz, at 10 MPa) [Zong and Yang, 2008]. The instability frequency decreased with an increase in the ambient pressure and a decrease in the injection differential pressure. When the ambient pressure increases, the penetration of the flow into the surrounding area is obstructed and the axial flow velocity is decreased. A decrease in the injection differential pressure causes a decrease in the mass flow rate, finally having a similar effect on the flow. Consequently, the flow structure will pass the measurement point less frequently and the measured instability frequency will decrease.

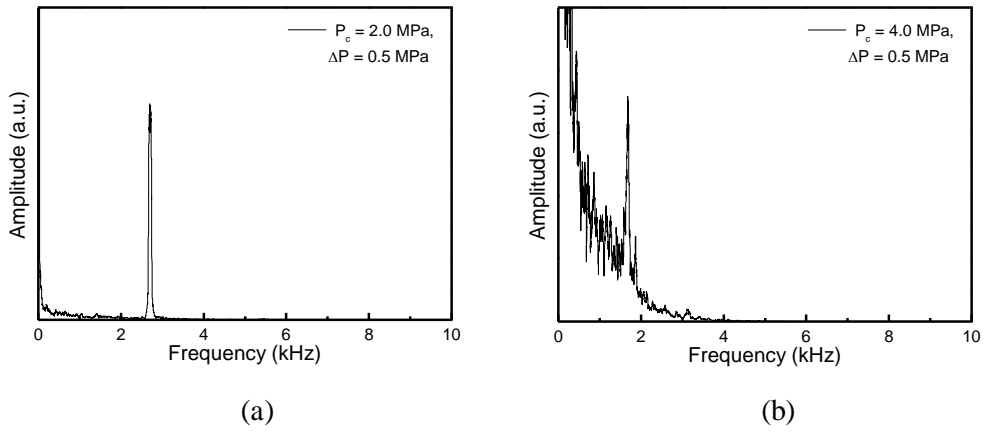


Fig. 3.11 Results from spectral analysis of transmission rate at  $\Delta P = 0.5$  MPa under various ambient pressure conditions: (a)  $P_c = 2$  MPa, (b)  $P_c = 4$  MPa

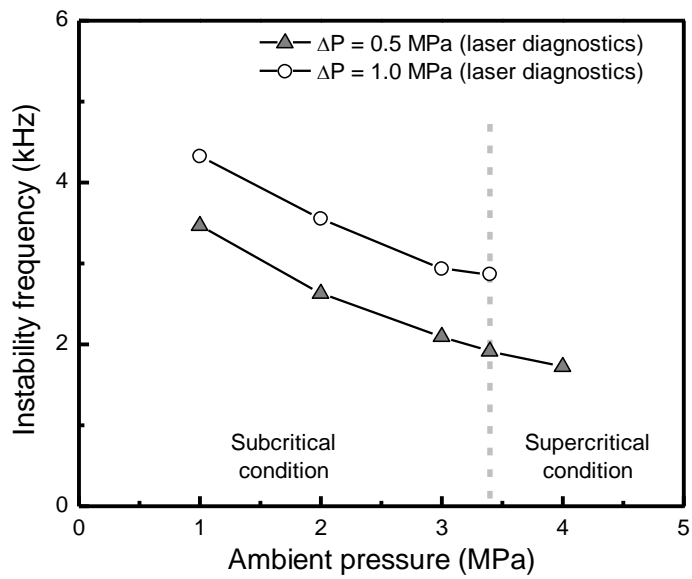


Fig. 3.12 Instability frequency of cryogenic swirl flow

## **Chapter 4**

# **DYNAMIC CHARACTERISTICS OF A CRYOGENIC SWIRL FLOW UNDER SUPERCRITICAL CONDITIONS**

### **4.1 Background and Objectives**

Many type of injectors are used in propulsion or power supply combustion engines for injection and mixing the fuel and oxidizer. In liquid propellant rocket engines, three types of injectors are generally used: impinging type, shear coaxial type and swirl coaxial type. Among these, swirl type injectors have several advantages in the distribution and mixing of injectants. Accordingly, this type of injector has been studied [Bazarov and Yang, 1998; Khavkin, 2004] and used in many of the rocket engines developed in Russia [Lefebvre, 1989].

Serious combustion instability can be induced in the combustion chamber of a liquid rocket engine because of its operational conditions of high pressure and temperature. Combustion instability is caused by the coupling of acoustic pressure oscillation and unsteady heat release [Culick and Yang, 1995]. This phenomenon drastically increases the amplitude of oscillation and ultimately leads to serious engine failure. Particularly in the most recently developed rocket engines, the high energy density condition inside the combustion chamber can provide a large amount of energy leading to instability. Therefore, the reduction of instability is extremely important in the development of liquid propellant rocket engines.

Various factors affect combustion instability: chamber geometry, instability from the propellant feed line, flow instability, etc. [Culick and Yang, 1995]. Among these, the most significant factor is the geometry of the combustion chamber, which determines the acoustic characteristics of combustion instability. Flow instability can affect the distribution and mixing of the injected propellant. This phenomenon can be related to the

disintegration and atomization characteristics of the liquid flow. Thus, numerous studies have been conducted on flow instability in swirl injectors [Cooper and Yule, 2001; Donjat et al., 2003; Im et al., 2009; Kenny et al., 2009; Kim et al., 2009; Landwehr et al., 2006; Marchione et al., 2007; Musemic et al., 2009]. In a simplex swirl injector flow, instability in the low-frequency ( $\sim 10^2$  Hz) and high-frequency ( $\sim 10^3$  Hz) regions were measured simultaneously [Landwehr et al., 2006; Musemic et al., 2009], and the similar instability frequencies caused by spray angle oscillation were observed [Marchione et al., 2007]. In addition, several studies have suggested that the internal flow instability of an injector causes instability in the external flow [Cooper and Yule, 2001; Donjat et al., 2003; Kenny et al., 2009]. In gas-liquid coaxial injector flow, the self-pulsation frequency has been related to the natural frequency of the liquid-only flow [Im et al., 2009].

The dynamic characteristics of cryogenic flow under supercritical conditions have also been investigated. These studies indicated that two kinds of instability in cryogenic swirl flow under supercritical conditions exist: a precessing vortex core (PVC) in the central toroidal recirculation zone (CTRZ) and Kelvin-Helmholtz instability caused by shear between the flow and its surroundings [Zong and Yang, 2008]. These instability characteristics are similar to those of liquid swirl flow injected into liquid surroundings [Gallaire et al., 2004; Liang and Maxworthy, 2005]. The response of the flow to external excitation was also experimentally [Teshome et al., 2012; Wegener et al., 2014] and numerically [Schmitt et al., 2012] investigated. These efforts revealed that the characteristics of flow instability can affect the response of the flow to external excitation.

For in-depth study of flow instability, mode decomposition methods have been recently applied to the flow field dataset. In particular, the Proper Orthogonal Decomposition (POD) method has been used to investigate the dynamics in various types of flows to obtain coherent flow structures and to determine their roles in flow behavior [Arienti and Soteriou, 2009; Berkooz et al., 1993; Eberhart et al., 2012; Markovich et al., 2014; Meyer et al., 2007; Semeraro et al., 2012; Teshome et al., 2012; Wegener et al., 2014; Zong and Yang, 2008]. Although most of these studies used velocity data from the flow field, some of them used flow images [Arienti and Soteriou, 2009; Eberhart et al.,

2012; Teshome et al., 2012; Wegener et al., 2014]. The POD method has already been adopted in investigations of the external behavior of swirl flow under subcritical conditions [Eberhart et al., 2012], jet flow under supercritical conditions [Teshome et al., 2012; Wegener et al., 2014], and the internal flow of the swirl injector under supercritical conditions [Zong and Yang, 2008]. Therefore, it is reasonable that this method be used in a study on swirl flow instability under supercritical conditions.

The main purpose of this study is experimental investigation of the instability characteristics of a cryogenic swirl flow. The ambient pressure was changed as the flow was injected into ambient gas under subcritical to supercritical conditions. The coherent structures of the flow were deduced by analysis of the flow image using the POD method. The spatial and temporal characteristics of the flow and its instability were determined to reveal the instability mechanism that dominated flow behavior.

## **4.2 Experimental Methods**

### **4.2.1 Injector design**

A simplex swirl type injector was mounted inside the chamber to create a cryogenic swirl flow. The injector was a closed-type swirl injector, creating a single hollow-cone-shaped flow. Its geometry was similar to the oxidizer part of the main injector used in an RD-0110 liquid propellant rocket engine [Rubinsky, 1995]. The detailed geometry of the injector is shown in Fig. 4.1 and Table 4.1. Because the inner diameter of the high-pressure chamber was much larger than that of the injector  $D_{o,i}$ , the confinement effect of the chamber wall to the flow was negligible. The temperature and the pressure of the fluid were measured in the vicinity of the tangential inlet of the injector to ensure that the flow was injected in the liquid state.

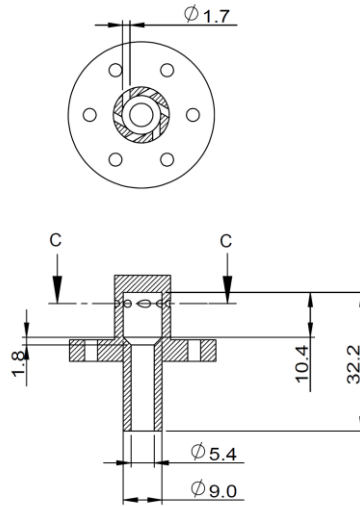


Fig. 4.1 Schematic of the simplex swirl injector (unit: mm)

Table 4.1 Injector geometry

Injector part	Geometry, mm
Swirl arm, $R$	3.5
Swirl chamber diameter (inner), $D_s$	9
Nozzle diameter (inner), $d_{o,i}$	5.4
Nozzle diameter (outer), $d_{o,o}$	9
Tangential inlet diameter, $d_p$	1.7
Number of tangential inlets, $n$	6
Injector geometrical characteristic parameter $K = 2Rd_{o,i}/nd_p^2$	2.2

#### 4.2.2 Experimental conditions

The detailed experimental conditions in this study are shown in Fig. 4.2 and Table 4.2. In Fig. 4.2, as noted in section 3.2.2, initial and final condition of the injectant for each experimental case are pointed and connected with a solid line in Pressure-Temperature diagram of nitrogen. The initial condition point represents the injectant condition at the injector manifold while the final condition point shows the condition of the surrounding nitrogen inside the high-pressure chamber. The injection differential pressure was maintained at 0.5 MPa, which is similar to the actual injection pressure of the oxidizer propellant in an RD-0110 engine [Rubinsky, 1995]. The ambient pressure of the injected flow was increased to 5 MPa, which exceeds the critical pressure of the working fluid. As a result, the liquid flow was injected into the surrounding environment under subcritical to supercritical pressure conditions. The ambient temperature of the flow was maintained around 280 K.

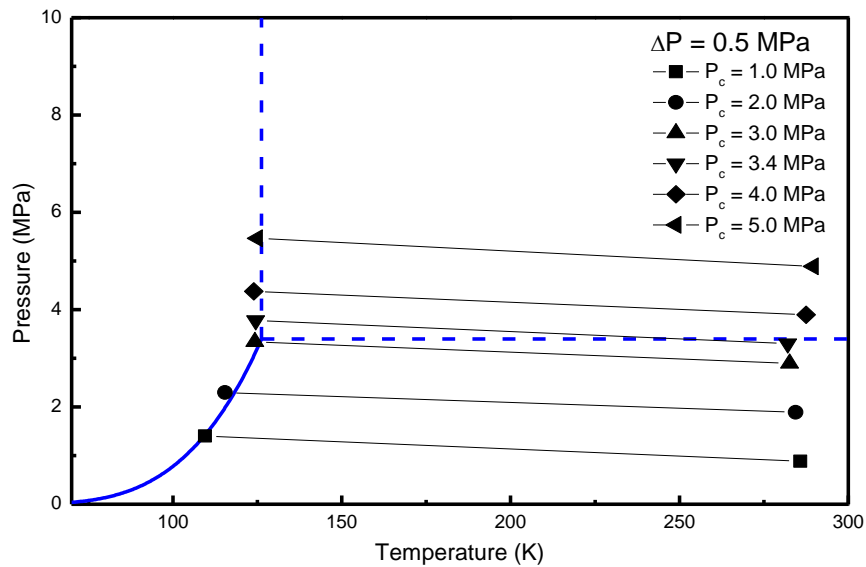


Fig. 4.2 Experimental conditions in Pressure-Temperature diagram of nitrogen

Table 4.2 Experimental conditions

Flow condition	Range
Injection differential pressure (MPa)	0.5
Ambient pressure (MPa)	1.0 – 5.0
Injector manifold temperature (K)	105 – 125
Ambient temperature (K)	280

### 4.2.3 Experimental techniques

The shape of the cryogenic flow was unstable because of its rapid phase change caused by the huge temperature difference between the flow and its surroundings. Therefore, a temporal measurement of the characteristics of the flow was required to study the flow dynamics. In this study, we chose the use of high-speed photography with backlight imaging technique. The whole imaging area was  $42.7$  (width)  $\times$   $21.3$  (height)  $\text{mm}^2$ . The length of each pixel was  $83.3 \mu\text{m}$ . The detailed explanation of this method is in section 2.2.1. The instability frequency of the flow was calculated from the POD analysis. For the validation of the result obtained from POD analysis, the flow frequency was measured with laser diagnostics which is shown in section 2.2.2.

### 4.2.4 Proper Orthogonal Decomposition

The POD method is an application of Principal Component Analysis, which has been used in stochastic analysis of datasets to analyze flow fields. The main purpose of the mode decomposition method is to determine modes from a set of flow field snapshots. These modes are spatially orthogonal to each other, and their coherent structures represent the main characteristics of the flow field [Arienti and Soteriou, 2009; Berkooz

et al., 1993; Meyer et al., 2007].

This section contains a brief explanation of the POD method. The detailed principle and process of POD analysis can be found in Appendix. First, each snapshot of the flow field can be reconstructed by linear summation of the modes. This can be represented as follows:

$$V = [v_1 \quad v_2 \quad \cdots \quad v_{N-1} \quad v_N] \quad (4.1)$$

$$v_n = \sum_{i=1}^N a_{i,n} \phi_i \quad (4.2)$$

In the above equations,  $V$  is a set of flow field snapshots  $v_n$ ,  $\phi_i$  is an  $i$ th spatial POD mode, and  $a_{i,n}$  is a time coefficient related to snapshot  $v_n$  and mode  $\phi_i$ .

Each mode has its own eigenvalue, which can be deduced from the POD mode extraction process.

$$Z = V^*V \quad (4.3)$$

$$Z\phi_i = \lambda_i\phi_i \quad (4.4)$$

$Z$  is the covariance matrix of  $V$ . Symbol  $*$  means conjugate transpose of matrix.  $\lambda_i$  is an eigenvalue of the mode  $\phi_i$  and can be treated as the relative energy of the mode. It is well known that a mode with large eigenvalue is strongly related to  $V$  and contains important information about the flow characteristics. If  $v_n$  contains velocity data in the flow field, then the mode eigenvalue is proportional to the square of the velocity components in the mode. In this case, if the density is constant for the entire flow field, the mode eigenvalue can be directly related to the kinetic energy of the flow.

Although the POD method deduces spatially orthogonal modes, additional analysis is required to determine instability characteristics. Spectral analysis of the time coefficient  $a_i$  can be conducted to determine the instability frequency of the mode.

To apply the POD method to flow image analysis, Matlab™ was used in the image processing. Although velocity field information is mainly used in POD [Berkooz et al., 1993; Meyer et al., 2007; Semeraro et al., 2012], flow image information also can be adopted in the analysis to determine the instability characteristics of the flow [Arienti and Soteriou, 2009; Eberhart et al., 2012]. Moreover, the flow image can be related the distribution of the flow, and the oscillation of the flow distribution is highly dependent on flow instability. Consequently, it is possible to determine the important characteristics of flow instability with POD analysis of the flow image set.

In this study, 4,000 images were used for the POD analysis of each experimental condition. The analysis area for the flow images was 27 (width)  $\times$  10.8 (height) mm<sup>2</sup>. The characteristics of the flow for different positions were investigated by selecting an analysis area with  $y/D_{o,i} = 0 \sim 2$  (upstream region) and  $y/D_{o,i} = 1 \sim 3$  (downstream region) where  $y$  is the axis along the flow propagation starting from the injector post. The analysis area is shown in Fig. 4.3.

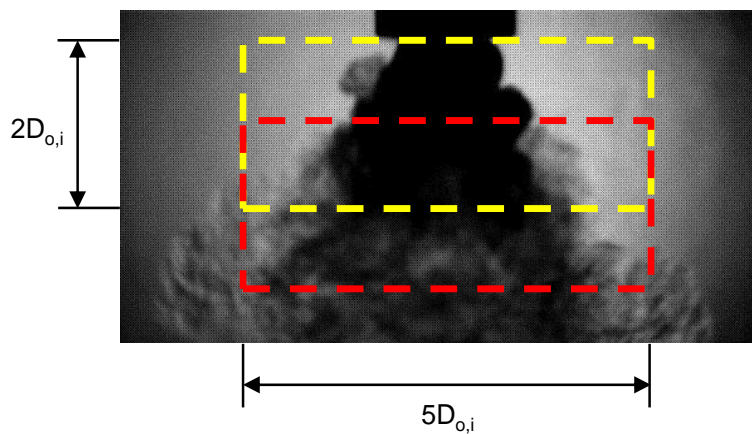


Fig. 4.3 Analysis area of the flow image for the upstream (yellow line) and downstream (red line) regions

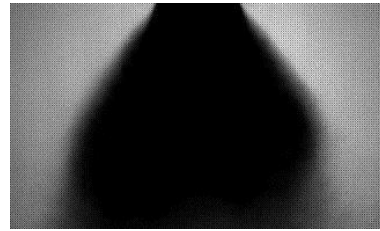
## **4.3 Results and Discussion**

### **4.3.1 Static characteristics of a cryogenic swirl flow**

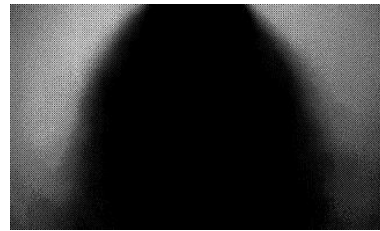
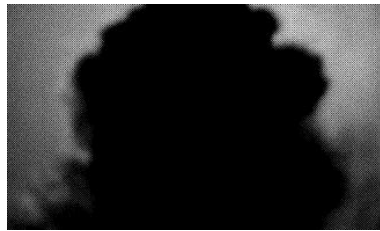
As previously mentioned, a cryogenic flow has significant instability [Cho et al., 2014; Zong and Yang, 2008]. Because of this, the flow was visualized using high-speed photography. The instantaneous and averaged images of the flow for each experimental condition are shown in Fig. 4.4.

In the instantaneous flow images, serious instability was observed on the flow surface. Many structures with various scales were superposed in the vicinity of the injector post region, which created a rough surface shape. The vortex ring structures were generated by Kelvin-Helmholtz instability at the downstream region where the phase change and the disintegration of the injectant occurred. These phenomena were most significant under subcritical conditions, as shown in Fig. 4.4(d).

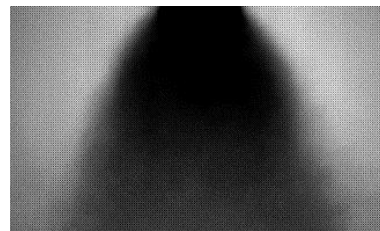
Many factors lead to instability of the flow surface, such as flow instability, relatively low surface tension of the cryogenic fluid, non-periodic surface change caused by phase change of the injectant, or interaction of the flow and its surroundings. If the most influencing factor among these is the natural instability of the flow, it can be supposed that various instability mechanisms can affect the cryogenic swirl flow. However, to prove this supposition, the coherent structures and frequencies that represent certain instability phenomena should be deduced from an analysis of the flow images.



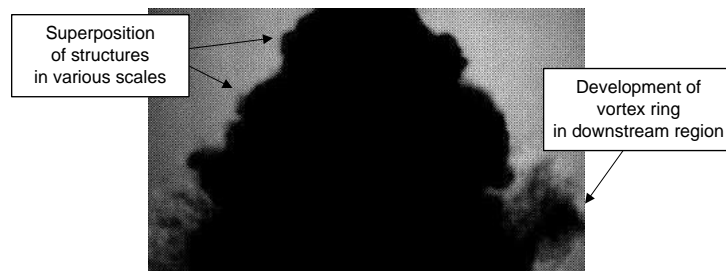
(a)  $P_c = 2.0$  MPa



(b)  $P_c = 3.4$  MPa



(b)  $P_c = 5.0$  MPa



(d)

Fig. 4.4 Representative images of the cryogenic swirl flow; instantaneous (left column) and averaged (right column) images for (a) subcritical, (b) critical, (c) supercritical ambient conditions, and (d) structures on the flow surface

Next, the spray angles were measured from the flow images to investigate the quantitative characteristics of the flow shape. Spray angle is a useful parameter to indicate the distribution of the injected flow. The results are shown in Fig. 4.5.

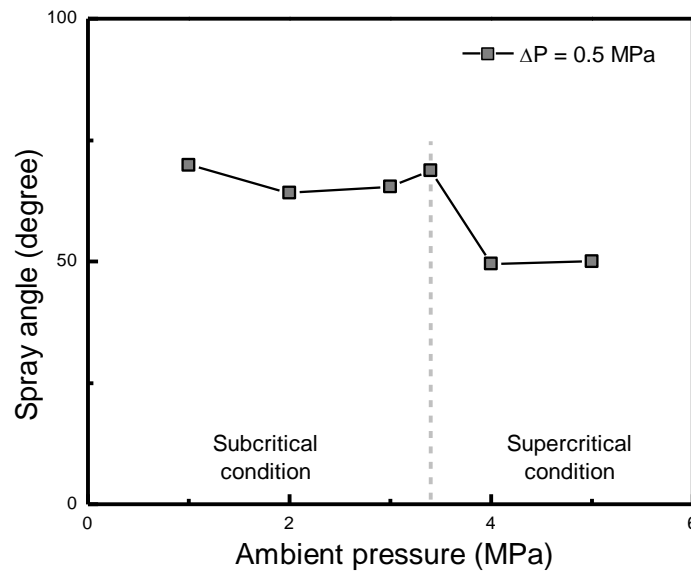


Fig. 4.5 Spray angle of the cryogenic swirl flow

The spray angle was abruptly decreased when the ambient pressure was changed from subcritical to supercritical pressure. The relationship between the angle and flow condition were then considered to account for this drastic decrease. The spray angle can be represented as follows.

$$\frac{\alpha}{2} = \tan^{-1} \frac{w}{u} \quad (4.5)$$

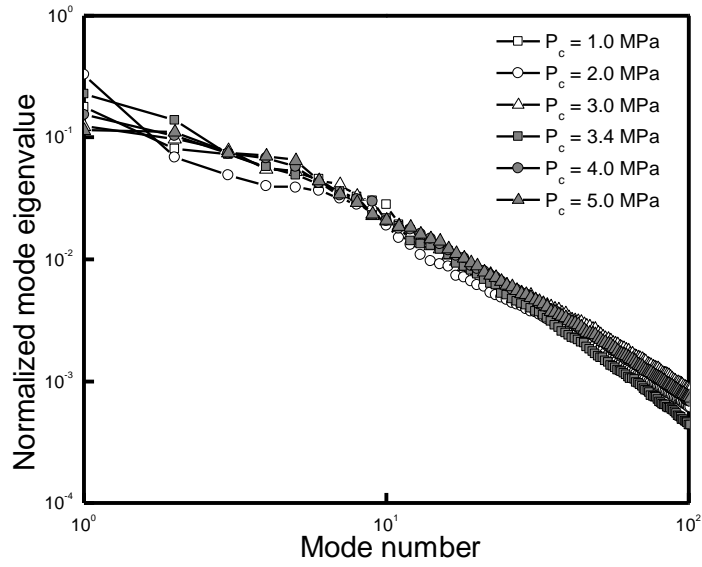
In this equation,  $\alpha$  is the spray angle,  $w$  is the tangential velocity, and  $u$  is the axial velocity of the flow. This equation shows that the spray angle is a parameter determined by the velocity of the flow. From equation (4.5) and Fig. 4.5, it can be deduced that the swirl strength of the flow was significantly decreased under supercritical conditions. Although an explanation for this decrease could not be determined in this study, it can be suggested that the injectant's phase change process, called the transcritical process, decreases the tangential velocity inside the injector more than the axial velocity component, and finally causes a decrease in the spray angle [Cho et al., 2014; Zong and Yang, 2008].

#### 4.3.2 POD analysis of flow image

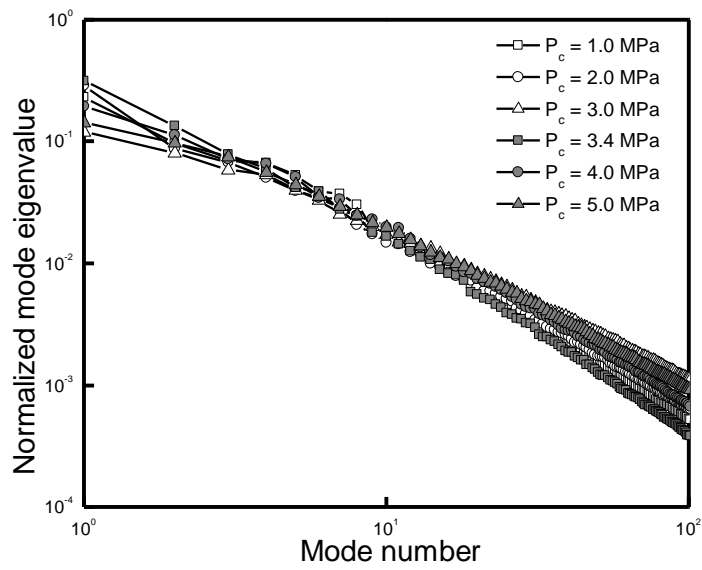
POD analysis was conducted on the set of flow images. First, the normalized mode eigenvalue distributions for each experimental condition were investigated. The following results are demonstrated in Fig. 4.6. It was observed that most of the total mode energies were distributed in the initial 10 ~ 20 modes. Therefore, the initial 10 modes for each condition were investigated in the analysis of the results obtained by POD analysis.

The initial 10 POD modes in upstream and downstream region for subcritical ( $P_c = 2.0$  MPa), critical ( $P_c = 3.4$  MPa), and supercritical ( $P_c = 5.0$  MPa) conditions are shown in Fig 4.7 to 4.12. Because there is no external excitation to the flow, the portion of the flow instability structure to the whole flow shape is small. Therefore, it can be supposed that the eigenvalue of the POD mode related to the instability would be smaller than the mode with mean flow shape.

Although mean flow image was extracted in the POD analysis analysis, the first POD mode under subcritical conditions is similar to the averaged image. Its normalized eigenvalue is between 0.2 to 0.3. In contrast, the first mode under supercritical conditions shows the instability structure on the flow surface and its eigenvalue is around 0.1. It implies that flow instability considerably affects to the behavior of the injectant under supercritical condition.



(a)



(b)

Fig. 4.6 POD mode eigenvalue distribution for the experimental conditions;  
 (a) upstream modes, and (b) downstream modes

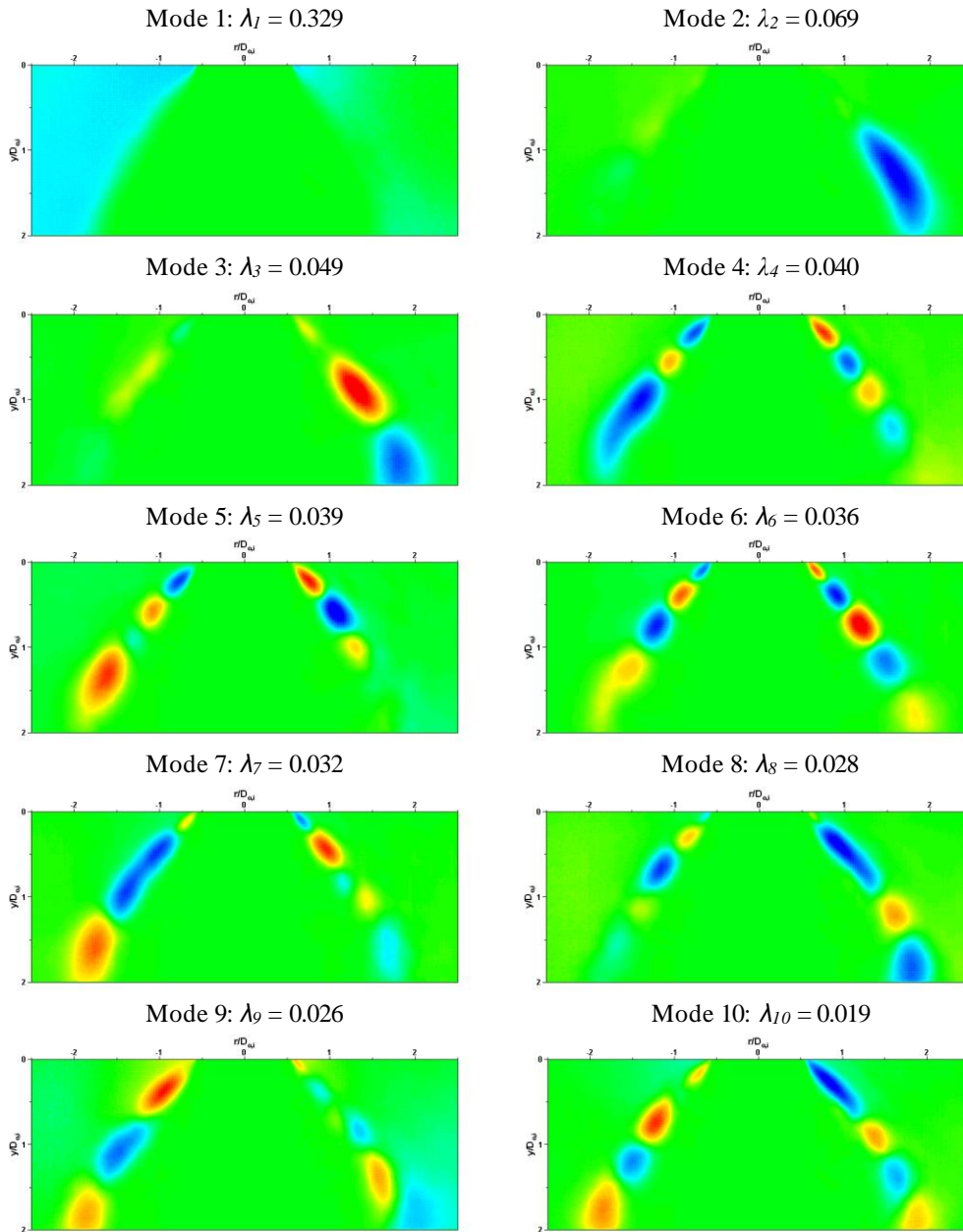


Fig. 4.7 Initial 10 POD modes for subcritical condition ( $P_c = 2.0$  MPa);  
upstream region

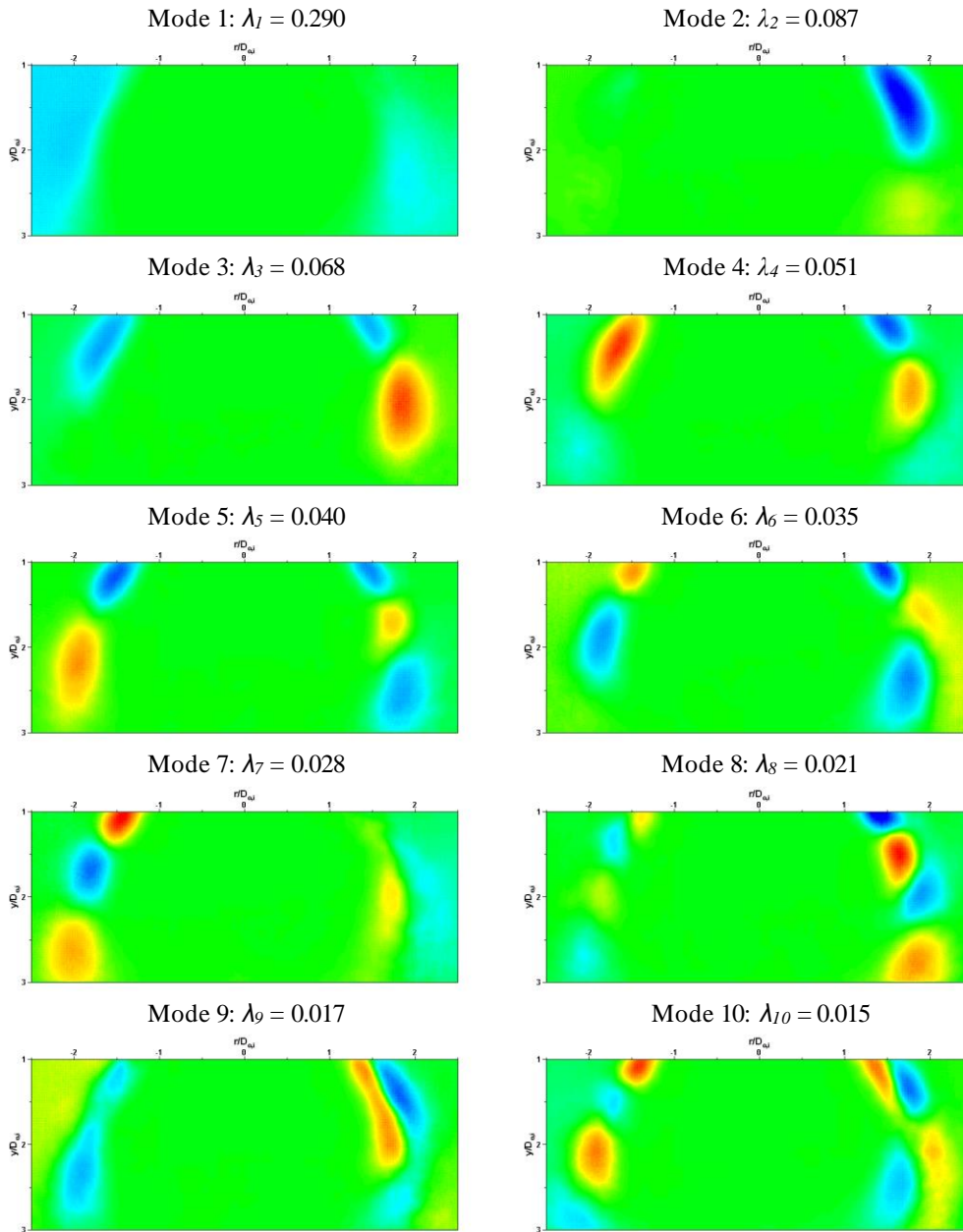


Fig. 4.8 Initial 10 POD modes for subcritical condition ( $P_c = 2.0$  MPa);  
downstream region

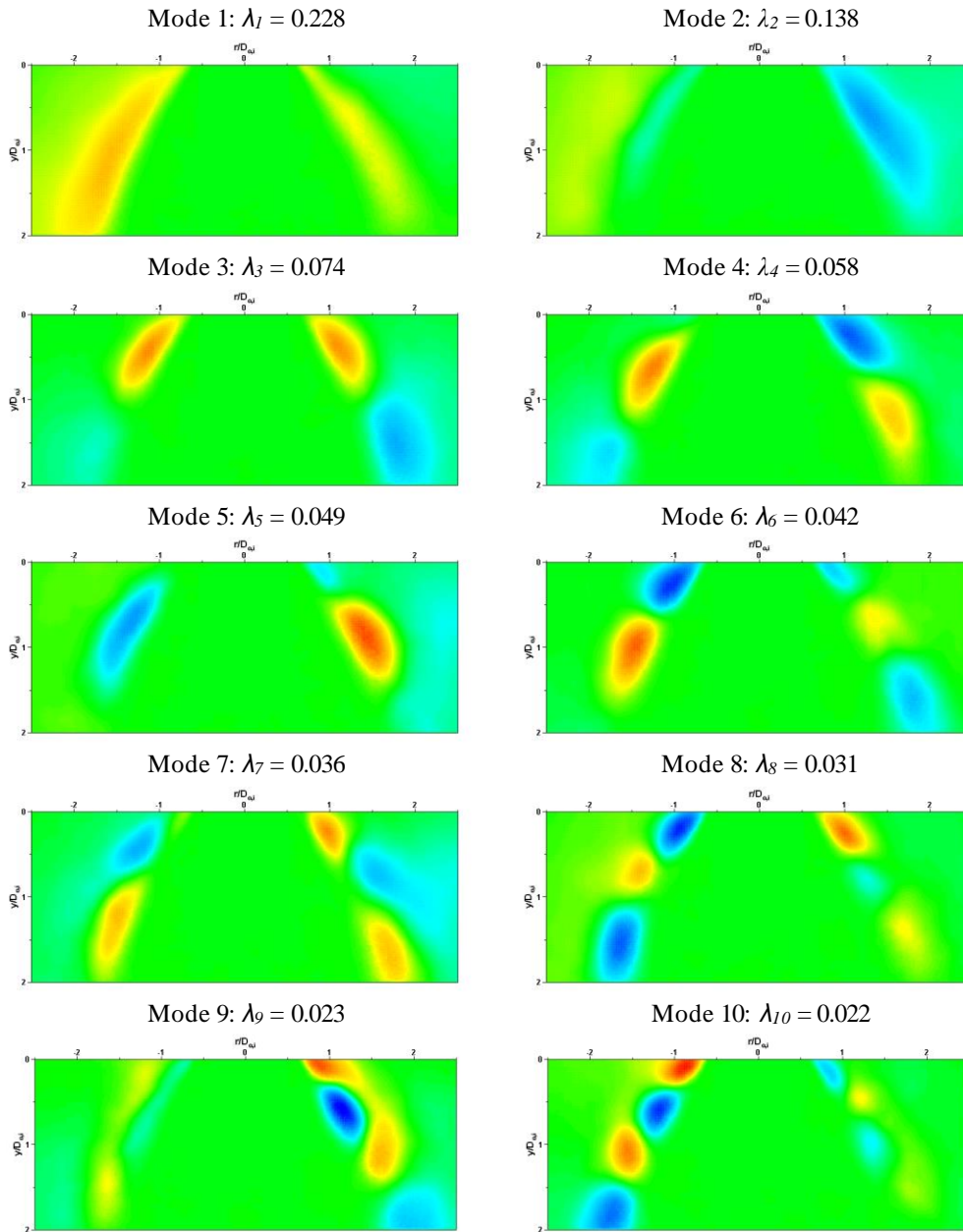


Fig. 4.9 Initial 10 POD modes for critical condition ( $P_c = 3.4$  MPa);  
upstream region

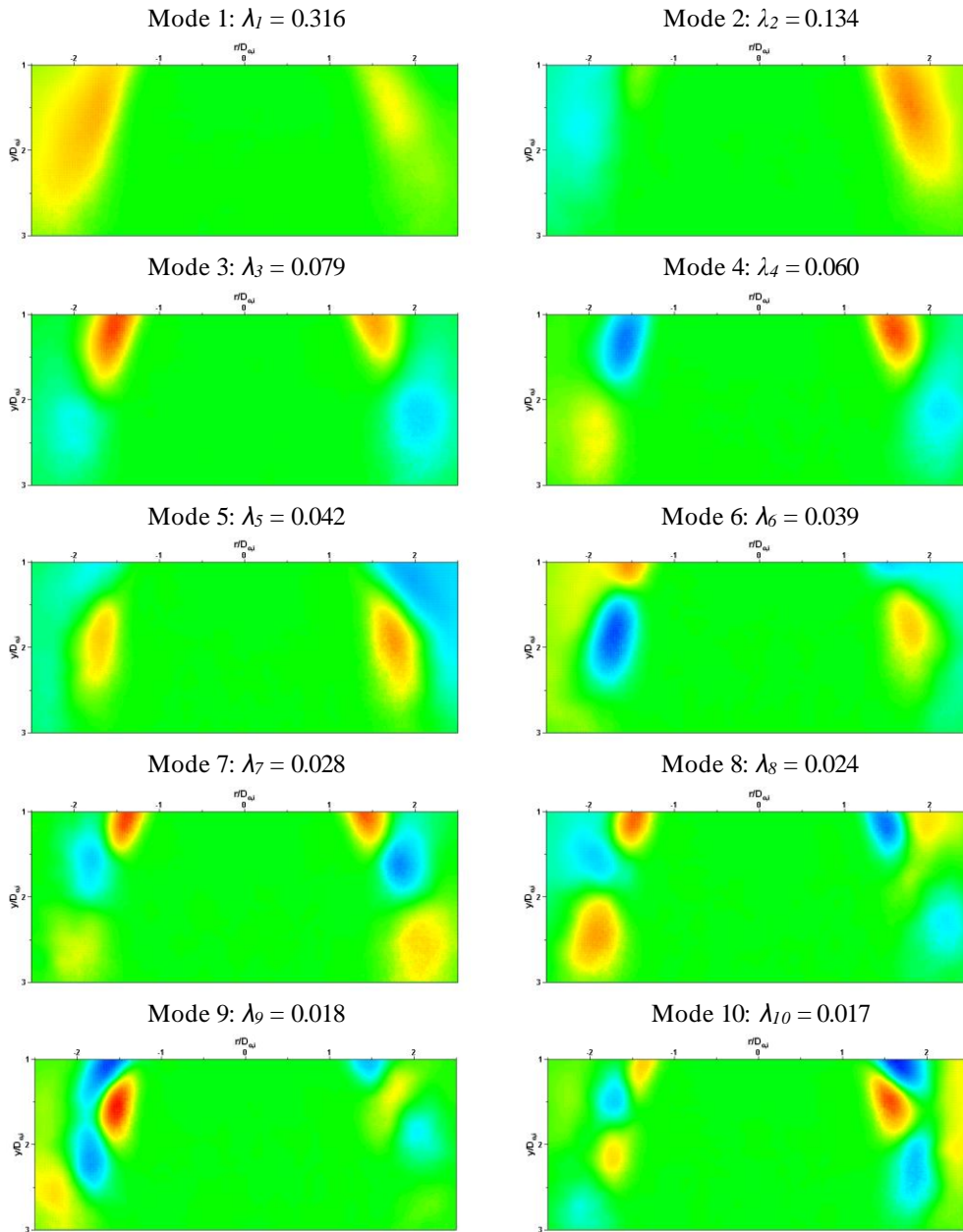


Fig. 4.10 Initial 10 POD modes for critical condition ( $P_c = 3.4$  MPa);  
downstream region

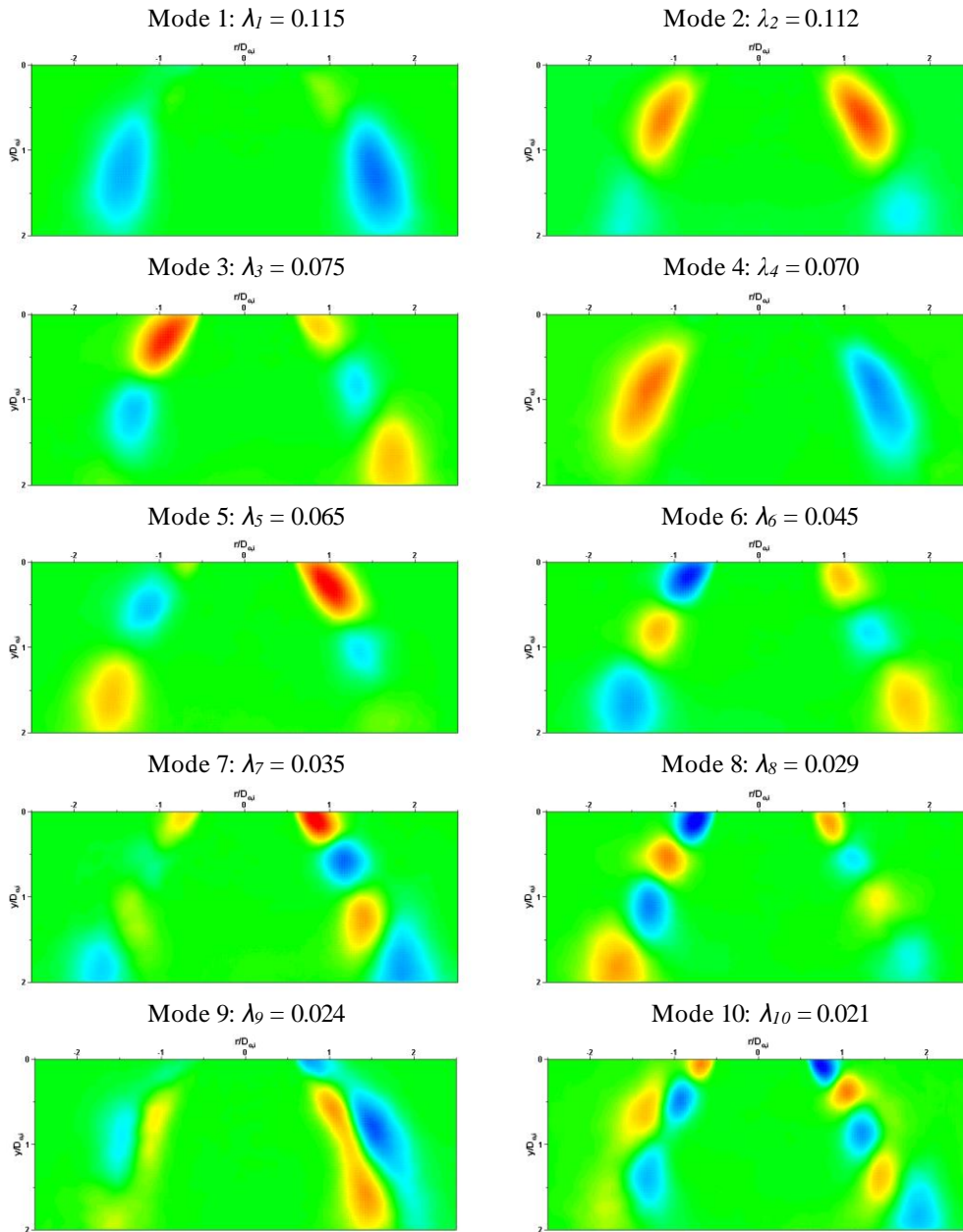


Fig. 4.11 Initial 10 POD modes for supercritical condition ( $P_c = 5.0$  MPa);  
upstream region

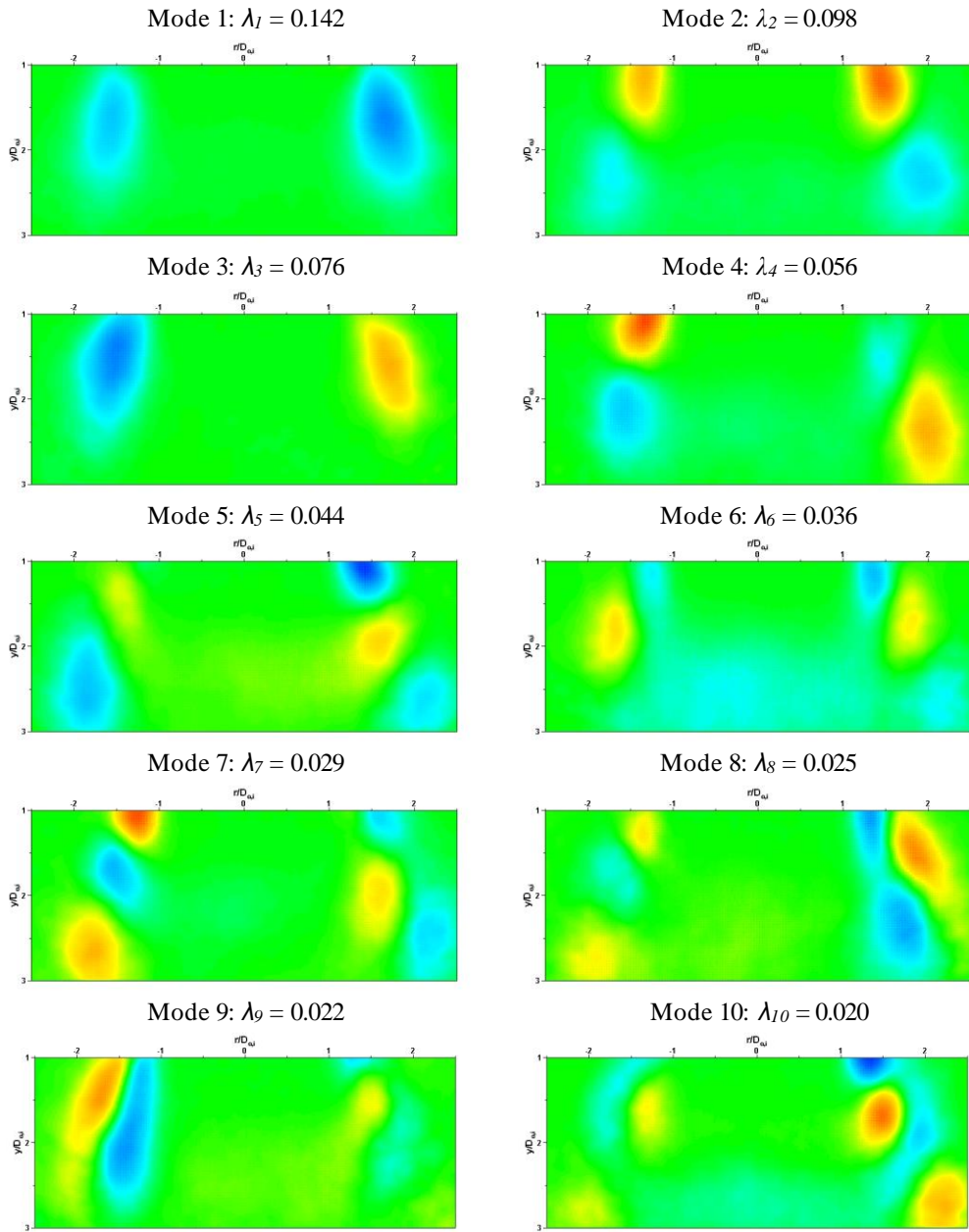


Fig. 4.12 Initial 10 POD modes for supercritical condition ( $P_c = 5.0$  MPa);  
downstream region

From the initial 10 POD modes, representative spatial modes were collected for each condition. The modes for the upstream region are shown in Fig. 4.13; those for the downstream region can be found in Fig. 4.14. The representative modes had their own coherent structures. These structures were aligned along the flow surface line, and the spatial characteristics of the flow were observable.

Two kinds of modes were found using POD analysis: a symmetric/tilted-ring shaped mode and an anti-symmetric shaped mode. The symmetric modes were generally found in the initial 1 to 5 modes. The coherent structures in this type of mode were located in the broad range of the analysis area, mainly in the downstream region. The scale of the structure size and the distance between each structure was large. In contrast, anti-symmetric modes could be found in modes 6 to 10, which have low eigenvalue compared to the symmetric modes. The coherent structures were located in the vicinity of the injector post, and the scale of their size and distance was relatively small. The categorization of the modes with these criteria was used in previous work [Markovich et al., 2014] for the analysis of swirl flow behavior. It was determined in this previous study that the coherent structures in each mode were generated by their own instability mechanisms.

First, the symmetric mode is generated by Kelvin-Helmholtz instability. The coherent structures arranged with symmetric shapes represent the vortex ring structures created by velocity shear between the flow and its surroundings. When the flow has a strong swirl momentum, the shape of the structure is shown as a tilted-ring rather than a symmetric structure. In cryogenic swirl flow, coherent structures in the symmetric mode were located far from the injector post. It can be supposed that this phenomena might be caused by the phase of the injectant which results in a huge influence of Kelvin-Helmholtz instability on flow behavior. As shown in Fig. 4.4, the phase change of the injectant in the downstream region induces a decrease of density and surface tension of the fluid, and finally, the flow easily loses its initial shape by external force.

In contrast, in the anti-symmetric mode, coherent structures are created by helical instability, which is related to the swirl of the flow. It is widely accepted that this

instability is commonly generated by the PVC in the central toroidal recirculation zone [Gallaire et al., 2004; Liang and Maxworthy, 2005; Syred, 2006; Wang et al., 2005]. PVC instability mainly occurs when the state of the injectant and its surroundings is similar when a gas flow is injected into the surrounding gas [Syred, 2006; Wang et al., 2005] or when a liquid flow is injected into the surrounding liquid [Gallaire et al., 2004; Liang and Maxworthy, 2005]. However, the instability mechanism seems different under conventional operating conditions for liquid swirl injectors where a liquid flow is injected into a surrounding gas under subcritical conditions. In this case, helical instability is generated by the instability of the liquid film inside the injector, and this instability affects the disintegration and atomization process of the flow [Cooper and Yule, 2001; Donjat et al., 2003; Kenny et al., 2009; Kim et al., 2009]. It has been suggested that the main reason for this instability is the precession of the air core inside the injector caused by the flow from the tangential inlet [Donjat et al., 2003]. These previous studies successfully explained the phenomena that the anti-symmetric structures were located in the vicinity of the injector post under subcritical conditions where the injectant remains in the liquid phase.

However, under supercritical conditions, the anti-symmetric structures were located in the broad range of the analysis area, as shown in Figs. 4.13 and 4.14. Under this condition, the swirl strength of the flow would be decreased inside the injector and cause the subsequent precession of the air core to diminish. As a result, the instability inside the injector would not be the main factor that dominates the instability of the external swirl flow. In this situation, the PVC instability mechanism would determine the characteristics of the helical instability. Because the properties of the injectant and the surroundings are similar under supercritical conditions, the PVC can dominate the flow behavior. A previous study conducted using numerical analysis [Zong and Yang, 2008] also insisted that the instability of the external swirl flow under supercritical conditions was dominated by PVC instability. Therefore, it can be inferred that when the condition of the surroundings is changed from subcritical to supercritical, the mechanism generating helical instability will also be changed.

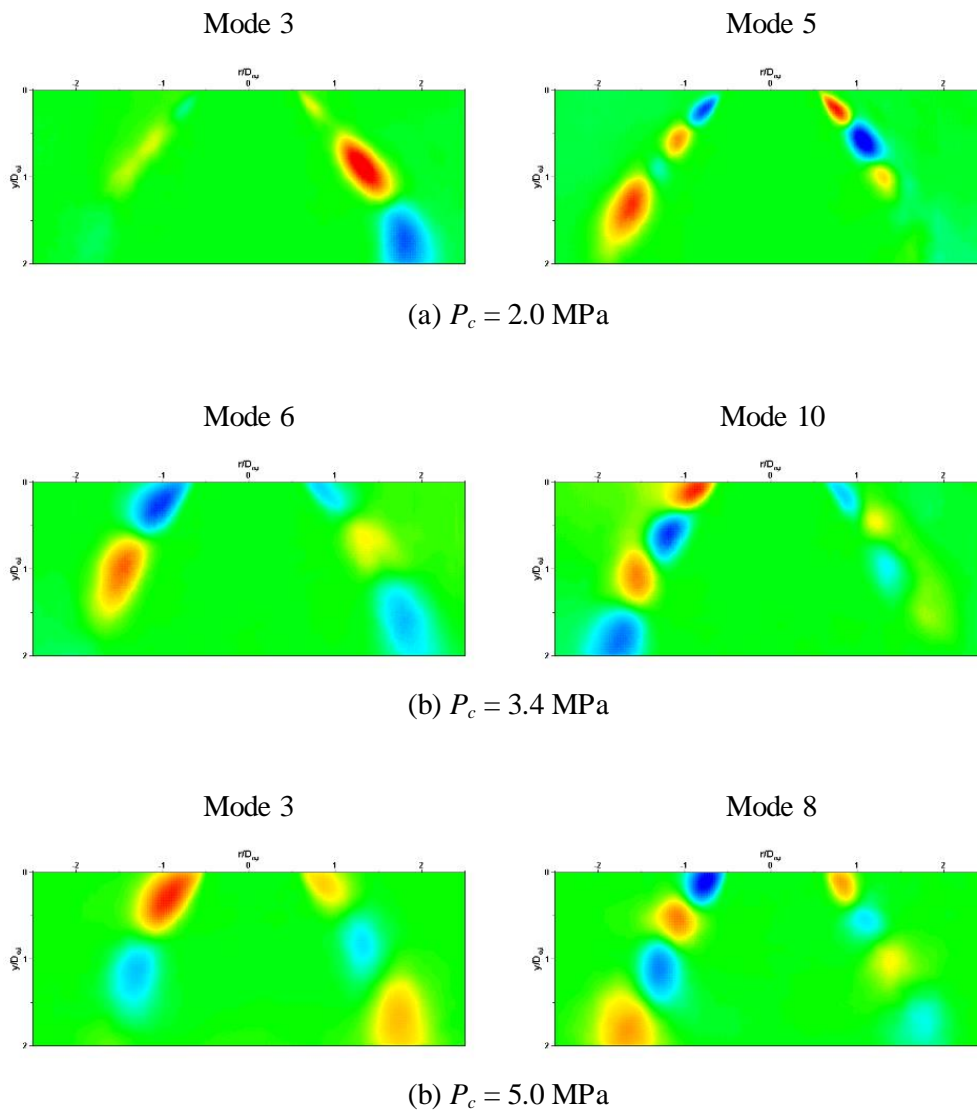


Fig. 4.13 Representative POD modes of the upstream cryogenic swirl flow; symmetric/tilted-ring structure (left column) and anti-symmetric structure (right column) modes for (a) subcritical, (b) critical, and (c) supercritical ambient conditions



### 4.3.3 Analysis of POD mode

Temporal and spatial analyses of the POD modes were conducted to identify the quantitative characteristics of the instabilities for each experimental condition. First, an analysis of a conjugate pair was attempted. A conjugate pair is determined from the cross-power spectrum analysis conducted on the time coefficients of two arbitrary modes. If the maximum amplitude of the spectrum is found at a phase with  $\pm 90^\circ$ , these two modes are thought to be a conjugate pair. The existence of a conjugate pair denotes that the coherent structures in the modes travel in the downstream direction [Arienti and Soteriou, 2009; Wegener et al., 2014]. In the present study, pairs existed in the anti-symmetric mode under most experimental conditions, while they were rarely found in the symmetric mode. This result implies that the vortex ring structure generated by Kelvin-Helmholtz instability does not travel along the flow direction with constant velocity. Because the vortex ring rotates counter to the flow direction, a part of the structure does not move downward. Therefore, it is obvious that a conjugate cannot be found in a set of symmetric modes. On the other hand, the axial velocity component of the flow is maintained in helical instability. With this velocity component, the coherent structures in the anti-symmetric mode propagate along the flow direction and consequently, a conjugate pair can be detected. An example of a conjugate pair in the anti-symmetric mode is shown in Fig. 4.15.

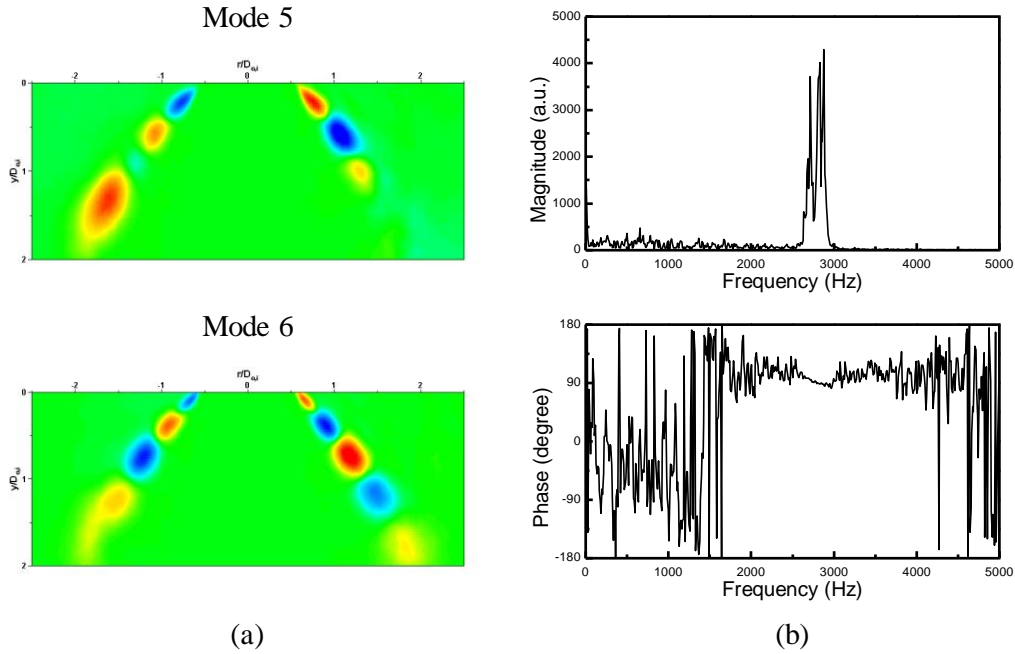


Fig. 4.15 Conjugate pair analysis of POD modes at  $P_c = 2.0$  MPa (upstream region): (a) conjugate mode images, and (b) cross-power spectral density for conjugate modes

For temporal analysis of the POD mode, time coefficients for representative POD modes were selected and spectral analysis was conducted. The peak instability frequency was deduced from the spectrum for each experimental condition. The frequencies obtained from the POD analysis and that from laser diagnostics method are compared in Fig. 4.16. In POD analysis, for each experimental conditions, significant peak frequency was observed only for the anti-symmetric mode obtained in the upstream region. In previous work, it was pointed out that the dissipation of the highly turbulent flow in this region would spread the instability energy to instabilities with other frequencies [Semeraro et al., 2012]. Thus, it is reasonable that the instability frequency was found only in the upstream region.

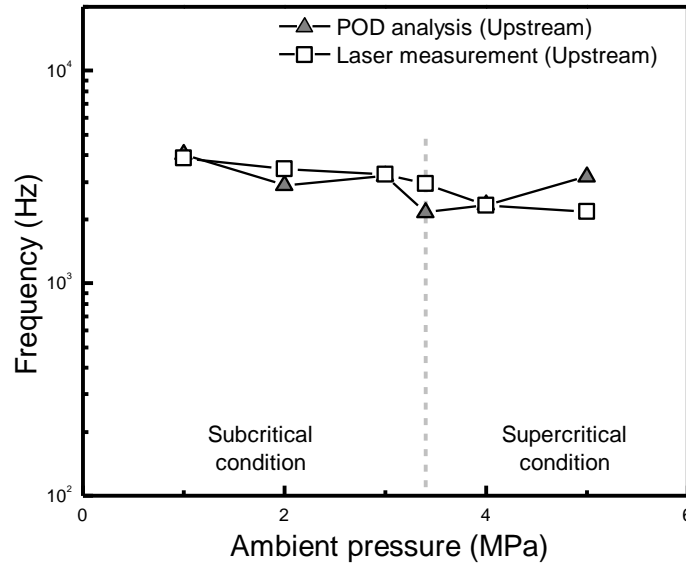


Fig. 4.16 Instability frequency of POD modes in the cryogenic swirl flow

The frequencies of the anti-symmetric modes were higher than 2 kHz, within the frequency range of combustion instability. The change of frequency along with the ambient pressure was different for subcritical and supercritical conditions. The instability frequency of the anti-symmetric mode was decreased along the ambient pressure under subcritical conditions, while it was increased under supercritical conditions.

It is clear that the instability propagated from the inside of the injector is weakened and its frequency is decreased when the ambient pressure increases. However, in the present study, the frequency of the instability generated by the PVC was increased along with the ambient pressure under supercritical conditions. Although further study is required for the explanation of this phenomenon, the results showing that the change of instability frequency is different for each condition support the existence of different instability mechanisms for subcritical and supercritical conditions.

Meanwhile, instability frequencies measured from laser diagnostics were similar to

the frequencies obtained from POD analysis. As shown in Fig. 4.7 to 4.12, anti-symmetric structures of the flow appear in the vicinity of the injector post. Therefore, the result of frequency measurement implies that the helical instability mainly determines the behavior of the flow instability in the region where the injectant remains in liquid state. However, when  $P_c = 5.0$  MPa, frequency measured from laser diagnostics was 2.1 kHz while that of POD analysis was 3.1kHz. The reason of this difference is not clear. Thus, additional study should be conducted.

The wavelength of the coherent structure was measured to discover the spatial characteristics of the spatial modes in the flow. In each mode, the wavelength was measured from the distances between the structures. The obtained results are shown in Fig. 4.17. The wavelength in the anti-symmetric mode was relatively smaller than that of the symmetric structure under the subcritical condition. This denotes that different instability mechanisms are applied to each mode. Meanwhile, the wavelength of the coherent structure increased in the downstream region, which indicates dissipation of the flow.

The wavelengths for each mode had similar values in the downstream regions or under supercritical conditions. Moreover, in such cases, as shown in Figs. 4.7 to 4.12, it was difficult to distinguish the symmetric and anti-symmetric structures. The most significant similar characteristic for both cases is that most of the injectants were changed from liquid to gas or to supercritical fluid, which behaves like dense gas. This result implies that when the phase of the injectant is changed to a gas-like state, its instability characteristics become similar for each experimental condition.

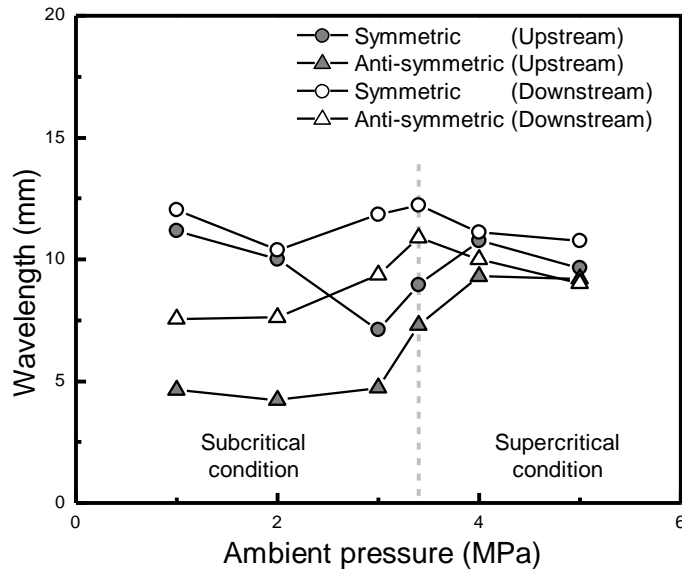


Fig. 4.17 Wavelength of POD modes in the cryogenic swirl flow

## CHAPTER 5

### CONCLUSION AND FUTURE WORK

#### 5.1 Conclusion

The characteristics of the cryogenic swirl flows under subcritical to supercritical conditions were investigated experimentally. High-speed photography and frequency measurement method using laser diagnostics were used to analyze the flow characteristics. The flow characteristics were observed in qualitative and quantitative manner, and spatial and temporal analysis was conducted. Spray angle and other static characteristics were investigated, and surface wave analysis and the POD analysis were used to obtain the surface instability and the dynamic characteristics of the flow. Although the datasets are limited because of the difficulty in flow measurement, the following results were obtained.

1. The characteristics of the cryogenic swirl flow were identified. Due to the fast phase change, and low density, and surface tension of the injectant, unstable structures on the flow surface were generated. The flow instability was caused by a PVC, and the scale of the instability was significantly larger than that of the water flow.
2. The effect of the ambient pressure to the cryogenic swirl flow were investigated. Due to the differences in each condition, the flow characteristics were changed during the transition from subcritical to supercritical pressure, occurring before and then after the phase change as well. These differences also affected the instability on the flow surface, creating a helical wave initially, which then developed into a roll-up vortex structure.
3. The instability frequency of the flow was measured. As the flow changes periodically, the instability frequency can be calculated via spectral analysis of the transmission rate of a laser beam passing through the flow. The frequency decreased when the ambient pressure increased. This result is explained by the decrease in the

propagation velocity of the surface structure.

4. From the POD analysis, the coexistence of two types of modes was ascertained: a symmetric/tilted-ring shaped mode and an anti-symmetric shaped mode. The symmetric structures in the mode represented the vortex ring generated by Kelvin-Helmholtz instability. This mainly occurred in the downstream region of the flow and created large-scale structures.
5. The anti-symmetric mode was created by helical instability. This instability had high-order frequency. The mechanism generating the instability was different for subcritical and supercritical conditions. Under subcritical conditions, the high swirl strength of the flow inside the injector generated the instability and the resulting structure was located in the vicinity of the injector post where the injectant remained in a liquid state. Under supercritical conditions, the swirl strength was decreased and the instability was generated by PVC, which dominates the flow behavior when the states of the injectant and its surroundings are similar. The range of the instability frequencies and the related instability mechanisms is thought to be related to the instabilities that exist in liquid propellant rocket engines.
6. In the downstream region or under supercritical conditions, the spatial characteristics of the coherent structures become similar. This result implies that when the injected flow loses its energy by interaction with the surrounding environment, and when the phase of the injectant is changed and its properties become similar to the surrounding environment, the mixing of the flow and its surroundings would be enhanced and its own instability characteristics would be diminished. Especially under supercritical conditions, because the injectant's phase change process is significantly different from that under subcritical conditions, in-depth consideration of flow behavior is required to understand flow characteristics.

## 5.2 Recommendations for Future Work

This study mainly focused on the analysis of the flow image. Although the image can be related to the density distribution of the injectant, it shows the opacity of the flow. Therefore, the real property data of the flow cross section cannot be adopted. To solve this problem, Raman spectroscopy have been used in many research to investigate the characteristics of the single/coaxial liquid nitrogen jet flow [Chehroudi et al., 2002a; Oswald and Schik, 1999]. This method measures the density distribution of the flow without interrupting the flow. However, some problems can be occurred in use of this method to the cryogenic swirl flow. Because the intensity of Raman signal from the swirl flow would be much smaller than that of the jet flow, serious attenuation and distortion of signal could occur. Therefore, various techniques would be needed in correction of the signal.

Meanwhile, POD analysis was conducted to investigate the characteristics of time-resolved flow images. However, this method deduces spiatially orthogonal flow structures which cannot be directly related to the flow instability. As an alternative of POD method, Dynamic Mode Decomposition (DMD) method was suggested to obtain the temporally orthogonal flow structure [Schmid, 2010]. Because of the characteristics of DMD, it can be expected that the obtained DMD mode could provide important information of flow instability.

Finally, laser-using flow instability frequency measurement should be conducted in detail. Because the flow is dissipated as it moves downward, the instability frequency would be different for each location [Schmitt et al., 2012; Zong and Yang, 2008]. Therefore, measurement of the frequency at various position along radial and axial direction would help the in-depth understanding of the flow instability.

## APPENDIX

### PROPER ORTHOGONAL DECOMPOSITION

#### A.1 Background

Proper Orthogonal Decomposition (POD) is the method which have been used for the analysis of the flow characteristics. This method have been used as the Principal Component Analysis (PCA) in statistics, and Karhunen-Loève Transform (KLT) in signal processing. POD method deduces the “modes” which represent the coherent structure of the flow. Each mode are spatially orthogonal, and the modes are ranked according to the energy/eigenvalue of each mode.

#### A.2 POD Analysis Procedure

The conventional process of POD analysis is shown in this section as follows.

First, the set of flow field data/spatially uncorrelated coherent structure  $V$  can be presented as Eq. A.1.

$$V = [v_1 \quad v_2 \quad v_3 \quad \cdots \quad v_n \quad \cdots \quad v_N]$$
$$= \begin{bmatrix} v_{1,1} & v_{1,2} & v_{1,3} & \cdots & v_{1,n} & \cdots & v_{1,N} \\ v_{2,1} & v_{2,2} & v_{2,3} & \cdots & v_{2,n} & \cdots & v_{2,N} \\ \vdots & \vdots & \vdots & \vdots & \vdots & \vdots & \vdots \\ v_{M,1} & v_{M,2} & v_{M,3} & \cdots & v_{M,n} & \cdots & v_{M,N} \end{bmatrix} \quad (\text{A.1})$$

$$v_n = \begin{bmatrix} v_{1,n} \\ v_{2,n} \\ \vdots \\ v_{M,n} \end{bmatrix} : n^{\text{th}} \text{ snapshot data} \quad (\text{A.2})$$



A shows the temporal evolution of coherent structures.

$$\begin{aligned}
 A &= [a_1 \quad a_2 \quad a_3 \quad \cdots \quad a_n \quad \cdots \quad a_N] \\
 &= \begin{bmatrix} a_{1,1} & a_{1,2} & a_{1,3} & \cdots & a_{1,n} & \cdots & a_{1,N} \\ a_{2,1} & a_{2,2} & a_{2,3} & \cdots & a_{2,n} & \cdots & a_{2,N} \\ \vdots & \vdots & \vdots & \vdots & \vdots & \vdots & \vdots \\ a_{n,1} & a_{n,2} & a_{n,3} & \cdots & a_{n,n} & \cdots & a_{n,N} \\ \vdots & \vdots & \vdots & \vdots & \vdots & \vdots & \vdots \\ a_{N,1} & a_{N,2} & a_{N,3} & \cdots & a_{N,n} & \cdots & a_{N,N} \end{bmatrix} \quad (A.7)
 \end{aligned}$$

The symbol ‘\*’ means the conjugate transpose.

From these contents, the flowfield snapshot  $v_n$  can be represented as the linear summation of components of  $\Phi$ ,  $\Sigma$  and  $A$ .

$$\begin{aligned}
 v_n &= \sigma_1 a_{n,1} \phi_1 + \sigma_2 a_{n,2} \phi_2 + \sigma_3 a_{n,3} \phi_3 + \cdots + \sigma_N a_{n,N} \phi_N \\
 &= \sum_{i=1}^N \sigma_i a_{n,i} \phi_i \quad (A.8)
 \end{aligned}$$

It can be thought that  $V$  is  $M$  by  $N$  matrix where  $M$  is number of flow field data point and  $N$  is number of snapshots. Because  $M$  is much larger than  $N$ , the full-size SVD might be impossible with limited computer source. Therefore, the reduced SVD can be adopted in the POD analysis. In this study, eigenvalue decomposition of covariance matrix  $Z$  was used as follows.

$$Z = V^* V = A \Sigma \Phi^* \Phi \Sigma A^* = A \Sigma^2 A^* \quad (A.9)$$

By solving eigenvalue problem of  $Z$ ,

$$ZA = A \Sigma^2 \quad (A.10)$$

$$VA = \Phi \Sigma \quad (\text{A.11})$$

By normalization of column in  $VA$  in Eq. A.11,  $\Phi$  can be calculated.  $\Sigma^2$  shows the eigenvalue or energy content of  $\phi$ . The eigenvalue for each mode can be related to the mode energy when  $v$  contains velocity data only and the flow is incompressible.

## **BIBLIOGRAPHY**

- Arienti M, Soteriou MC (2009) Time-resolved proper orthogonal decomposition of liquid jet dynamics. *Phys Fluids* 21:112104.
- Banuti DT, Hannemann K (2014) Supercritical pseudo-boiling and its relevance for transcritical injection. In: The 50th AIAA/ASME/SAE/ASEE Joint Propulsion Conference, Cleveland, USA.
- Bayvel L (1993) *Liquid Atomization* vol 1040. vol 2756. Taylor & Francis, Washington.
- Bazarov VG, Yang V (1998) Liquid-propellant rocket engine injector dynamics. *J Propul Power* 14:797-806.
- Berkooz G, Holmes P, Lumley JL (1993) The proper orthogonal decomposition in the analysis of turbulent flows. *Annu Rev Fluid Mech* 25:539-575.
- Borodin VA, Dityakin YF, Klyachko LA, Yagodkin VI (1968) *Atomization of Liquids*. Air Force Foreign Technology Division Report, FTD-MT-24-97-68 (AD685151).
- Chehroudi B (2010) Physical hypothesis for the combustion instability in cryogenic liquid rocket engines. *J Propul Power* 26:1153-1160.
- Chehroudi B, Cohn R, Talley D (2002a) Cryogenic shear layers: experiments and phenomenological modeling of the initial growth rate under subcritical and supercritical conditions. *International journal of heat and fluid flow* 23:554-563.
- Chehroudi B, Talley D, Coy E (2002b) Visual characteristics and initial growth rates of round cryogenic jets at subcritical and supercritical pressures. *Phys Fluids* 14:850-861.
- Chehroudi B, Talley D, Mayer W, Branam R, Smith JJ (2003) Understanding injection into high pressure supercritical environments. In: 5th International Symposium on Liquid Space Propulsion, Chattanooga, TN.
- Cho S, Park G, Chung Y, Yoon Y, Bazarov VG (2014) Surface instability on cryogenic swirl flow at sub- to supercritical conditions. *J Propul Power* 30:1038-1046.
- Clark CJ, Dombrowski N (1972) Aerodynamic instability and disintegration of inviscid liquid sheets. *Proceedings of the Royal Society of London A Mathematical and*

- Physical Sciences 329:467-478.
- Cooper D, Yule A (2001) Waves on the air core/liquid interface of a pressure swirl atomizer. In: The 17th Annual Conference on Liquid Atomization and Spray Systems, Zurich, Switzerland. 2001
- Culick FEC, Yang V (1995) Overview of combustion instabilities in liquid-propellant rocket engines. In: Yang V, Anderson WE (eds) Liquid rocket engine combustion instability, Progress in Astronautics and Aeronautics, vol 169. AIAA, Washington, DC, pp 3-37.
- Davis DW, Chehroudi B (2007) Measurements in an acoustically driven coaxial jet under sub-, near-, and supercritical conditions. *J Propul Power* 23:364-374.
- Decker M, Schik A, Meier UE, Stricker W (1998) Quantitative Raman imaging investigations of mixing phenomena in high-pressure cryogenic jets. *Appl Opt* 37:5620-5627.
- Dityakin YF, Klyachko LA, Novikov BV, Yagodkin VI (1977) Atomization of Liquids. Mashinostroenie, Moscow.
- Dombrowski N, Johns WR (1963) The Aerodynamic instability and disintegration of viscous liquid sheets. *Chem Eng Sci* 18:203-214.
- Donjat D, Estivalezes J-L, Michau M, Lavergne G (2003) Phenomenological study of the pressure swirl atomizer internal flow. In: The 9th International Conference on Liquid Atomization and Spray Systems, Sorrento, Italy.
- Eberhart CJ, Lineberry DM, Frederick Jr. RA (2012) Propellant throttling effects on self-pulsation of liquid rocket swirl-coaxial injection. In: 48th AIAA/ASME/SAE/ASEE Joint Propulsion Conference & Exhibit, Atlanta, USA.
- Fu Q-F, Yang L-J, Zhang W, Cui K-D (2012) Spray characteristics of an open-end swirl injector. *Atomization Spray* 22:431-445.
- Gallaire F, Rott S, Chomaz J-M (2004) Experimental study of a free and forced swirling jet. *Phys Fluids* 16:2907-2917.
- Han ZY, Parrish S, Farrell PV, Reitz RD (1997) Modeling atomization processes of pressure-swirl hollow-cone fuel sprays. *Atomization Spray* 7:663-684.

- Heo J-Y, Kim K, Sung H-G, Choi H-S, Yang V (2012) Numerical study for kerosene/LOx supercritical mixing characteristics of a swirl injector. In: 50th AIAA Aerospace Sciences Meeting including the New Horizons Forum and Aerospace Exposition.
- Huo H, Wang X, Yang V (2014) Flow dynamics of a simplex swirl injector at supercritical conditions. In: The 52nd Aerospace Sciences Meeting, National Harbor, USA.
- Hutt JJ, Cramer JM (1996) Advanced rocket injector development at the Marshall Space Flight Center. In: AIAA, Space Programs and Technologies Conference, Huntsville, AL. Sep.
- Im J-H, Kim D, Han P, Yoon Y, Bazarov V (2009) Self-pulsation characteristics of a gas-liquid swirl coaxial injector. *Atomization Spray* 19:57-74.
- Kenny RJ, Hulka JR, Moser MD, Rhys NO (2009) Effect of chamber backpressure on swirl injector fluid mechanics. *J Propul Power* 25:902-913.
- Khavkin Y (2004) *The Theory and Practice of Swirl Atomizers*. Taylor & Francis, New York.
- Kim D, Im J-H, Koh H, Yoon Y (2007) Effect of ambient gas density on spray characteristics of swirling liquid sheets. *J Propul Power* 23:603-611.
- Kim JG (2013) Spray structures in high pressure environment of gas-centered swirl coaxial injector for staged combustion cycle engines. Ph.D. Thesis, Seoul National University
- Kim S, Khil T, Kim D, Yoon Y (2009) Effect of geometric parameters on the liquid film thickness and air core formation in a swirl injector. *Meas Sci Technol* 20:015403.
- Landwehr F, Feggeler D, Walzel P, Weichert F, Schröter N, Müller H (2006) A fibre sensor based frequency analysis of surface waves at hollow cone nozzles. *Exp Fluids* 40:523-532.
- Lefebvre AH (1989) *Atomization and Sprays*. Hemisphere, New York.
- Liang H, Maxworthy T (2005) An experimental investigation of swirling jets. *J Fluid Mech* 525:115-159.
- Linstrom PJ, Mallard WG NIST Chemistry WebBook, NIST Standard Reference

- Database Number 69. National Institute of Standards and Technology, Gaithersburg MD, 20899, <http://webbook.nist.gov>, (retrieved February 6, 2013).
- Marchione T, Allouis C, Amoresano A, Beretta F (2007) Experimental investigation of a pressure swirl atomizer spray. *J Propul Power* 23:1096-1101.
- Markovich DM, Abdurakipov SS, Chikishev LM, Dulin VM, Hanjalić K (2014) Comparative analysis of low- and high-swirl confined flames and jets by proper orthogonal and dynamic mode decompositions. *Phys Fluids* 26:065109.
- Mayer W, Tamura H (1996) Propellant injection in a liquid oxygen/gaseous hydrogen rocket engine. *J Propul Power* 12:1137-1147.
- Mayer W, Telaar J, Branam R, Schneider G, Hussong J (2003) Raman measurements of cryogenic injection at supercritical pressure. *Heat and Mass Transfer* 39:709-719.
- Mayer WOH, Ivancic B, Schik A, Hornung U (2001) Propellant atomization and ignition phenomena in liquid oxygen/gaseous hydrogen rocket combustors. *J Propul Power* 17:794-799.
- Mayer WOH, Schik AH, Vielle B, Chauveau C, Gökalp I, Talley DG, Woodward RD (1998) Atomization and breakup of cryogenic propellants under high-pressure subcritical and supercritical conditions. *J Propul Power* 14:835-842.
- Meyer KE, Pedersen JM, Özcan O (2007) A turbulent jet in crossflow analysed with proper orthogonal decomposition. *J Fluid Mech* 583:199-227.
- Miller RS, Harstad KG, Bellan J (2001) Direct numerical simulations of supercritical fluid mixing layers applied to heptane–nitrogen. *J Fluid Mech* 436:1-39.
- Musemic E, Rojek A, Gaspar M, Weichert F, Müller H, Walzel P (2009) Experimental analysis and 3D-visualization of oscillating hollow-conical liquid sheets in quiescent air. In: *The 11th International Conference on Liquid Atomization and Spray Systems*, Vail, USA.
- Newman JA, Brzustowski T (1971) Behavior of a liquid jet near the thermodynamic critical region. *AIAA journal* 9:1595-1602.
- Oefelein JC, Yang V (1993) Comprehensive review of liquid-propellant combustion instabilities in F-1 engines. *J Propul Power* 9:657-677.

- Oefelein JC, Yang V (1998) Modeling high-pressure mixing and combustion processes in liquid rocket engines. *J Propul Power* 14:843-857.
- Oschwald M, Schik A (1999) Supercritical nitrogen free jet investigated by spontaneous raman scattering. *Exp Fluids* 27:497-506.
- Oschwald M, Smith J, Branam R, Hussong J, Schik A, Chehroudi B, Talley D (2006) Injection of fluids into supercritical environments. *Combustion Science and Technology* 178:49-100.
- Park H, Heister SD (2006) Nonlinear simulation of free surfaces and atomization in pressure swirl atomizers. *Phys Fluids* 18:052103-052111.
- Rubinsky VR (1995) Combustion instability in the RD-0110 engine. In: Yang V, Anderson WE (eds) *Liquid rocket engine combustion instability, Progress in Astronautics and Aeronautics*, vol 169. AIAA, Washington, DC, pp 89-112.
- Schmid PJ (2010) Dynamic mode decomposition of numerical and experimental data. *J Fluid Mech* 656:5-28.
- Schmitt T, Rodriguez J, Leyva IA, Candel S (2012) Experiments and numerical simulation of mixing under supercritical conditions. *Phys Fluids* 24:055104.
- Semeraro O, Bellani G, Lundell F (2012) Analysis of time-resolved PIV measurements of a confined turbulent jet using POD and Koopman modes. *Exp Fluids* 53:1203-1220.
- Senecal PK, Schmidt DP, Nouar I, Rutland CJ, Reitz RD, Corradini ML (1999) Modeling high-speed viscous liquid sheet atomization. *Int J Multiphas Flow* 25:1073-1097.
- Sterling AM, Sleicher CA (1975) The instability of capillary jets. *J Fluid Mech* 68:477-495.
- Strakey P, Talley D, Hutt J (2001) Mixing characteristics of coaxial injectors at high gas/liquid momentum ratios. *J Propul Power* 17:402-410.
- Syred N (2006) A review of oscillation mechanisms and the role of the precessing vortex core (PVC) in swirl combustion systems. *Prog Energ Combust* 32:93-161.
- Talley DG (2002) Recent developments in liquid rocket injectors. In: *Liquid Propulsion Systems—Evolution and Advancements*, Indianapolis, IN, USA. 11-12 July 2002
- Teshome S, Leyva I, Talley D, Karagozian A (2012) Cryogenic high-pressure shear-

- coaxial jets exposed to transverse acoustic forcing. In: The 50th AIAA Aerospace Sciences Meeting including the New Horizons Forum and Aerospace Exposition, Sashville, USA. Jan.
- Wang S, Hsieh S-Y, Yang V (2005) Unsteady flow evolution in swirl injector with radial entry. I. Stationary conditions. *Phys Fluids* 17:045106.
- Wegener JL, Forliti DJ, Leyva IA, Talley DG (2014) Receptivity of a cryogenic coaxial gas-liquid jet to acoustic disturbances. In: The 50th AIAA/ASME/SAE/ASEE Joint Propulsion Conference, Cleveland, USA.
- Yang V (2000) Modeling of supercritical vaporization, mixing, and combustion processes in liquid-fueled propulsion systems. *P Combust Inst* 28:925-942.
- Zong N, Meng H, Hsieh S-Y, Yang V (2004) A numerical study of cryogenic fluid injection and mixing under supercritical conditions. *Phys Fluids* 16:4248-4261.
- Zong N, Yang V (2008) Cryogenic fluid dynamics of pressure swirl injectors at supercritical conditions. *Phys Fluids* 20:056103.

## 초 록

극저온 스월 유동의 불안정 특성에 대한 실험적 연구를 수행하였다. 극저온 액체 질소를 스월 분사기를 통하여 고압 챔버 내에 분사시켰으며, 이때 유동의 주위 환경은 질소의 아임계 및 초임계 압력 조건이 되도록 변화시켰다. 초고속 카메라 촬영 기법을 이용하여 시간에 따라 빠르게 변화하는 유동의 이미지를 획득하였으며, 이미지 처리 기법을 이용하여 유동의 특성을 분석하였다. 또한 레이저 이용 유동 계측 기법 및 유동 이미지 분석을 통하여 유동의 불안정 주파수를 계측하였다.

우선, 아임계 및 초임계 조건에서의 유동 표면 불안정성을 연구하였다. 일반적인 액체 유동과 극저온 유동을 비교하였을 때 뚜렷한 거동의 차이를 확인하였으며, 이는 유동 중앙 재순환 영역에 존재하는 *precessing vortex core*에 의한 것으로 생각되었다. 유동의 주위 환경이 아임계 조건에서 초임계 조건으로 변화하였을 때 분사 유체의 상변화 및 밀도가 변화하였으며, 그에 따라 유동 후류의 거동, 유동의 분무각, 표면 파형 구조의 파장, 전파 속도 등의 유동 특성 또한 급격하게 변화하였다. 유동의 불안정 주파수를 측정하였을 때, 이는 *precessing vortex core* 불안정 주파수를 따르는 것이 발견되었다. 불안정 주파수는 주위기체압력 증가에 따라 유동 속도와 함께 감소하였으나, 주위 환경이 아임계 조건에서 초임계 조건으로 변화함에 따른 급격한 변화는 관찰되지 않았다. 이러한 결과는 유동의 표면 거동은 상변화된 분사 유체의 밀도에 의하여 크게 영향을 받으나, 불안정 특성은 액체 상태의 유동에 의하여 결정됨을 암시한다.

모드 분해 기법을 이용하여 아임계 및 초임계 조건에서의 극저온 스월 유동의 동적 특성을 실험적으로 연구하였다. 유동의 이미지로부터 다양한 불안정 구조의 중첩 및 와류 링 구조가 발견되었다. 유동의 분무각은 초임계 조건

에서 급격하게 감소하였으며, 이는 분사기 내부 유동의 독특한 상변화 과정에 따른 것으로 추측된다. 유동 이미지의 적합직교분해 (POD) 분석을 통하여 두 종류의 모드를 도출하였으며, 대칭/기울어진 링 형상 모드 및 반대칭 형상 모드가 존재함을 확인하였다. 대칭 모드는 Kelvin-Helmholtz 불안정에 의하여 생성되었으며, 반대칭 모드는 헬리컬 불안정에 의하여 발생하였다. 이때 헬리컬 불안정은 아임계 조건에서는 분사기 내부 액막의 불안정에 의하여 생성되는 반면, 초임계 조건에서는 유동 중앙 재순환 영역의 precessing vortex core 에 의하여 생성되는 것으로 추측된다. 한편, 유동의 후류 및 초임계 조건의 POD 모드에서 나타나는 고유 구조의 특성은 서로 유사하였다. 이는 유동의 거동이 분사 유체의 상태에 크게 영향을 받음을 나타낸다.

**중심어:** 액체 추진제 로켓 엔진, 단일 스월 분사기, 극저온 유동, 초임계조건, 유동 불안정, 적합직교분해법

**학 번:** 2009-30169